

UNIVERSAL SCALING FUNCTIONS AND EFFECTIVE FUNCTIONAL FORMS

A Dissertation

Presented to the Faculty of the Graduate School

of Cornell University

in Partial Fulfillment of the Requirements for the Degree of

Doctor of Philosophy

by

Yan-Jiun Chen

August 2013

© 2013 Yan-Jiun Chen
ALL RIGHTS RESERVED

UNIVERSAL SCALING FUNCTIONS AND EFFECTIVE FUNCTIONAL FORMS

Yan-Jiun Chen, Ph.D.

Cornell University 2013

This thesis is a practical study of how to report universal scaling functions for critical phenomena. We demonstrate, through three examples, how parametrized functional forms are flexible and useful in (1) describing critical systems with multiple control parameters, (2) extending the range of validity for the scaling theory, (3) providing accurate and reliable predictions, and (4) incorporating corrections to scaling and other non-universal effects. In Chapter 2 we find an effective form for the spin-spin correlation function for the 2d Ising model as a function of temperature and field, a useful observable for comparison with biomembrane lipid composition. In Chapter 3, we examine a common experimental problem: how to describe the scaling of events within a limited field of view, such as those observed under a microscope. In Chapter 4, we smoothly describe a crossover between two models of depinning in a concise function. We also describe a software environment *SloppyScaling* that facilitated these studies.

BIOGRAPHICAL SKETCH

Yan-Jiun (YJ) Chen was born in Taipei, Taiwan. Due to her parents' graduate studies, she bounced back and forth between Taipei and Wisconsin, and it took her 7 years to finish grades 1-6, but she graduated from Chengda Experimental Primary School in 1996. She finished her primary education at Shijian Junior High, and Taipei First Girls' Senior High.

YJ majored in Physics at National Taiwan University, where she dabbled in experiments, energy policy, and playwriting. She enjoyed her senior year as an exchange student at University of California- Berkeley, where she worked on her very first computational research project modeling chromosome packing in cell nuclei. In her gap year she grew diamond films for the Spallation Neutron Source at Oak Ridge National Lab.

At Cornell, she joined Jim Sethna's group, and had lots of fun learning how to program, looking at data with Gianfranco, cooking up scaling functions, attempting to understand FRG, and getting weird answers from DFT for surface energies. After graduation, she will be working as a software developer in Manhattan.

This thesis is dedicated to all the great physics teachers I've had throughout my studies.

And all my teachers of life.

ACKNOWLEDGMENTS

I'd like to acknowledge the significant contributions of my mentors and collaborators who were central to the work in this thesis; Gianfranco Durin, Stefanos Papanikolaou, Stefano Zapperi, Natalie Paquette and Ben Machta. I'd especially like to thank my Ph.D. advisor, Jim Sethna, who has taught me how to do research in these 5+ years. His mentorship, encouragement, and enthusiasm have made my graduate studies a wonderful experience.

During the course of my time at Cornell, I've also had the great fortune to have worked on projects or research ideas (not included in this thesis) with the following talented people: Bryan Daniels, Ryan Gutenkunst, Chris Myers, Susan Holcomb, Itai Cohen, Mihir Khadilkhar, Alex Alemi, Matt Bierbaum, Alexander Dobrinevski, Kay Wiese, and Pierre Le Doussal. A big thank you to all the members of the Sethna group with whom I've had the pleasure of sharing meetings and office space, for their help and collegiality on matters large and small, some of whom I've listed above, but also: Yong Chen, Woosong Choi, Mark Transtrum, Ricky Chachra, Ashivni Shekhawat, Isabel Kloumann, and Lorien Hayden.

I'm grateful for the support of the NSF-IGERT program in nonlinear systems during my first two years at Cornell. Other than funding, the seminars and required courses were an invaluable resource. It also afforded me the opportunity to visit Jean Carlson's group at UCSB and sit in on the Physics of Climate Change program at KITP in summer 2008, and later attend another program, the Mathematics of Climate Change, at the MSRI. Kevin Brown was instrumental in getting me launched on research at Santa Barbara. Mary Lou Zeeman was a great inspiration at the MSRI and also during reading discussions we had the following semester. Much appreciation to John Guckenheimer for organizing a great

program. And thanks to my IGERT cohort, I learned a lot from the vast array of talents you brought to the table.

Graduate school would not have been the same without the Ithaca friends who have provided companionship, laughter, and a sympathetic ear throughout my 6 years here: (roughly in order of appearance) Li-Wei Chiu, I-Chun Lin, Yao Weng, Jolyon Bloomfield, Kendra Letchworth Weaver, Turan Birol, Melina Bleses, Hsien-Wei Meng, Colwyn Gulliford, Ben Kreis, Stephen Poprocki, Hitesh Changlani, Ravishankar Sundararaman, Nora Callinan, Prajakta Karekar, Shayna Grajo, Amanda Hood, Yi-Ting Hsu, Philip Nee, Chloe Jiang, Nicole Baran, Flip Tanedo, Yariv Yanay, John Stout, Yi-Ju Wang. And I'm thankful for the old friends from Taipei and Berkeley that have kept in touch: Tina Hsu, Ernie Yang, Brianna Chang, Yee-chen Liu, Matthias Groener, Anne Lin, Jui-Ping Chiang— your phone calls and online presence have meant a lot to me.

A special thank you goes to the local salsa and swing dance communities, the GPSA, the GPSPB, the Ithaca Community Gardens, and the Cornell Chorale for the distractions from research, and also the balance they've afforded.

Much thanks to my family for their love and support. To my mom, dad, and grandma, who have looked after me for nearly 30 years— thanks for always having my back and providing me a place to call home. To my sister, Jesse, who is my best friend, and my favorite person too.

Where I stand today would not have been possible without the great teachers I've had throughout my academic life, whether instructors or peers, who've taught me math, physics, chemistry, biology, and stuff about computers. There are many beyond the people listed here, and their impact lingers.

TABLE OF CONTENTS

Biographical Sketch	iii
Dedication	iv
Acknowledgments	v
Table of Contents	vii
List of Figures	viii
List of Tables	ix
CHAPTER	PAGE
1 Introduction	1
1.1 Why universal scaling functions?	2
1.2 The various playgrounds of this thesis	3
1.2.1 The 2D Ising Model	3
1.2.2 Crackling noise in windows	5
1.2.3 Interfaces in Disordered Media	8
1.3 SloppyScaling	9
1.4 Outlook	10
2 Universal scaling function for the two-dimensional Ising model in an external field: A pragmatic approach	11
2.1 The spin-spin correlation function	11
2.2 Corrections to scaling	18
2.3 Methods and Accuracies	21
2.3.1 Scaling solutions at $H = 0$	21
2.3.1.1 Numerical evaluation of scaling solutions	21
2.3.1.2 Effective Functional Form	24
2.3.2 High-precision scaling form for the susceptibility	26
2.3.3 Analytic Corrections to Scaling	27
2.3.4 Accuracies and Errors	28
2.4 Small Distance Discrepancies	30
2.4.1 Numerical Methods: Wolff Algorithm in a field	33
2.5 Conclusion	35
3 Avalanche Spatial Structure and Multivariable Scaling Functions; Sizes, Heights, Widths, and Views through Windows	36
3.1 Introduction	37
3.2 Summary of Key Results	40
3.3 Model	45
3.4 Avalanche Shapes and Distributions of the Full System	47
3.4.1 Area-weighted size distributions	47
3.4.2 Maximum height and width distributions	51

3.4.3	Joint fit of size, height and width distributions	52
3.4.4	Local height distributions	58
3.4.5	Joint distributions and multivariable scaling functions	59
3.5	Window Effects	60
3.5.1	Internal Avalanches	64
3.5.2	Split Avalanches	66
3.5.3	Spanning Avalanches	68
3.6	Scaling Shapes and Results	76
3.6.1	Scaling shapes and functional forms	76
3.6.2	The limit of small windows	82
3.7	Suggestions for Experiments and Conclusions	82
3.8	Methods and software	85
3.8.1	Numerical simulation	85
3.8.2	Nonlinear least squares fitting	86
3.8.3	Software for fitting	88
3.8.4	Systematic Error Bars	88
3.8.5	Corrections to scaling	90
3.8.6	Scaling collapses and their limitations	92
3.9	The roughness exponent ζ	95
4	A scaling function description of a crossover between two models of depinning	100
4.1	Interfaces in Random Media	100
4.2	Preliminary Results	104
4.3	Unresolved Issues	107
4.4	Continuous time piecewise linear simulation	112
4.5	Outlook	115
APPENDIX		PAGE
A	SloppyScaling User Documentation	116
A.1	Preliminaries	116
A.1.1	Python	116
A.1.2	Installation	117
A.1.3	How to look for help	117
A.2	The SloppyScaling Module	118
A.2.1	The ScalingTheory class	118
A.2.2	The Data class	119
A.2.3	The Model class	119
A.2.4	The CompositeModel class	120
A.3	Additional Capabilities	120
A.3.1	Fitting Techniques	120
A.3.2	Monte-Carlo Ensemble Predictions	121

A.3.3	Convenience Functions for Organization	122
A.4	Examples	122
A.4.1	Example of one scaling function	123
A.4.2	Example of a joint theory	127
A.5	Frequently Asked Questions	135
References		136

LIST OF FIGURES

Figure	Page
1.1 Power Law Scaling Crossover From reference [7]. This experiment uses MOKE to measure avalanche sizes. A temperature dependent crossover is reported by looking at shifts in τ , from 1.32 to 1.04, for the size-distribution. The three different colors of the curves correspond to different effective windows of observation. Notice that only the straight-line power law is fit in these curves. We argue that this drift in exponent, while striking, could be better measured if the data was fit to a crossover scaling function, such as we provide in Chapter 4. Furthermore, in the paper, it is not specified how their data analysis is performed given the finite-size viewing window; are the avalanches cut off by the boundary discarded in the analysis, or are they kept in the data set? We demonstrate in Chapter 3 that these two practices would lead to different observed size-distribution exponent τ , and that window effects need to be considered for experiments.	7
2.1 Curves of constant ‘polar coordinate’ R are plotted against the Ising parameters of T and H , from outwards in: $R = 0.4$ (magenta), $R = 0.336737$ (blue), $R = 0.2$ (green), $R = 0.1$ (red). The critical point is labeled by the red circle. We compare to Monte-Carlo results for 1024×1024 simulations with parameters given by the blue dots. Note that the half-plane $T < T_c$ spans a small range of θ , namely from $\theta = 1$ to $\theta = \theta_c \approx 1.08144$ [26]. . .	14
2.2 Spin-spin Correlation Function Our functional form (lines) for the disconnected correlation function is in excellent agreement with large r simulation data (symbols) from systems of size $L = 1024$. Results are plotted at fixed R over the allowed range of θ as shown in Figure 2.1. At small distances (inset), there are other effects that the scaling function fails to capture.	17
2.3 Analytic Corrections Dots are simulation data from $L = 1024$ size simulations using the Wolff algorithm. The dashed line for all the plots are the scaling solutions, with $a(T) \approx a_0$, $\xi(T) \approx \xi_0 t^{-\nu}$, and $u_t = t$. The solid line is including corrections to first order in $a(T)$, $\xi(T)$, and u_t	22
(a) $H = 0$ $T > T_c$	22
(b) $H = 0$ $T < T_c$	22
2.4 Fit to Painleve Results at $T > T_c$ this is a fit to equation 2.24. Fit parameters $c = 1.73$, $b = 0.92$, $k = 3.8$. Red dots are Painleve results, and the black line is the result of the fit.	25

2.5	Fit to Painleve Results at $T < T_c$ this is a fit to equation 2.26. Fit parameters are: $c = 3.62$, $b = 0.87$, and $k = -0.4$. The magnetization is separated out, so that we may subtract it off for the interpolation- which makes things less complicated. Red dots are Painleve results, and the black line is the result of the fit.	26
2.6	Small Distance Discrepancies for $T > T_c$ $H = 0$ This figure shows the small distance discrepancies for data along $T > T_c$, $H = 0$. The dashed line is the scaling theory, while the solid line is including all first order corrections in $a(T)$, $\xi(T)$, and u_t . One can see that the discrepancy between simulation data and theory gets smaller as the distance increases.	30
2.7	Small distance corrections for $T < T_c$ $H = 0$ This figure shows the small distance discrepancies for data along $T < T_c$, $H = 0$. The dashed line is the scaling theory, while the solid line is including all first order corrections in $a(T)$, $\xi(T)$, and u_t . One can see that the discrepancy between simulation data and theory gets smaller as the distance increases.	33
2.8	Small Distance Corrections for All Data This is a plot that shows the small distance discrepancies for all the data we included in matching our interpolation results. It is a larger version of the inset of 2.2, so that we may see the details of where the scaling theory fails.	34
3.1	Windowed Distributions (a) The full system of avalanches. This figure shows a qKPZ simulation with avalanches. (b) A limited field of view: we can only see part of the system. The avalanches inside the artificial viewing window are brightly colored, and those outside are washed out. Notice that the avalanches within the window are cut off at top and bottom, and (more importantly for short, wide avalanches with roughness exponent $\zeta < 1$) on the two sides. (c) The size distributions for the different types of avalanches: (d) internal 00 avalanches, (e) split 10 avalanches, (f) split 01 avalanches, and (g) spanning 11 avalanches	41
3.2	Scale Invariance in Crackling Noise. Three simulations of crackling noise, with different “demagnetization fields”, k . (a) $k = 10^{-5}$ (b) $k = 10^{-6}$ (c) $k = 10^{-7}$ (k is what controls the typical avalanche sizes in a given system, giving a characteristic width L_k .) Larger demagnetization fields stop avalanches more strongly, hence large k corresponds to smaller avalanches. The colored regions represent avalanches. The fronts are moving from bottom to top. Notice that the two simulations are statistically similar to one another apart from a rescaling of heights and widths. Note that most of the area is covered by the largest avalanches.	46

3.3	<p>$A(S)$ vs $P(S)$. Here one can see the difference between the more traditional $P(S)$ and the area-weighted $A(S)$. (a) $P(S)$: most of the area under the curve is from small avalanches, where non-universal lattice effects are important. (b) $A(S)$: the normalization is dominated by large avalanches, avoiding the lattice effects, so that we can focus instead on the dependence on the large scale cutoffs- L_k and, in later sections the window size. The data here is from qKPZ simulations of different k with different simulation size L. The lines in (b) are a result of a joint fit with the maximum height and width distributions. The fitting function and fitting parameters are shown in Table 3.1.</p> <p>(a) Size Distribution (Probability)</p> <p>(b) Area-weighted Size Distribution</p>	48 48 48
3.4	<p>Area-weighted Avalanche Distributions for Maximum Heights and Widths Area-weighted avalanche distributions of (a) maximum heights, and (b) maximum widths for qKPZ simulations at different k, and simulation sizes L (dots are binned data). The critical exponents were jointly fit with the size distributions $A(S L_k)$ of Fig. 3.3, using the scaling forms of Eqs. 3.12, 3.13, and 3.14. The best fit values for the critical exponents, parameters for universal scaling functions, and non-universal corrections are given in Table 3.1.</p> <p>(a) Maximum heights</p> <p>(b) Maximum widths</p>	53 53 53
3.5	<p>Size Distribution $A(S L_k)$ Scaling Collapse We collapse the size distribution data using the universal exponents of $\tau = 1.24$, $\nu_k = 0.45$, and $\zeta = 0.62$, the best fit values of the joint fit between $A(S L_k)$, $A(h L_k)$ and $A(w L_k)$.</p>	55
3.6	<p>Height Distribution $A(h L_k)$ Scaling Collapse We collapse the simulation data using the universal exponents of $\tau = 1.24$, $\nu_k = 0.45$, and $\zeta = 0.62$, the best fit values of the joint fit between $A(S L_k)$, $A(h L_k)$ and $A(w L_k)$. . .</p>	55
3.7	<p>Width Distribution $A(w L_k)$ Scaling Collapse We collapse the width distribution data using the universal exponents of $\tau = 1.24$, $\nu_k = 0.45$, and $\zeta = 0.62$, the best fit values of the joint fit between $A(S)$, $A(h)$ and $A(w)$.</p>	56
3.8	<p>Area-weighted Local Height Distributions Here are the area-weighted local height distributions, the fraction of area taken up by a cross sectional height h_x. The fits shown in the figure were with the form of Eq. 3.16, where $\mathcal{A}_{h_x k}$ is the scaling function of the fit to 11 spanning avalanches (Eq: 3.33) which cross both window boundaries, taking $W = 0$. Details for this function are explained in Section 3.5.</p>	58

3.9	An Avalanche Cut by Windows in the Extreme Limits.	Drawn here are two fronts separated by an avalanche event. Here we are depicting cases where this avalanche (or its segment) is the maximum avalanche size for the 00, 10, and 11 at different window widths. Boxes of different widths and colors are used to show the cases in which this may happen. The main avalanche may count as a 00 avalanche for a wide window, while part of it would count as a 11 avalanche for a smaller window; it could also count as a 10 avalanche if it happens to cross the window boundary. This figure illustrates our arguments for the shape of the cutoff (the exponent n_{zz}) given a window size W for the 00, 11, 10 cases. Another small avalanche is drawn for the 11 case to show that the minimum size to cross the 11 window also introduces a separate cutoff.	62
3.10	Internal Avalanches Data and Fit	Shown here are the area-weighted size distributions for internal (00) avalanches. The lines are the joint best fit of A_{00} , A_{10} and A_{11} to the functional forms of equations 3.24, 3.27, and 3.33, whereas the shaded areas are the fluctuations in theory corresponding to the systematic covariant errors on our exponents and parameters (individual parameter best fit values and errors are quoted in Table 3.2).	66
3.11	Split Avalanches Data and Fit.	Shown here are the area-weighted size distributions for split (10) avalanches with different k and window size W . The lines are the joint best fit of A_{00} , A_{10} and A_{11} to equations 3.24, 3.27, and 3.33, whereas the shaded areas are the fluctuations in theory corresponding to the covariant systematic errors on our exponents and parameters (individual parameter best fit values and errors Table 3.2).	69
3.12	Spanning Avalanches Data and Fit	Shown here are the area-weighted size distributions for spanning (11) avalanches with different k and window size W . The lines are the joint best fit value using the functional forms using equations 3.24, 3.27, and 3.33, whereas the shaded areas are the fluctuations in theory corresponding to the systematic errors on our exponents and parameters (individual parameter best fit values and errors are quoted in Table 3.2).	72
3.13	Internal Avalanches Scaling Function.	(a) Scaling collapse showing $\mathcal{A}_{00}(s_k, W_k)$ as a function of s_k . The separate curves show the effects of the scaled window size W_k . (b) Logarithmic contour plot of best fit scaling function against both scaling variables s_k and W_k . Each contour reflects a drop of a factor of e in the scaling function. The black dots are at locations of the simulated data points used in the fit indicating where the fit should be a reliable prediction. The red solid line is $\log_{10} W_k = n_{00} \log_{10} s_k$ which is the slope at the large avalanche cutoff, with $n_{00} = 1.62$, the best fit value. ($n_{00} = 1 + \zeta = 1.63$ is the expected value from our heuristic arguments).	78
	(a)		78
	(b)		78

3.14	<p>Split Avalanches Scaling Function. (a) Scaling collapse showing $\mathcal{A}_{10}(s_k, W_k)$ as a function of s_k. The separation between curves shows the dependence on the scaled window size W_k. (b) Logarithmic contour plot of best fit scaling function against both scaling variables s_k and W_k. Each contour reflects a drop of a factor of e in the value of the scaling function. The black dots are at locations of the simulated data points used in the fit. The red solid line is $\log_{10} W_k = n_{10} \log_{10} s_k$ which is the slope at the large avalanche cutoff, with $n_{10} = 1.62$, the best fit value.</p> <p>(a)</p> <p>(b)</p>	79 79 79
3.15	<p>Spanning Avalanches Scaling Function. (a) Scaling collapse showing $\mathcal{A}_{10}(s_k, W_k)$ as a function of s_k. The curves move leftward and become more sharply rounded with increasing W_k. (b) Logarithmic contour plot of best fit scaling function. Each contour reflects a drop of a factor of e in the scaling function. The black dots are at locations of the simulated data points used in the fit. The upper orange solid line is the slope of the contour plot at the small avalanche cutoff, and has $\log_{10} W_k = 1/1.65 \log_{10} s_k$ where 1.65 is the best fit n_{11} value. The orange dashed has $\log W_k = 1/1.63 \log_{10} s_k$ where 1.63 is the $1 + \zeta$ value. The lower red solid line is $\log_{10} W_k = \log_{10} s_k$ which is the slope at the large avalanche cutoff.</p> <p>(a)</p> <p>(b)</p>	81 81 81
3.16	<p>Size distribution collapse Here we collapse the size distributions with exponents $\tau = 1.25$, $\nu_k = 0.44$, and $\zeta = 0.68$. Notice that the collapses are similar to the ones shown in Figure 3.5. Here only the combination of $\nu_k(1 + \zeta)$ affect the scaling collapse, the large shifts in ν_k and ζ mostly cancel in the product, yielding similar collapses.</p>	93
3.17	<p>Height distribution collapse Here we collapse the size distributions with exponents $\tau = 1.25$, $\nu_k = 0.44$, and $\zeta = 0.68$. Here only the combination of $\nu_k \zeta$ affect the scaling collapse, the large shifts in ν_k and ζ mostly cancel in the product, yielding similar collapses. Comparing this with the collapse shown in Figure 3.6, we see that the two collapses are comparable in quality, where in Figure 3.6 the large avalanche cutoff is collapsed nicely, and here the smaller avalanches are collapsed better.</p>	94
3.18	<p>Width distribution collapse Here we collapse the size distributions with exponents $\tau = 1.25$, $\nu_k = 0.44$, and $\zeta = 0.68$. Notice that the collapses are similar to the ones shown in Figure 3.7. Here only the combination of ν_k affects the scaling collapse and $(\tau - 2)(1 + \zeta)$ affects the shape of the scaling collapse. Since ν_k does not change significantly, the quality of the collapses are similar.</p>	95

3.19	Height-height Correlations for the qKPZ Simulations Shown here are the roughness exponents for various simulation sizes L and k . We measure the height-height correlation function $C(r) \sim \langle (h(x+r) - h(r))^2 \rangle$. A power law fit shows ζ falls between 0.63 and 0.68. The lower red-dashed line shows $\zeta = 0.63$ and upper black-dashed line $\zeta = 0.68$. The lines were shifted to show each individual power law.	96
3.20	Roughness Exponents for the qKPZ Simulations Shown here are the measurements of the local-log slope $\ln[C(r)/C(r/2)]/\ln(2)$ of the height-height correlation function; this is a measure for the roughness exponents for various simulation sizes L and k . The results of the local-log slope $\ln[C(r)/C(r/2)]/\ln(2)$ is consistent with what is seen in Figure 3.19. The lower red-dashed line shows $\zeta = 0.63$, corresponding to directed-percolation depinning (DPD) and suggested by literature to be the correct value for our model. Whereas the upper black-dashed line shows $\zeta = 0.68$ which is the result of our fits of windowed avalanche distributions. In the blowup of the region of $r/2 = 10 - 100$, we can see there is a trend of larger ζ corresponding to larger k simulations.	97
4.1	Crossover of qKPZ to qEW Model. Fronts generated from simulations with the nonlinear KPZ term coefficients set to (a) $\lambda = 0$, (b) $\lambda = 0.001$, (c) $\lambda = 0.1$, (d) $\lambda = 5$. The random colors represent the area between each pinned front. One can see that the morphology of the interfaces change dramatically as λ increases.	104
4.2	Local Log Slope. The measured local-log slope of the height-height correlation function for varying λ and k . The dashed red line is $\zeta = 0.63$, the dashed black line is $\zeta = 1.0$. The curves nearest to $\zeta = 1$ are for small lambda, with ζ increasing as we increase λ	106
	(a)	106
	(b)	106
4.3	Height-height Correlation Function. The numerics generated with an automata code are well described by Equation 4.8 with fit parameters $\zeta_{KPZ} = 0.78 \pm 0.003$, $\zeta_{EW} = 1.20 \pm 0.02$, $\phi = 1.02 \pm 0.04$, $A_1 = 0.37 \pm 0.09$, $A_2 = 1.0 \pm 0.2$, $M = 4.1 \pm 0.07$	108
4.4	Structure Factor. This is the Fourier transform of heights from simulations with the qEW equations with $\lambda = 0$, $k = 0.01$, $\gamma = 1$, and $L = 1024$. According to Equation 4.9, the slope should be given by $-(1 + 2\zeta)$. A best fit yields $\zeta = 1.1 \pm$, however, as one can see from the dashed line $\zeta = 1.25$ is also within error bars of the solution, so there is ambiguity to determining this exponent.	110

4.5	Mean-squared Elongation. Measuring the fluctuations in the length of the interface across different system sizes also gives a measure of ζ (Equation 4.10). However, here, with just three data points so far, the best fit is $\zeta = 1.04$.	111
A.1	Shaded Theory Predictions The colored regions represent the uncertainty in the theory generated from a Monte-Carlo sampling of the parameter space.	122
A.2	The Piano Tuner Data and Fit	127
A.3	The Piano Tuner Data Collapse	128
A.4	The Piano Tuner Fit Residuals	129
A.5	Rats in the City Data and Fit	132
A.6	Rats in the City Data Collapse	133
A.7	Rats in the City Residuals	134

LIST OF TABLES

Table	Page	
2.1	Cost and Errors for Interpolation The quality of our interpolation function is tabulated here in terms of average relative error (Equation 2.42) and average cost (Equation 2.41). For the calculation of this table, we skip the first 3 points (where lattice effects and higher-order corrections to scaling dominate) and data for $C < 10^{-2}$ (where the error is dominated by insufficient numerical statistics). (Note that the only data sets with values smaller than 10^{-2} are $\theta = 0$ and $\theta = 0.1$.) For $\theta = 0$, the statistical error becomes comparable to the data value once $C(r) < 0.01$, the error approaches 50% of the data value and exceeds that once $C(r) < 0.01$, and for $\theta = 0.1$ it approaches 5 – 10% after $C(r) < 0.01$. We expect our scaling form to be excellent in these large-distance regimes, where the corrections to scaling are negligible and the effects of the external field are small.	31
2.2	Cost and Errors with Corrections Here are the accuracies of the interpolation with all first order corrections (for $a(T)$, $\xi(T)$ u_t , and u_h) reported in terms of average relative error (Equation 2.42) and average cost (Equation 2.41). As in Table 2.1, we skip the first 3 points, and data below 10^{-2} . Note that with corrections the errors are smaller.	32
3.1	Best Fit Exponents and Parameters Here are the results of our joint fit for the size $A(S L_k)$, width $A(w L_k)$, and height $A(h L_k)$ distributions. The corresponding universal scaling forms which were fit are quoted in the table alongside the parameter results; on the bottom of the table are multiplicative corrections for each distribution, with x equal to either S , w , and h . Here systematic error bars which account for errors in the theory (see Section 3.8.4 for explanation) are given. The traditional standard error bars are typically ~ 64 times smaller than the systematic error bars quoted; however, they are a gross underestimate of the actual errors expected since our theory is both highly nonlinear and sloppy [73]. We quote each parameter to the significant figure indicated by its standard error, since the parameters are strongly correlated, truncating each parameter to its significant figure would yield a poor fit.	57

3.2	Best Fit Exponents and Parameters for Windowed Distributions. Here are the results of our joint fit for the windowed A_{00} , A_{11} , A_{10} distributions. The corresponding scaling forms which were fit are quoted in the table alongside the parameter results. Here systematic error bars which account for errors in the theory (see Section 3.8.4 for explanation) are given. The traditional standard error bars are typically ~ 30 times smaller than the systematic error bars quoted. The last column is the drift in parameters seen when allowing ζ to be a free parameter. Notice that these numbers are more or less similar or smaller than the estimated systematic error, except for ζ . (The problems in measuring ζ are discussed in Section 3.9) As in Table 3.1, we quote several digits more than the error bars warrant for individual parameters, because the errors are strongly correlated; truncating each parameter to its significant figures would yield a poor fit.	75
4.1	Roughness Exponents in Experiments. Table reproduced from [14]. Notice that there is a wide range of ζ reported, even for the same experimental system.	103

CHAPTER 1

INTRODUCTION

The study of phase transitions and critical phenomena has long been a fascinating subject to physicists. In particular, second order, continuous phase transitions exhibit scale-invariance and universality, allowing a particularly elegant theoretical framework. One of the most striking features about universality is that simple caricatures (such as the Ising Hamiltonian) are adept at describing the behavior of physical systems with intricate fluctuations across multiple length scales. Ideas from the Renormalization Group (RG) allow us to systematically explore the behavior of such Hamiltonians, and compute answers that are valid for scales that extend across orders of magnitude, and across a variety of systems that are dramatically different microscopically.

Many experiments and computational studies have milked this scale invariance by reporting power laws (the natural scale-invariant function), scaling collapses or scaling functions, and critical exponents, as evidence of a continuous phase transition or as verification or falsification of correspondence between experimental systems and a certain model class. In some cases, for certain models, analytic solutions for critical exponents or scaling functions are possible using mean-field theory, perturbative techniques (such as the momentum space ϵ -expansion), exact results, or variational approaches (such as density-matrix RG). However, in many cases, the analytical results are not helpful for any real-world system (such as a $6 - \epsilon$ result), or so far unobtainable (such as the crossover in Chapter 4), and hence there is a need for more practical numerical or experimental methods

for obtaining predictions. In this thesis, we will emphasize how, using the implications of RG, we can build parametrized functional forms for universal scaling functions. We will show that these forms are a useful and powerful tool for describing criticality and understanding the underpinnings of continuous phase transitions.

1.1 WHY UNIVERSAL SCALING FUNCTIONS?

While power laws and critical exponents have been the focus of many theoretical and experimental studies, we argue that reporting and measuring universal scaling functions should become standard practice in the study of critical phenomena— even in cases where it is not feasible to have analytic predictions for their forms.

The utility of reporting universal scaling functions can be summarized into the following:

- **Multiple variables:** In systems with more than one control variable, or more than one length scale, a scaling collapse will not suffice to capture the criticality or make predictions about the universal shape. In using parametrized forms, we can deal with as many variables as need be.
- **Better predictions:** Often power laws and exponents can be poorly measured when there are not enough decades of good quality data. Most scientists know from experience that data plotted on a log-log plot tends to look like a straight line. We can do better than reporting straight-line power laws. In this thesis, we demonstrate that it is not difficult to try to measure the full universal scaling function, and report the fit results with honest error bars which reflect the quality of our predictions.
- **Inclusive and extensive:** One very useful feature of using functional forms is that one may include non-universal effects, such as lattice corrections, amplitude

corrections, or finite-size effects. Often these subtle features themselves may have rich information about the system at hand. When we add these features, our predictions become much more powerful, the accuracy of the universal pieces may improve, and we extend the range of validity for which we can compare the data against our function.

The three different topics included in this thesis will more concretely demonstrate the points stated above. We start with a well-studied and widely known model system: the 2D Ising model in Chapter 2. We find an effective form for the spin-spin correlation function for the 2D Ising model as a function of temperature and field—a useful observable for comparison with biomembrane lipid composition which exhibits Ising criticality; In Chapter 3, we examine a common experimental problem: how to describe the power-law scaling of events within a limited field of view, such as those observed under a microscope; In Chapter 4, we smoothly describe a crossover between two models of depinning in a concise function that accounts for finite-size scaling in two different ways.

1.2 THE VARIOUS PLAYGROUNDS OF THIS THESIS

Below we give background on the three topics studied in this thesis, and the context in which the scaling forms we provide for these problems become useful.

1.2.1 THE 2D ISING MODEL

Invented nearly a hundred years ago to describe ferromagnetism, the Ising Hamiltonian

$$H = -J \sum_{ij} \sigma_i \sigma_j - h \sum_i \sigma_i \tag{1.1}$$

has been one of the most thoroughly studied model systems in statistical physics, and it has contributed significantly to our understanding of phase transitions. In the case of two-dimensions, at external field $H = 0$, Onsager solved the free energy exactly [1], and McCoy and Wu solved the spin-spin correlation function [2]. More recently, there have been conformal field theory solutions for $T = T_c$ at non-zero field [3, 4]. However, a full solution of the free energy as a function of temperature *and* field has eluded theorists, and even practical forms describing the spin-spin correlation function at arbitrary temperatures and fields has not been written down.

In recent years, interest in the Ising model has been renewed in the context of biology, and it is with this motivation that we would like an effective functional form for comparison to membrane experiments. The cell membrane is composed of lipid-bilayers, and when removed from the cell structure and cooled 5% below body temperature they phase separate into two liquid phases. This phase transition is well described as an Ising critical point [5]. As one varies the lipid composition in the phase diagram, the behavior of the cell lipids correspond to Ising models sitting at non-zero field. Methods of probing the structure of these membranes include Nuclear Magnetic Resonance (NMR), Florescence Resonance Energy Transfer (FRET) and fluorescence microscopy, which indirectly measure a spatial correlation of lipid molecules.

A spin-spin correlation function as a function of temperature and field therefore would allow for more direct comparison to these biomembrane probes, and also provide an approximate form that has been lacking in the Ising literature. In Chapter 2, we show how a simple interpolation between known results at $H = 0$, coupled with constraints of a high-precision equation of state calculation, describes simulation data to good precision and serves as a useful starting point for experimental comparison. In our study, we also systematically organize the available corrections to scaling scattered through the literature,

which will be important to include in any experimental comparison, since the magnitude of these corrections for a membrane would differ from an Ising square lattice simulation.

1.2.2 CRACKLING NOISE IN WINDOWS

As a ferromagnet switches magnetization direction under an external field, the domain wall moves in a jerky fashion, and the magnetic spins flip in avalanches, this is termed Barkhausen noise. If the magnet is placed in a coil and connected to speakers, one can hear crackling; this is the signature of a power-law size distribution of events. Traditionally, the avalanche size distributions and time evolution have been measured in such a fashion, with induction coils. In recent years, experiments have been developed to look at the domain wall motion of ferromagnet thin films under a microscope using the reflection of a polarized beam of lasers – the magneto-optical-kerr-effect (MOKE) – where the polarization of the laser beam switches directions according to the direction of magnetization of the film [6]. This has allowed experimentalists to measure new features of one of the most studied disordered critical systems.

However, measuring avalanches with a microscope has a disadvantage compared to the induction coil method– only events inside the viewing window are visible. This is especially a problem given that optical microscopes and recording devices have finite resolution– zooming out one sacrifices resolving smaller events, while zooming in one causes more distortion of your data set. It turns out that the exponent is modified, and an additional cutoff, in addition to finite-size effects of the sample, is introduced when viewing events through windows.

One experiment [7] on magnetic thin films that uses MOKE observes a temperature dependent crossover by measuring a change in the size-distribution exponent τ (where the

probability of sizes $P(s) \sim s^{-\tau}$ while varying temperature. (See Figure 1.1). While the drift in exponent they observe is interesting, from our point of view a more careful analysis is warranted. For one, there may be windowing effects like mentioned above and in Chapter 3. (We do not know if they included avalanche segments that cross the window boundaries.) Measurements of exponents by power-law fits more generally is problematic. Exponents for competing universality classes often do not differ by a large factor. For Barkhausen noise in three dimensions, the prediction for the size-distribution exponent is different for models in the mean-field ($\tau = 3/2$), with only short-range interactions ($\tau = 1.6$), and including long-range dipolar forces ($\tau = 1.3$) [8]; whereas in two dimensions, an interface with only short-range elasticity has $\tau = 1.1$ [9], while long-range dipolar forces give $\tau = 4/3$ [10]. Notice that in all these cases, τ only varies around 30%, these experiments may indicate a crossover (as the authors suggest), or a temperature dependent correction to scaling, or may purely be an artifact of finite-window distortions. It would be advantageous to measure the predicted scaling functions [11, 12] for better exponents. Or, even better, describe the proposed temperature dependent crossover with a clear crossover function that includes the limiting behavior in the two fixed points, as we do in Chapter 4.

We further realized that the finite viewing window is common to many experiments, and not just MOKE measurements of Barkhausen noise—any experiment that records power-law distributed events within a finite viewing window would have the same type of distortion in the form of a modified exponent, and a finite-window cutoff. These include experiments which record a movie of a pile of rice falling down an incline, fracture, and fluid imbibition. In Chapter 3 we write down how the scaling laws change in a finite-viewing window, and use complete functional forms of three variables: size s , characteristic avalanche width L_k , and window size W to describe the problem. We generate avalanches from a disordered interface simulation, and artificially window each set to test our scaling ideas and come up

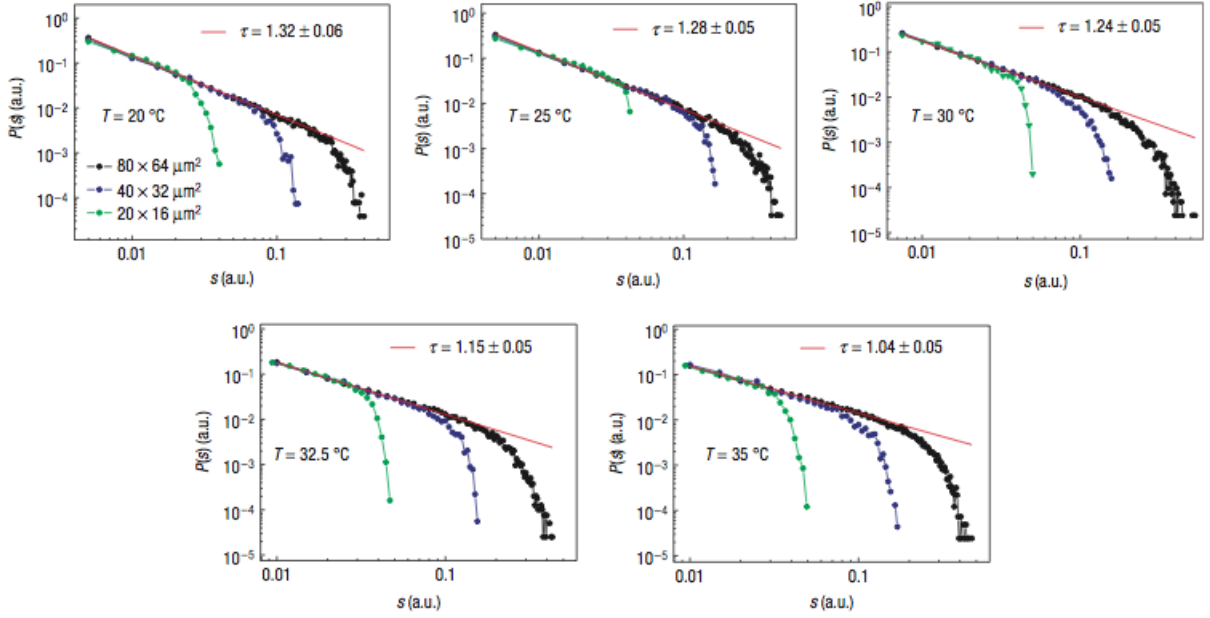


Figure 1.1: Power Law Scaling Crossover From reference [7]. This experiment uses MOKE to measure avalanche sizes. A temperature dependent crossover is reported by looking at shifts in τ , from 1.32 to 1.04, for the size-distribution. The three different colors of the curves correspond to different effective windows of observation. Notice that only the straight-line power law is fit in these curves. We argue that this drift in exponent, while striking, could be better measured if the data was fit to a crossover scaling function, such as we provide in Chapter 4. Furthermore, in the paper, it is not specified how their data analysis is performed given the finite-size viewing window; are the avalanches cut off by the boundary discarded in the analysis, or are they kept in the data set? We demonstrate in Chapter 3 that these two practices would lead to different observed size-distribution exponent τ , and that window effects need to be considered for experiments.

with accurate functional forms to describe them. We believe these results will be very valuable towards evaluating experiments with viewing windows, both in direct predictions, and in an overall methodology of presentation.

1.2.3 INTERFACES IN DISORDERED MEDIA

Although the concepts of RG apply to all critical points, not all critical phenomena can be dealt with using the same machinery. Systems that are non-equilibrium and/or contain disorder often prove more difficult to deal with analytically in comparison to equilibrium systems without noise (such as the 2D Ising model in Section 1.2.1). Nonetheless they exhibit behavior that are physically interesting and relevant. The depinning transition is an example of non-equilibrium disordered criticality. Depinning is a competition between an external force and a pinning potential; experimental systems described by these models include the dynamics of materials with charge density waves (CDW), or interfaces (such as the magnetic domain wall mentioned in Section 1.2.2, or in fluid imbibition) [13, 14].

Consider the simplest model of a interface $h(\vec{x})$ in d -dimensions with elastic forces between the interface segments, some type of external driving field F (the applied magnetic field in magnets, or the applied voltage in CDW), and some type of pinning force $\eta(h, \vec{x})$ (the impurities or defects in magnets). The equation can be written as:

$$\frac{dh(\vec{x}, t)}{dt} = F + \gamma \nabla^2 h(\vec{x}) + \eta(h, \vec{x}). \quad (1.2)$$

This is the quenched Edwards-Wilkinson (qEW) equation. Notice this equation has translation invariance in space and time, and rotation and inversion symmetry in the direction $h(\vec{x}, t)$ is moving. And if we set $F = 0$ or constant, there is up/down symmetry for h . In general, if we would like to add some other interaction, and break one of the symmetries, we can choose to break the up/down symmetry, and the appropriate lowest-order

term to choose would be $(\nabla h)^2$, which would lead to the quenched Kardar-Parisi-Zhang (qKPZ) equation.

The breaking of this symmetry drives the behavior of the system away from the qEW fixed point, and changes the universality class. Although other crossovers between interface dynamics have been studied and observed [10], systematic treatment of this crossover has been lacking. Although there have been a number of analytic studies for qEW [15, 16] and numerical studies for qKPZ [17, 18], the qEW to qKPZ crossover is not well described due to difficulty in computing analytic results [19].

We connect simulations of these two models to a universal crossover function in Chapter 4, using the height-height correlation function to describe the change in the morphology of the interface between qEW and qKPZ. The crossover proves to be a fascinating subtle problem where finite-size effects become important at the qEW fixed point, while a non-universal amplitude also plays a role in the height-height correlation function. Simulations for this problem are also less than straightforward— it is plausible that lattice automata break the same symmetry that the $(\nabla h)^2$ term (the KPZ term) breaks, and prevents us from accessing the true qEW fixed point. Therefore, we also provide ideas for an efficient continuous-motion algorithm at the end of the chapter.

1.3 SLOPPYSCALING

To facilitate the fitting and visualization of the universal scaling functions reported in this thesis, we have written a software environment *SloppyScaling* in Python [20]. It includes (a) capabilities to fit and plot scaling functions with up to four variables, (b) generate parameter ensemble predictions and error bars, (c) access to many of the fitting

algorithms recently developed by Mark Transtrum [21], and (d) use a covariance matrix for least-squares fitting. Currently this is written as a collection of convenient classes to be used interactively in a Python command line environment. A more user-friendly GUI version is currently under development [22]. User documentation is included in Appendix A.

1.4 OUTLOOK

We hope that our work in these three examples will encourage others to report and describe universal scaling functions in addition to the commonly reported power-laws and scaling collapses, even when analytical results are not available. This approach should not be limited to simulations and theory; we are currently analyzing data from Barkhausen noise experiments with which we will apply the same principles— using complete and descriptive functional forms for reporting results. The use of universal scaling functions, while incorporating analytic and singular corrections, is a discerning tool for the study of critical phenomena; they enable us to provide complex predictions for multivariable properties in a broad region of parameter space around the critical point.

UNIVERSAL SCALING FUNCTION FOR THE TWO-DIMENSIONAL ISING MODEL IN AN EXTERNAL FIELD: A PRAGMATIC APPROACH ¹

We report an effective functional form for the spin-spin correlation function of the 2D Ising model as a function of temperature and field. Although the Ising model has been well-studied, no analytical result for the spin-spin correlation function exists for arbitrary magnetic fields and temperatures. We show the validity of our form by comparison with simulations using the Wolff algorithm, and obtain useful precision by including analytic corrections to scaling. Given recent interest in comparing biomembrane heterogeneity to Ising criticality, our spin-spin correlation function may be used as a predictive quantitative measure for FRET or NMR membrane experiments.

2.1 THE SPIN-SPIN CORRELATION FUNCTION

The two-dimensional (2D) Ising model occupies a unique place in statistical physics. As the simplest example of a system displaying nontrivial critical phenomenon it has long been a testing ground for theoretical and computational methods, having spawned thousands of

¹This is work done in collaboration with Natalie Paquette, Benjamin B. Machta, and James P. Sethna, submitted, arXiv:1307.6899.

papers. In addition, it is the canonical member of the 2D Ising universality class. Members of the 2D Ising universality class include many current experimental systems, some (e.g. liquid-vapor phase transitions or membrane phase diagrams) far removed from its original conception as a simple model of ferromagnetism.

In the vicinity of its critical point the spin-spin correlation function for the 2D Ising model approaches a two parameter universal scaling function

$$C(r|H, T) = \langle \sigma_r \sigma_0 \rangle = r^{-\eta} \mathcal{C}(r/t^{-\nu}, h/t^{\beta\delta}) \quad (2.1)$$

with $\eta = 1/4$, $\nu = 1$, $\beta = 1/8$, $\delta = 15$, reduced temperature $t = \frac{T-T_c}{T}$ and field $h = \beta H = H/T$. σ is the value of the spin (either 1 or 0), and r is the distance between spins. The form of the universal function \mathcal{C} is known along two lines through its parameter space: when $H = 0$ it can be written in terms of an integral over Painlevé transcendents [2] and when $T = T_c$ there exists a complete asymptotic expansion that uses exact results from integrable field theory [4, 23]. Approximate functional forms for the correlation function and the correlation length have been developed for the 3D Ising model in a field in momentum space [24, 25]. Here we leverage the known exact results and a high precision approximate form for the free energy [26] to develop an elegant interpolation for the scaling form for the 2D Ising correlation function in an external field.

In addition to filling a surprising gap in the theoretical Ising literature, our results are of practical relevance for the interpretation of experiments in multicomponent lipid membranes. Phase diagrams for these membranes often contain miscibility critical points in the two-dimensional Ising universality class [27, 28]. Recent experiments suggest that cells may be tuning their own membranes to the proximity of this critical point [29] suggesting cells may be taking advantage of criticality's unique physics [30, 31]. NMR [27], FRET [32], and fluorescence microscopy [33] all yield observables that are simply related to the

underlying membrane’s correlation functions. Although scattering experiments in typical three dimensional systems more naturally probe the Fourier transform of $C(r)$, membrane probes more typically measure real-space properties. With our scaling forms it will be possible to map the Ising axis of t and M (the magnetization) onto the composition and temperature parameters of these membranes.

It is useful to describe the scaling behavior near the critical points using the Schofield ‘polar coordinate’ parametrization [26, 34, 35], which is expressed as follows:

$$t = \frac{T - T_c}{T} = R(1 - \theta^2) \quad (2.2)$$

$$h = H/T = h_0 R^{\beta\delta} h(\theta) \quad (2.3)$$

$$M = m_0 R^\beta \theta \quad (2.4)$$

Here, we use Caselle’s [26] high precision form for $h(\theta)$:

$$h(\theta) = (\theta - \theta^3/1.16951)(1 - 0.222389\theta^2 - 0.043547\theta^4 - 0.014809\theta^6 - 0.007168\theta^8). \quad (2.5)$$

We take $m_0 = 0.90545$ [36] and $h_0 = 0.940647$ [26]. Figure 2.1 shows a representation of the coordinate transform, with curves of constant R plotted in (T, H) . Exact scaling results exist at three points along each curve, $\theta = 0$ ($H = 0, T > T_c$), $\theta = \theta_c$ ($H = 0, T < T_c$), $\theta = 1.0$ ($T = T_c$). Other systems (like membrane miscibility phase diagrams) can be treated by suitable mappings of their control variables into (R, θ) .

We would like to compare our functional form to simulation results from systems that are close enough to the critical point to be in the scaling regime yet which have a correlation length small compared to our lattice size $L = 1024$ so as to minimize finite-size corrections. Therefore we run simulations at a range of θ values at a fixed R value chosen to have correlation lengths between $\xi_+ \approx L/60$ and $\xi_- \approx L/10$ above and below T_c . Interpolating

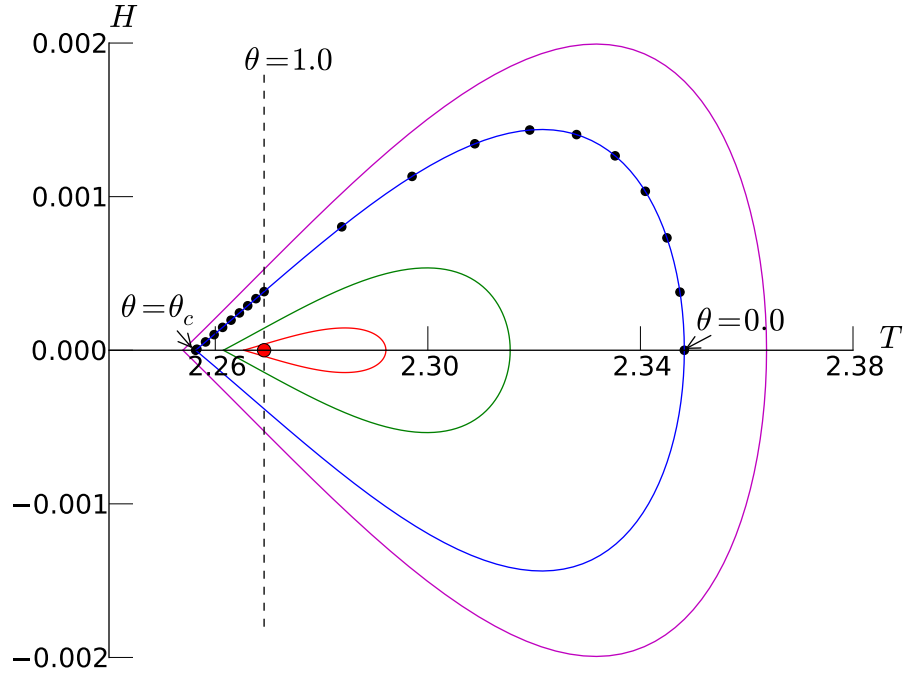


Figure 2.1: Curves of constant ‘polar coordinate’ R are plotted against the Ising parameters of T and H , from outwards in: $R = 0.4$ (magenta), $R = 0.336737$ (blue), $R = 0.2$ (green), $R = 0.1$ (red). The critical point is labeled by the red circle. We compare to Monte-Carlo results for 1024×1024 simulations with parameters given by the blue dots. Note that the half-plane $T < T_c$ spans a small range of θ , namely from $\theta = 1$ to $\theta = \theta_c \approx 1.08144$ [26].

between known results along $h = 0$ above and below $T = T_c$ [37], and using a high-precision form [26] of the susceptibility as an integration constraint, we are able to arrive at an interpolating correlation function that matches our simulation data for all values of θ .

As one component of the functional form, we need an interpolating form for the asymptotic correlation length $\xi(H, T) = \xi(R, \theta)$ giving the long-distance exponential decay of the correlation function. Here we define a scaling variable $s = r/\xi(H, T)$, where $s \approx (4/T_c)(r/t^{-\nu})$ along $H = 0$ and $s \approx r(h/h_s)^{8/15}$ with $h_s = \left(\frac{\Gamma(2/3)\Gamma(8/15)}{4\sin(\pi/5)\pi\Gamma(1/5)}\right)^{15/8} \left(\frac{\Gamma(1/4)\Gamma^2(3/16)}{4\pi^2\Gamma(3/4)\Gamma^2(13/16)}\right)^{1/2}$ along $T = T_c$ [4]. We design an even polynomial in θ in the form of $\xi(R, \theta) = \Xi(\theta)/R$, since $\xi \sim t^{-\nu} \sim R^{-\nu}$ where $\nu = 1$.

$$\Xi(\theta) = a_0 + a_1\theta^2 + a_2\theta^{34} \quad (2.6)$$

Matching the two known values at $H = 0$ and the value at $T = T_c$ we fix a_0 , a_1 , and a_2 . $a_0 = 0.567296$, $a_1 = 0.0284915$ and $a_2 = 0.19171$. The power 34 is taken from a fit of $a_0 + a_1\theta^2 + a_2\theta^n$ to known values at $\Xi(0)$, $\Xi(1)$, $\Xi(\theta_c)$, where 34 is the smallest even power that allows $\Xi(\theta)$ to be monotonic with increasing θ . This large power is likely due to the strong asymmetry of the Schofield coordinates (Figure 2.1), which compress the range $T < T_c$ into $1 < \theta < \theta_c \approx 1.08144$.

Now, with the scaling variable $r/\xi = rR/\Xi(\theta)$ we can further use known scaling solutions to find an interpolating form for the correlation function. We design a function that interpolates between the exact scaling solution [37] $F_+(s)$ at $T > T_c$ and $F_-(s) - M^2$ for $T < T_c$, replacing the scaling variable with our form $s = rR/\Xi(\theta)$. The function $f(\theta)$ controls the interpolation, and is designed such that $f(0) = 0$ and $f(\theta_c) = 1$. Outside of the

interpolation, we add back the magnetization in Schofield coordinates with $(m_0 R^\beta \theta)^2$.

$$C(r|R, \theta) = r^{-1/4} \left((1 - f(\theta)) F_+ \left(\frac{r}{R\Xi(\theta)} \right) + f(\theta) \left(F_- \left(\frac{r}{R\Xi(\theta)} \right) - 2^{3/8} \left(\frac{r}{R\Xi(\theta)} \right)^{1/4} \right) \right) + (m_0 R^{1/8} \theta)^2 \quad (2.7)$$

Here $2^{3/8} s^{1/4}$ is the limit of $F_-(s)$ as $s \rightarrow \infty$, which is the scaling part of the exact magnetization $M(T)^2 = (1 - \sinh(2/T)^{-4})^{1/4} \approx r^{1/4} F_-(\infty) \approx m_t^2 t^{1/4}$. Also, we have $m_0 = m_t |1 - \theta_c^2|^{1/8} / \theta_c$. The exact zero-field scaling solutions F_+ and F_- are integrals of Painlevé transcendents of the third kind, which are not expressible in closed form functions of s , nor readily available in subroutine libraries. In Section 2.3.1.2, we offer a high-precision implementation for the necessary Painlevé function. In addition, we provide a simple fitting form for F_+ and F_- , accurate to within 3.4% and 1% respectively for three orders of magnitude of scaling arguments and written in terms of simple elementary functions.

The interpolating function $f(\theta)$ is chosen to match the scaling form for the susceptibility, namely $\chi(R, \theta) = R^{-7/4} X(\theta) = \int dr 2\pi r (C(r, R, \theta) - m(R, \theta)^2)$, using a high-precision polynomial form for $X(\theta)$ from [26] (see Section 2.3.2), this leads to:

$$f(\theta) = \frac{X(\theta)/2\pi - \Xi(\theta)^{7/4} \mathcal{I}_+}{\Xi(\theta)^{7/4} (\mathcal{I}_- - \mathcal{I}_+)} \quad (2.8)$$

where $\mathcal{I}_+ = \int dy y^{3/4} F_+(y)$, $\mathcal{I}_- = \int dy y^{3/4} (F_-(y) - m_0^2 y^{1/4} \theta_c^2 \Xi(\theta_c)^{1/4})$. Numerical integration of the exact scaling results gives $\mathcal{I}_+ = 0.413135114$ and $\mathcal{I}_- = 0.010959562$. Using our approximate forms the two constraints $f(0) = 0$ and $f(\theta_0) = 1$ give $\mathcal{I}_+ = 0.413134$ and $\mathcal{I}_- = 0.0104234$ at our current R.

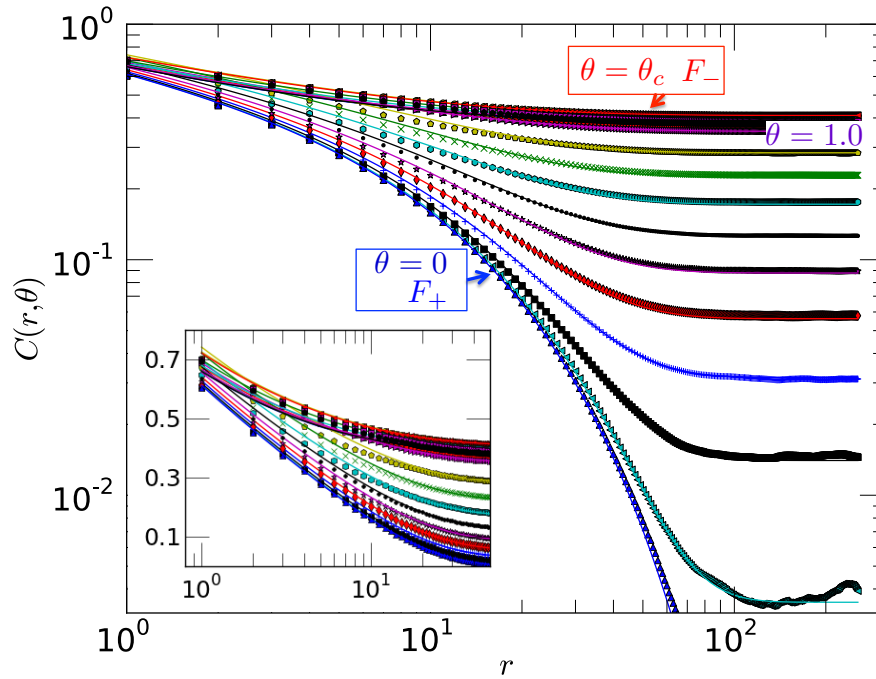


Figure 2.2: Spin-spin Correlation Function Our functional form (lines) for the disconnected correlation function is in excellent agreement with large r simulation data (symbols) from systems of size $L = 1024$. Results are plotted at fixed R over the allowed range of θ as shown in Figure 2.1. At small distances (inset), there are other effects that the scaling function fails to capture.

2.2 CORRECTIONS TO SCALING

This simple interpolation description for the correlation function (Figure 2.2) is in agreement with simulation results within 2% relative error except at distances less than three spin spacings, below which nonuniversal lattice effects dominate (see Section 2.4 for discussion). Although our interpolating form is approximate even in the scaling limit, its agreement with simulation results can be improved by including analytic and singular corrections to scaling that vanish with increasing r .

There has been theoretical work [38, 39] on the amplitudes of the dominant analytic corrections to scaling in the 2D Ising model on a square lattice, and evidence that the dominant singular corrections to scaling happen to vanish. In an experimental system (e.g., biomembranes), the magnitudes of these analytic and singular corrections to scaling must be experimentally determined. They will give small corrections near (T_c, H_c) , but will extend the validity of the theory further into the phase diagram – perhaps facilitating systematic identification of phase boundaries.

We begin at $H = 0$, where due to exact results [37] and perturbative studies [39, 40] we can write a general form for both analytic and singular corrections to scaling and can add the leading corrections exactly. Although Equation 2.1 becomes exact as $r \rightarrow \infty$, for finite r there are a hierarchy of corrections that arise from a more complete form:

$$C(r|T) = a(T)r^{-\eta}\mathcal{C}(r/\xi(T), u_3t^\Delta, \dots). \quad (2.9)$$

where u_i for $i > 2$ are irrelevant directions under the renormalization group, with u_3 the leading singular correction. The T-dependent functions can be written in a series expansion

of t ,

$$a(T) = a_0(1 + a_{1,0}t + O(t^2)) \quad (2.10)$$

$$\xi(T) = \xi_0 t^{-\nu}(1 + c_\xi t + O(t^2)), \quad (2.11)$$

where $a_0 = 2^{3/8}$ and $\xi_0 = T_c/4$ are Ising specific prefactors for the scaling form [37]. Expanding the exact form of $a(T)$ and $\xi(T)$ given by McCoy and Wu [37], we get $a_{1,0} = 2^{-3/2}(4/T_c)$, and $c_\xi = -1/(\sqrt{2}T_c)$ which are the first analytic corrections to scaling. Figure 2.3 shows the improvement in accuracy enabled by these analytic corrections along $H = 0$.

The first order effect of the leading irrelevant direction u_3 to scaling is to generate a power-law, singular correction that looks like $r^{-\eta-\Delta}$:

$$\begin{aligned} C(r|t, u_3) &= r^{-\eta} \mathcal{C}(r/t^{-\nu}, u_3 t^\Delta) \\ &= r^{-\eta} \mathcal{C}(r/t^{-\nu}, 0) + u_3(t) r^{-\eta-\Delta} \mathcal{C}^{(1)}(r/t^{-\nu}, 0) \end{aligned} \quad (2.12)$$

where $\mathcal{C}^{(1)}(r/t^{-\nu}, 0)$ is the derivative of the scaling function $\mathcal{C}(r/t^{-\nu}, u_3 t^\Delta)$ with respect to u_3 at $u_3 = 0$. For the Ising critical point, studies have found that $u_3 = 0$ [39, 40], and in our data we also see no evidence for a power-law of $r^{-\eta-\Delta}$ upon subtracting the exact scaling solutions from the numerical data. However, there is no reason that biomembrane experiments should expect $u_3 = 0$. For example, it is non-zero in Ising-like models (square-lattice Klauder and double-Gaussian model) [39], with $\Delta \approx 1.35$

One can also expand the non-universal amplitude $a(T)$, noticing $a_{10}t = 2^{3/2}s/r$, to get: $C(r) = r^{-1/4}F_\pm(s) \pm 2^{-3/2}r^{-5/4}sF_\pm(s) + (9/64)r^{-9/4}s^2F_\pm(s)$. Estimated values of Δ give $\eta + \Delta \approx 1.6$ and so in principle:

$$\begin{aligned} C(r) &= r^{-0.25}F_\pm(s) \pm 2^{-3/2}r^{-1.25}sF_\pm(s) \\ &+ \frac{9}{64}r^{-2.25}s^2F_\pm(s) + u_3(t)r^{-1.6}\mathcal{C}^{(1)}(r/t^{-\nu}, 0). \end{aligned} \quad (2.13)$$

In the case of Ising-like criticality in experiments, where no exact results are known, the combination of the effect of powers of $r^{-1.25}$, $r^{-1.6}$, and $r^{-2.25}$ would not be easy to disentangle, requiring a fit to a function that looks like $C(r) = r^{-0.25}\mathcal{C}(s) + r^{-1.25}\mathcal{C}_1(s) + r^{-2.25}\mathcal{C}_2(s) + c_{u_3}r^{-1.6}\mathcal{C}^{(1)}(s, 0)$. This fit will likely be sloppy [41], with the individual coefficients ill-determined.

Now that we have investigated corrections to scaling at $H = 0$, let us return to our main goal. The correlation function that we provide in this paper is a function of both temperature and field, so we will need to consider analytic corrections in a field. In principle, instead of the scaling form correlation function written in Equation 2.1, the full correlation function should look like:

$$C(r|T, H) = a(T, H)r^{-\eta}\mathcal{C}(r/u_t^{-\nu}, u_h/u_t^{\beta\delta}, \dots). \quad (2.14)$$

Here we incorporate analytic corrections to scaling (as in eqns 2.11) via the scaling fields u_t and u_h , which are only consistent with the tuning parameters t and h up to first order. We may instead write the non-universal amplitudes and scaling fields in terms of t and h . Using the notation of [40] they are,

$$a(T, H) = a_0(1 + a_{1,0}t + a_{0,2}h^2 + a_{2,0}t^2 + \dots) \quad (2.15)$$

$$u_t = t(1 + c_t t + O(t^2, h^2)) \quad (2.16)$$

$$u_h = h(1 + c_h t + O(t^2, h^2)) \quad (2.17)$$

$$\xi(u_t) = \xi_0 t^{-\nu}(1 + c_\xi u_t + O(u_t^2, u_h^2)) \quad (2.18)$$

By the inversion symmetry of the Ising lattice, only terms of h^{2n} are should be allowed. As h has the same scaling dimensions as $t^{\beta\delta} = t^{15/8}$, the leading analytic corrections should be controlled by temperature up to t^3 and we only consider leading order corrections arising from t .

For the 2D Ising model it is known that $c_t = c_h = \beta_c/\sqrt{2}$ [26], so we can add all forms of analytic corrections to our scaling function. For the nonlinear scaling fields u_t and u_h , we can translate the effective temperature and field $t_{\text{eff}} = t(1 + c_t t)$ and $h_{\text{eff}} = h(1 + c_h t)$ to effective Schofield coordinates, $R_{\text{eff}} = R(1 + g_1(\theta)R)$ and $\theta_{\text{eff}} = \theta(1 + g_2(\theta)R)$ assuming that since R scales with t , they will have the same leading order effects, and assuming an arbitrary form for the corrections dependent on θ . Using our parametric definition (see eq 2.5) we can arrive at closed form expressions for $g_1(\theta)$ and $g_2(\theta)$ (see Section 2.3.3), and incorporate θ_{eff} and R_{eff} into Equation 2.7. For the amplitude corrections and scaling function corrections, we include them respectively in $F_{\pm}(s)$ according to the McCoy/Wu expansion. Including the analytic corrections in $a(T)$, $\xi(T)$, u_R and u_{θ} for the constant- R data in Figure 2.2 leads to a improvement in the accuracy for the data sets at $\theta = 0$, $\theta = 1$, and $\theta = \theta_c$ (Figure 2.3), but no systematic improvement for the data sets in between these special points. This is perhaps unsurprising so near to the critical point, where the analytic corrections are small compared to the residual errors in our scaling form. Overall, including the corrections to scaling, our functional form has an average relative error of 1.5% per data point.

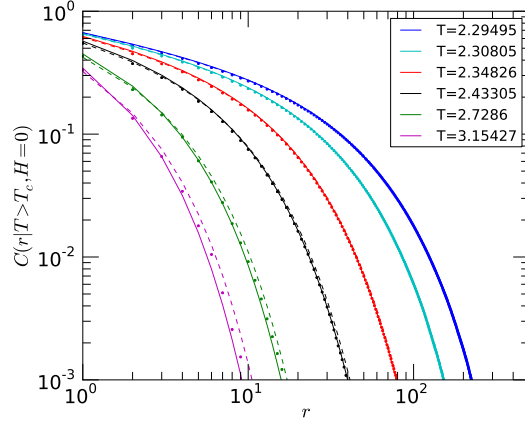
2.3 METHODS AND ACCURACIES

2.3.1 SCALING SOLUTIONS AT $H = 0$

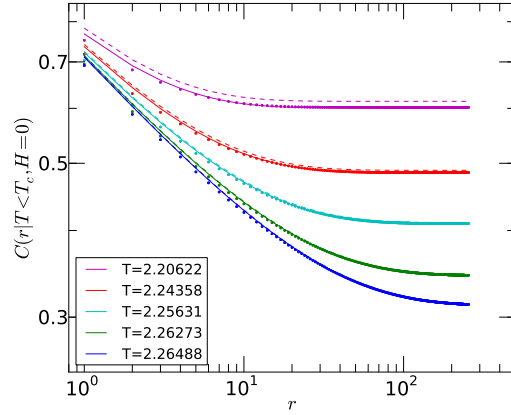
2.3.1.1 NUMERICAL EVALUATION OF SCALING SOLUTIONS

In Section 2.1, we make use of the scaling solutions for the disconnected correlation function at $H = 0$,

$$\langle \sigma_r \sigma_0 \rangle = r^{-1/4} F_{\pm}(s) \tag{2.19}$$



(a) $H = 0 \ T > T_c$



(b) $H = 0 \ T < T_c$

Figure 2.3: Analytic Corrections Dots are simulation data from $L = 1024$ size simulations using the Wolff algorithm. The dashed line for all the plots are the scaling solutions, with $a(T) \approx a_0$, $\xi(T) \approx \xi_0 t^{-\nu}$, and $u_t = t$. The solid line is including corrections to first order in $a(T)$, $\xi(T)$, and u_t .

which is valid as $T \rightarrow T_c$ and $r \rightarrow \infty$ with s fixed. The symbol \pm denotes solutions for $T > T_c$ and $T < T_c$ respectively. Analytical studies use $s^* = |z^2 + 2z - 1|/\sqrt{z(1-z^2)}r$ with $z = \tanh(1/T)$ as the argument for this function, however in section 2.1 we used the scaling form $s = (4/T_c)(r/t^{-\nu})$. The solutions are of the form [37]:

$$F_{\pm}(s) = 2^{-1/2} (2 \sinh(2/T))^{1/8} (s/2)^{1/4} (1 \mp \eta(s/2)) \eta(s/2)^{-1/2} \exp \left(\int_{s/2}^{\infty} dx \frac{x}{4} \eta(x)^{-2} ((1 - \eta(x)^2)^2 - \eta'(x)^2) \right) \quad (2.20)$$

$\eta(\theta)$ is the solution to the Painleve differential equation of the third kind,

$$\frac{d^2 \eta}{d\theta^2} = \frac{1}{\eta} \left(\frac{d\eta}{d\theta} \right)^2 - \eta^{-1} + \eta^3 - \theta^{-1} \frac{d\eta}{d\theta} \quad (2.21)$$

with boundary conditions

$$\eta(\theta) = -\theta \left[\ln \left(\frac{\theta}{4} \right) + \gamma_E \right] + O(\theta^5 \ln^3 \theta) \quad (2.22)$$

as $\theta \rightarrow 0$, and

$$\eta(\theta) = 1 - \frac{2}{\pi} K_0(2\theta) + O(e^{-4\theta}) \quad (2.23)$$

as $\theta \rightarrow \infty$ with $K_0(x)$ is a modified Bessel function of the 2nd kind. The Painleve transcendent $\eta(\theta)$ is not expressible in terms of elementary functions; to evaluate it numerically, we choose to use tools available in the Chebfun Matlab package [42]. We use a Chebyshev polynomial approximation for $\eta(\theta)$ between arguments of 0.003 and 3, while we use the asymptotics given in Equations 2.22 and 2.23 for arguments outside of this range. To evaluate Equation 2.20, we use integration subroutines available in Matlab and Python, the adaptive Simpson quadrature function *quad* in Matlab, and the `scipy.integrate.quad` function which draws from the Fortran library QUADPACK (mainly adaptive quadrature techniques). Our Matlab implementation and the Python module containing the Chebyshev polynomial for $\eta(\theta)$ and the $F_{\pm}(s)$ scaling function is available online [43].

2.3.1.2 EFFECTIVE FUNCTIONAL FORM

For convenience and less opaque representation of the scaling solutions, we also provide an effective functional form, which is good to 3.4% relative accuracy for F_+ and 1% relative accuracy for F_- . These functions are an interpolation between the small and large distance asymptotics for the exact scaling solutions at $H = 0$.

Both scaling functions have $F_{\pm}(0) = C_0 = 0.7033801577\dots$. The asymptotic large- r behavior is different depending on whether one is above or below criticality. The $T > T_c$ case is particularly simple, partially since $\langle M^2 \rangle = 0$. We simply choose the effective large- r functional form to be the exponential decay given by the Ornstein-Zernike decay, which is like $s^{-1/4} \exp(-s)$ for $T > T_c$. The amplitude of this piece, called p_1 , is determined by an asymptotic expansion of the large distance Bessel functions, and we get $p_1 = 1/(2^{1/8} \sqrt{\pi})$.

We find a simple and effective nonlinear interpolation that we will employ in both the high and low-temperature cases. Empirically, we find that both functions are well-described by $F_{\pm}^{\text{fit}} = (B(s)^{|k|}(\text{Small-r})^k + (1 - B(s)^{|k|})(\text{Large-r})^k)^{1/k}$, where k is a fit parameter, that controls the nonlinear interpolation of the functions, whereas a weighting function $B(s)$ that has the limits $B(0) = 1$ and $B(\infty) = 0$ controls the weight of each piece of the interpolation. For $T > T_c$ we write:

$$F_+^{\text{fit}}(s) = (0.70338^k B(s)^{|k|} + (1 - B(s)^{|k|})(p_1 \cdot s^{-1/4} \exp(-s))^k)^{1/k}. \quad (2.24)$$

with

$$B(s) = \exp(-(cs)^b) \quad (2.25)$$

If k is negative, we need to make the weights $(1/B(s))^k$ and $(1/(1 - B(s)))^k$, for $F_+^{\text{fit}}(s)$ to have the right limits at $s = 0$ and $s = \infty$, hence the absolute value $|k|$ in the power of those terms.

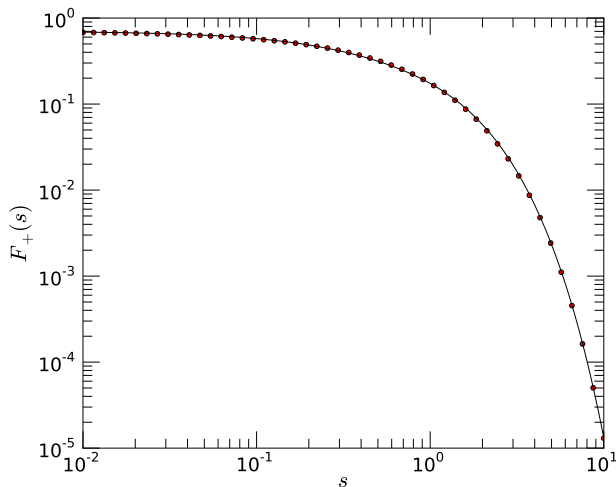


Figure 2.4: Fit to Painlevé Results at $T > T_c$ this is a fit to equation 2.24. Fit parameters $c = 1.73$, $b = 0.92$, $k = 3.8$. Red dots are Painlevé results, and the black line is the result of the fit.

Our form matches the exact solution to within 3.4% maximum relative error, with an average of 1.5% error, for the range of our fit $0.01 \leq s \leq 10$. (See figure 2.4).

Now let's turn our attention to the $T < T_c$ case. The philosophy for constructing the effective functional form is identical to the high temperature case, although for the disconnected correlation function, the long distance asymptote is dominated by the magnetization $\langle M \rangle^2$. For the connected correlation function $\langle \sigma_0 \sigma_r \rangle - \langle \sigma_0 \rangle \langle \sigma_r \rangle$, with the magnetization squared subtracted off, the long distance decay for the scaling function is $p_2 s^{-7/4} \exp(-2s)$, with $p_2 = 1/(2^{21/8} \pi)$. In our effective functional form, for simplicity, we choose to fit only the connected correlation function, interpolating between the short distance behavior and long distance decay, while adding the scaling magnetization squared to the result. (if one wishes, analytic corrections may be incorporated into the scaling magnetization as well). We use:

$$F_-^{fit}(s) = ((B(s))^{|k|} \cdot 0.700883)^k + ((1 - B(s))^{|k|} (p_2 s^{-7/4} \exp(-2s))^k)^{1/k} + 2^{3/8} s^{1/4} \quad (2.26)$$

Here,

$$B(s) = \exp(-(s/c)^b) \quad (2.27)$$

From fits, we find $c = 0.007 \pm 0.07$, $b = 0.4 \pm 2$, and $k = -0.2 \pm 0.1$. The fit is accurate to within 1% relative error; see figure 2.5. The fit is good to a maximum of 1% error when

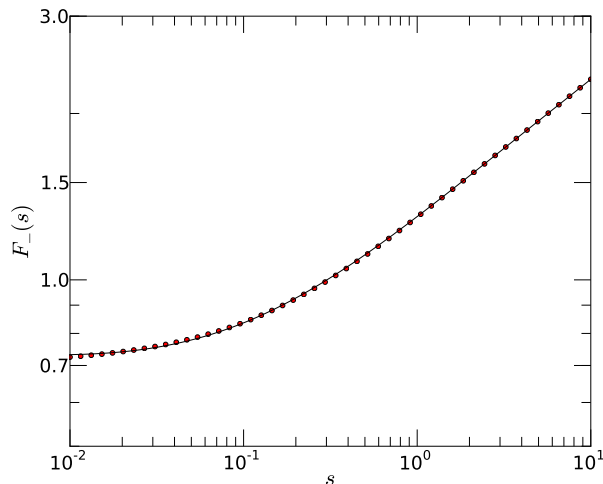


Figure 2.5: Fit to Painlevé Results at $T < T_c$ this is a fit to equation 2.26. Fit parameters are: $c = 3.62$, $b = 0.87$, and $k = -0.4$. The magnetization is separated out, so that we may subtract it off for the interpolation- which makes things less complicated. Red dots are Painlevé results, and the black line is the result of the fit.

compared against our Chebyshev form for the range of our fit $0.01 \leq s \leq 10$.

2.3.2 HIGH-PRECISION SCALING FORM FOR THE SUSCEPTIBILITY

We use a high-precision form of the susceptibility as an integration constraint for our functional form. The susceptibility was derived from the high-precision approximate

forms for the equation of state in Reference [26]. Using the parametric representation

$$t = \frac{T - T_c}{T} = R(1 - \theta^2) \quad (2.28)$$

$$h = H/T = h_0 R^{\beta\delta} h(\theta) \quad (2.29)$$

$$M = m_0 R^\beta \theta \quad (2.30)$$

the high-precision form for the equation of state,

$$h(\theta) = \left(\theta - \frac{\theta^3}{1.16951} \right) (1 - 0.222389\theta^2 - 0.043547\theta^4) \quad (2.31)$$

$$- 0.014809\theta^6 - 0.007168\theta^8). \quad (2.32)$$

and the definition $\chi = dM/dh$, we have:

$$\begin{aligned} \chi(R, \theta) = & R^{-7/4} m_0 (1 + (2\beta - 1)\theta^2) / (h_0 (1 - 0.482344\theta^2 - 0.0750424\theta^4 - 0.0262771\theta^6 \\ & - 0.0234342\theta^8 + 0.0385732\theta^{10} - 0.0444357\theta^{12})) \end{aligned} \quad (2.33)$$

2.3.3 ANALYTIC CORRECTIONS TO SCALING

The analytic corrections to scaling to the RG field u_t and u_h are given in coordinates of t and h in the literature. Since we give our function in parametric coordinates, here we provide forms for the corrections to be expressed in R and θ . In Section 2.2 we state that:

$$u_t = t(1 + c_t t + O(t^2)) \quad (2.34)$$

$$u_h = h(t + c_h t + O(t^2)). \quad (2.35)$$

Since $t = R(1 - \theta^2)$, R scales with t , so the first order corrections should also be linear in R . However, θ is not small as it can take any value from 0 to $\theta_c \approx 1.08144\dots$, so we will assume that

$$u_R = R(1 + g_1(\theta)R + O(R^2)) \quad (2.36)$$

$$u_\theta = \theta(1 + g_2(\theta)R + O(R^2)). \quad (2.37)$$

We can then solve for $g_1(\theta)$ and $g_2(\theta)$ using the Schofield definition:

$$\begin{aligned} g_1(\theta) = & (c_h \theta^3 (2 - 6.1549\theta^2 + 6.60301\theta^4 - 2.69648\theta^6 + 0.214502\theta^8 + 0.0351324\theta^{10} \\ & - 0.0135271\theta^{12} + 0.0122581\theta^{14}) + c_t \theta (1 - 6.23234\theta^2 + 13.4301\theta^4 - 12.7392\theta^6 \\ & + 5.00997\theta^8 - 0.343026\theta^{10} - 0.210889\theta^{12} + 0.152808\theta^{14} - 0.0674197\theta^{16})) / \\ & (\theta - 1.48234\theta^3 + 0.407301\theta^5 + 0.0487653\theta^7 + 0.00284291\theta^9 + 0.0620074\theta^{11} \\ & - 0.0830089\theta^{13} + 0.0444357\theta^{15}) \end{aligned} \quad (2.38)$$

$$\begin{aligned} g_2(\theta) = & ((c_h - \beta\delta c_t) (1 - \theta^2)^2 (\theta - 0.855059\theta^3) (1 - 0.222389\theta^2 - 0.043547\theta^4 \\ & - 0.014809\theta^6 - 0.007168\theta^8)) / (\theta - 0.482344\theta^3 - 0.0750424\theta^5 - 0.0262771\theta^7 \\ & - 0.0234342\theta^9 + 0.0385732\theta^{11} - 0.0444357\theta^{13}) \end{aligned} \quad (2.39)$$

2.3.4 ACCURACIES AND ERRORS

Here we report the quality our interpolation form in terms of average cost per data point, and average relative error per data point (See Equation 2.42) for each of the

simulation datasets at $R = 0.0336737$ with and without analytic corrections. We define the un-weighted residual to be:

$$r_j = D(j, \theta, R) - C(j, \theta, R) \quad (2.40)$$

where $D(j, \theta, R)$ is the data, $C(j, \theta, R)$ the interpolating form. The average cost per data point was calculated with the covariance matrix multiplying the residual:

$$cost = r_i \sigma_{ij}^{cov} r_j / N. \quad (2.41)$$

The relative error was measured as $\langle e_{rel}^2 \rangle$, where

$$e_{rel} = \frac{D(j, \theta, R) - C(j, \theta, R)}{C(j, \theta, R)}. \quad (2.42)$$

We may note that the relative error and cost do not necessarily reflect the same measure of theory quality. Relative error gives us a measure of the level of accuracy for the theory numbers, irrespective of how large the error bars are on the data. Cost, on the other hand, is weighted by the error of the data, and when the average cost is near or smaller than 1.0, the error is mainly caused by statistical fluctuations in the data. The higher the cost, the less well the theory is capturing the data to within error bars.

The accuracies in Table 2.1 and 2.2 were calculated for distances where the value of the disconnected correlation function $C(j, \theta, R) > 0.01$, this means skipping the points above $r = 44$ for $\theta = 0$, and $r = 51$ for $\theta = 0.1$. This is due to the fact that for $\theta = 0$ and $r > 44$, the errors are around 50% of the data value. We've also skipped the first 3 points of each data set due to the fact of short distance corrections dominated by lattice effects of higher-order analytic corrections to scaling. (see Section 2.4).

Notice in both tables that the special points $\theta = 0$ and $\theta = \theta_c$ whose exact results we interpolate between have a cost that is relatively small, and also that the corrections to

scaling improves the overall accuracy. As noted in the main text, the analytic corrections to scaling are small, and do not uniformly improve fits away from these special values. This is not surprising. Since the analytic corrections to scaling this close to the critical point are smaller than our interpolation errors in the scaling function, we might expect they would have cancelling effects roughly half the time. The analytic corrections should be of significant value farther from the critical point at all fields and temperatures.

2.4 SMALL DISTANCE DISCREPANCIES

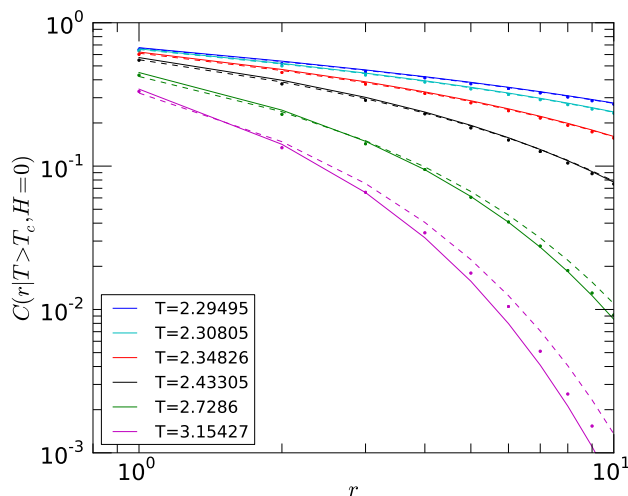


Figure 2.6: Small Distance Discrepancies for $T > T_c$, $H = 0$ This figure shows the small distance discrepancies for data along $T > T_c$, $H = 0$. The dashed line is the scaling theory, while the solid line is including all first order corrections in $a(T)$, $\xi(T)$, and u_t . One can see that the discrepancy between simulation data and theory gets smaller as the distance increases.

The scaling solutions differ from the numerical data at small distances, as shown in Figures 2.6, 2.7 and 2.8. We have investigated where this discrepancy stems from, by looking along the $H = 0$ axes where exact scaling solutions are known, and consistent with

θ	h	T	cost	error (%)
0	0	2.348260	0.5	2.85
0.10	1.612125e-04	2.347442	5.1	1.74
0.20	3.119619e-04	2.344991	2.9	3.55
0.30	4.420782e-04	2.340918	3.4	1.45
0.40	5.419973e-04	2.335240	3.8	2.72
0.50	6.031200e-04	2.327979	4.5	2.14
0.60	6.182554e-04	2.319166	5.1	0.91
0.70	5.822216e-04	2.308836	6.1	2.17
0.80	4.927350e-04	2.297031	8.7	1.96
0.90	3.518271e-04	2.283797	8.6	1.28
1.00	1.681982e-04	2.269185	0.7	0.20
1.01	1.481081e-04	2.267650	2.1	0.53
1.02	1.277970e-04	2.266102	2.4	2.58
1.03	1.072934e-04	2.264541	6.3	0.86
1.04	8.662751e-05	2.262967	6.8	1.00
1.05	6.583165e-05	2.261380	6.9	1.02
1.06	4.494000e-05	2.259780	5.5	0.92
1.07	2.398890e-05	2.258167	3.1	0.95
1.08	3.016912e-06	2.256541	1.0	0.19
θ_c	0	2.256306	3.6	0.85

Table 2.1: Cost and Errors for Interpolation The quality of our interpolation function is tabulated here in terms of average relative error (Equation 2.42) and average cost (Equation 2.41). For the calculation of this table, we skip the first 3 points (where lattice effects and higher-order corrections to scaling dominate) and data for $C < 10^{-2}$ (where the error is dominated by insufficient numerical statistics). (Note that the only data sets with values smaller than 10^{-2} are $\theta = 0$ and $\theta = 0.1$.) For $\theta = 0$, the statistical error becomes comparable to the data value once $C(r) < 0.01$, the error approaches 50% of the data value and exceeds that once $C(r) < 0.01$, and for $\theta = 0.1$ it approaches 5 – 10% after $C(r) < 0.01$. We expect our scaling form to be excellent in these large-distance regimes, where the corrections to scaling are negligible and the effects of the external field are small.

θ_{eff}	R_{eff}	cost	error (%)
0.0000000	0.0339815	0.8	1.81
0.0992207	0.0340277	1.4	1.43
0.1985608	0.0340413	1.1	2.91
0.2981203	0.0340234	1.2	2.11
0.3979613	0.0339790	1.4	1.95
0.4980952	0.0339168	1.3	1.41
0.5984751	0.0338478	1.3	1.28
0.6989978	0.0337834	1.6	1.52
0.7995184	0.0337330	1.5	1.49
0.8998839	0.0336999	1.4	1.34
1.0000000	0.0335563	0.1	0.14
1.0099992	0.0336703	0.5	0.53
1.0199971	0.0336664	2.0	2.49
1.0299941	0.0336619	0.9	0.95
1.0399909	0.0336568	1.0	1.06
1.0499883	0.0336507	1.1	1.10
1.0599874	0.0336434	0.9	0.91
1.0699899	0.0336345	0.7	0.74
1.0799981	0.0336234	0.6	0.56
1.0814389	0.0336216	0.4	0.43

Table 2.2: Cost and Errors with Corrections Here are the accuracies of the interpolation with all first order corrections (for $a(T)$, $\xi(T)$ u_t , and u_h) reported in terms of average relative error (Equation 2.42) and average cost (Equation 2.41). As in Table 2.1, we skip the first 3 points, and data below 10^{-2} . Note that with corrections the errors are smaller.

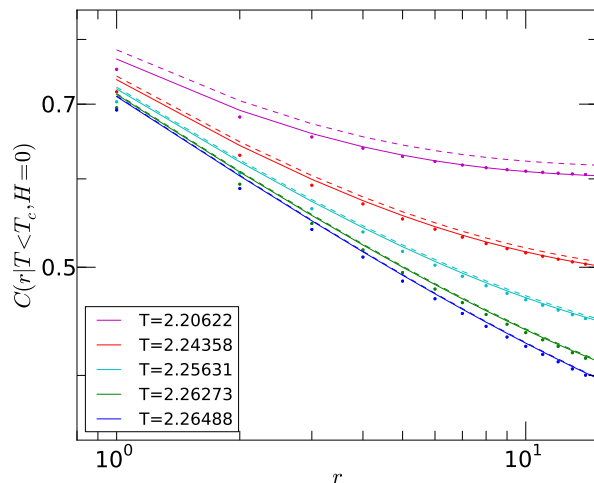


Figure 2.7: Small distance corrections for $T < T_c$, $H = 0$ This figure shows the small distance discrepancies for data along $T < T_c$, $H = 0$. The dashed line is the scaling theory, while the solid line is including all first order corrections in $a(T)$, $\xi(T)$, and u_t . One can see that the discrepancy between simulation data and theory gets smaller as the distance increases.

the literature we see no existence of singular corrections (which would be indicated by a power law), nor do we see a dependence between the discrepancy and the distance from the critical point. Most likely the small distance discrepancy is due to the fact that the form of the scaling solution goes as $C_{theory}(r) \sim a_0 r^{-1/4}$ for small distances, diverging as $r \rightarrow 0$, however for any data, $C_{data}(0) = 1.0$. Therefore, the ratio between the theory and data C_{theory}/C_{data} diverges as $r \rightarrow 0$. We attempted to multiply our function by $1/\exp(A/r)$ or equivalently $\exp(-A/r)$ with $A > 0$ to incorporate the lattice corrections, but a fit to with this correction does not noticeably improve the quality of our fit.

2.4.1 NUMERICAL METHODS: WOLFF ALGORITHM IN A FIELD

The Wolff algorithm [44] efficiently simulates the 2D Ising model in zero field, and requires small modifications to be used in non-zero magnetic field. In the usual Wolff algorithm,

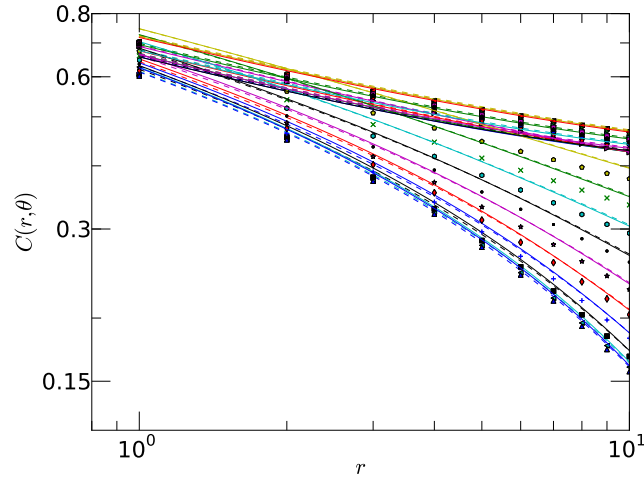


Figure 2.8: Small Distance Corrections for All Data This is a plot that shows the small distance discrepancies for all the data we included in matching our interpolation results. It is a larger version of the inset of 2.2, so that we may see the details of where the scaling theory fails.

which generates members of the ensemble of the Ising model in zero magnetic field, a random spin is chosen which 'seeds' a cluster. All of the nearest neighbors of this new cluster that have the same spin are then stochastically added to the cluster with the Wolff Probability, $P_{\text{Wolff}} = 1 - e^{-\beta J}$. The nearest neighbors of these new additions to the cluster are again added with the Wolff probability, and this process is iterated until a step adds no new spins to the cluster. At this juncture, the entire cluster is flipped. To implement a positive magnetic field, h , we distinguish between clusters which flip spins from up to down, and those that flip spins from down to up. Clusters that flip spins from down to up proceed as usual, but whenever an up spin is added to a down cluster, the entire cluster is rejected stochastically with probability $1 - \exp(-h)$. In implementing this algorithm, we were careful to use a predetermined number of proposed cluster flips, rather than a set number of spins, or successful cluster flips.

We implemented all of our simulations on 1024×1024 square lattices. Equilibration

times were conservatively estimated by waiting for many times the amount of time it takes for the magnetization to reach and then oscillate around its long time value. After equilibrating we determined the approximate correlation time- the number of proposed clusters that must on average be flipped to generate a new configuration whose magnetization is almost uncorrelated with the previous one. We generated 100 such independent configurations for each h and t value, and used these to estimate the correlation functions.

2.5 CONCLUSION

We have constructed a functional form for the spin-spin correlation function of the 2D Ising model at arbitrary temperature and field, which matches known analytical results at $H = 0$, and numerical simulations to high precision. By virtue of the real-space representation, comparing Ising predictions to laboratory experiments is reduced to the relatively simple matter of converting experimental parameters (such as biomembrane temperature and composition) to the Ising variables of temperature and magnetization or magnetic field or, equivalently, R and θ . This makes our functional form a robust tool for testing whether or not real systems fall into the Ising universality class

AVALANCHE SPATIAL STRUCTURE AND MULTIVARIABLE SCALING FUNCTIONS; SIZES, HEIGHTS, WIDTHS, AND VIEWS THROUGH WINDOWS ¹

We introduce a systematic method for extracting multivariable universal scaling functions and critical exponents from data. We exemplify our insights by analyzing simulations of avalanches in an interface using simulations from a driven quenched Kardar-Parisi-Zhang (qKPZ) equation. We fully characterize the spatial structure of these avalanches- we report universal scaling functions for size, height and width distributions, and also local front heights. Furthermore, we resolve a problem that arises in many imaging experiments of crackling noise and avalanche dynamics, where the observed distributions are strongly distorted by a limited field of view. Through artificially windowed data, we show these distributions and their multivariable scaling functions may be written in terms of two control parameters, the window size and the characteristic length scale of the dynamics. For the entire system and the windowed distributions we develop accurate parameterizations for the universal scaling functions, including corrections to scaling and systematic error bars, facilitated by a novel software environment *SloppyScaling*.

¹This chapter was published as: “Avalanche Spatial Structure and Multivariable Scaling Functions; Sizes, Heights, Widths, and Views through Windows”, Yan-Jiun Chen, Stefanos Papanikolaou, James P. Sethna, Stefano Zapperi, and Gianfranco Durin, *Phys. Rev. E* **84**, 061103 (2011)

3.1 INTRODUCTION

Systems that have crackling noise and avalanches exhibit scale invariance and power laws, which point to the notion of underlying universality [45]. These systems include many of the best-studied examples of non-equilibrium critical phenomena, and much progress has been made in a renormalization group context [13, 46]. The renormalization group implies that the long length and time behavior near critical points is governed by universal exponents and scaling functions. However, the predictive power of these theoretical studies has hitherto been underutilized; the primary focus of experiments and numerical simulations has been on precise estimates of critical exponents, rather than on the universal joint predictions of properties involving several control parameters and/or measured quantities.

A wide variety of materials and natural systems have been studied in the context of non-equilibrium critical phenomena. Many of these systems exhibit avalanches which have power law size distributions. These include Barkhausen noise in ferromagnets [7, 8, 47–49], fluid imbibition into porous media, flux-line depinning [13, 14, 50–53], and martensitic transformations [54, 55], to name a few. In the first three of these systems, avalanches are the result of the jerky motion of an interface (domain wall, fluid front, flux-line) in a disordered environment, and can be described by the same family of front-propagation models.

In this manuscript, we study the spatial structures of avalanches in a front-propagation model in two dimensions, developing tools and methods needed for systematic study and extraction of these multiparameter universal scaling functions. To illustrate the utility and importance of these functions, we apply them systematically to a practical experimental problem – the size distributions of avalanches seen through a viewing window. This problem illustrates (a) the complexity and sophistication of the different emergent size distributions,

(b) the relationships amongst the probability distributions of heights, widths, and sizes and their utility in generating predictions for windowed avalanches, and (c) the use of functional forms and least-squares fits to analyze and report on these multiparameter scaling functions.

Imaging experiments have been used in recent years to study a wide variety of systems exhibiting crackling noise or similar dynamics. Barkhausen noise is measured making use of the magneto-optical Kerr effect [6, 7, 47], allowing one to examine the domain wall motion in 2D thin films in real-time. In experiments on superconducting vortices [56], a magneto-optical (MO) setup is also used. In experiments of fracture [57], fluid imbibition [58] and granular systems [59, 60], the dynamics are also followed with a camera.

These visualization experiments provide an unusual opportunity: we now can study the universal properties of the spatial morphology – various distributions of heights, widths, angles, local heights, etc of either the avalanches or the fronts. However, the measurements of these properties are often distorted by a limited field of view. We hereby take this problem and develop the scaling theory for the universal functions needed to characterize the results of a generic imaging experiment – the distribution of avalanche sizes seen through windows.

The limited field of view in experiments distort the size distributions of avalanches, and cause difficulties in characterizing the critical exponents. Naturally, there is a bias towards small avalanches; large ones are cut off by the boundaries of the window. It can also distort the size distribution if pieces of large avalanches cut off by window boundaries are counted as small ones. Experiments have taken a variety of approaches to deal with such windowing effects: “Laser reflectometry” [6] on Barkhausen noise uses the magneto-optical Kerr effect, but lacking spatial resolution, lumps fragments and avalanches together; meanwhile, other

optical Kerr experiments have shown [47] that the effective size exponent τ for this lumped distribution depends strongly on the window width. Work by Kim *et al.* [61] report quite striking distributions but do not specify whether their data includes avalanches that touch the boundary. In experiments on superconducting vortices, or magnetic flux avalanches [56] avalanches exceeding a certain size are discarded. In fluid imbibition [58], the edges of the system are purposely left out to avoid any distortion produced by side walls. In granular systems, where avalanche dynamics in piles of rice are studied with real-time reconstruction [59, 60], and fracture experiments [57], where the dynamics are followed with a high-speed camera, boundary effects are not considered but may also be important.

We will show comprehensively how to analyze all of the size data lying within a window, and how to use the different classes of avalanches to get independent measures of various critical exponents. Indeed, window-width finite-size effects need not be avoided, but properly treated may provide additional measures of the critical exponents and the spatial structure.

Characterizing spatial structures of avalanches must go far beyond the traditional focus on critical exponents. Many experiments report power laws, however through this study we emphasize that one can make predictions about both power laws *and* scaling shapes from data, as has been demonstrated in a previous study of avalanche temporal shapes [62]. Indeed, traditional scaling collapse methods fail for functions of more than two variables. To optimally extract the behavior and estimate errors, we need to do simultaneous analysis of many different properties. We thus introduce a software environment, *SloppyScaling* [20], which facilitates the exploration and development of simultaneous fits of multiple data sets with parameterized forms of universal scaling functions. With this approach we are taking the first steps towards the use of scaling methods as a practical engineering tool.

3.2 SUMMARY OF KEY RESULTS

Since our theme is multifaceted, readers may be interested in focusing on different aspects of this work. In this section we present an overview of key results in this paper and a summary of their corresponding sections.

1. Universal spatial structures of avalanches in directed percolation depinning.

We provide a substantive analysis of the universal spatial morphology of avalanches in the quenched KPZ (qKPZ) model in 1+1 dimensions (the model is discussed in Section 3.3). Figure 3.1(a) shows avalanches in a typical simulation of this model. Analogous to magnetic systems, we have added a "demagnetization factor" k that parameterizes the restoring force, which allows us to access many metastable configurations of the front near the depinning transition, and controls the typical width of an avalanche, $L_k \sim k^{-\nu_k}$. Figure 3.2 shows examples of these resulting avalanches from simulations of various k . In Section 3.4, we thoroughly examine the spatial structure of the avalanches, including sizes s (the total area covered between pinned fronts, which would correspond to the total magnetization change in magnets, or the avalanche size of a rice pile), and also widths w and heights h (which measure the length of an avalanche in directions perpendicular and parallel to the direction of the motion of the front; this corresponds to studying the shapes of the magnetic domains or flux lines). We examine and fit the distributions of these sizes, heights and widths in Section 3.4.

2. Avalanches in Windows. As mentioned in the Introduction, in many imaging experiments the limited field of view distorts the avalanche size distribution. This is illustrated in Fig. 3.1(b) and (c). In Fig. 3.1(b) most of the avalanches are cut off by the left and right boundaries- if one were to count the area of these avalanches, we would count large ones as smaller ones. The resulting size distribution inside the window (dashed line of

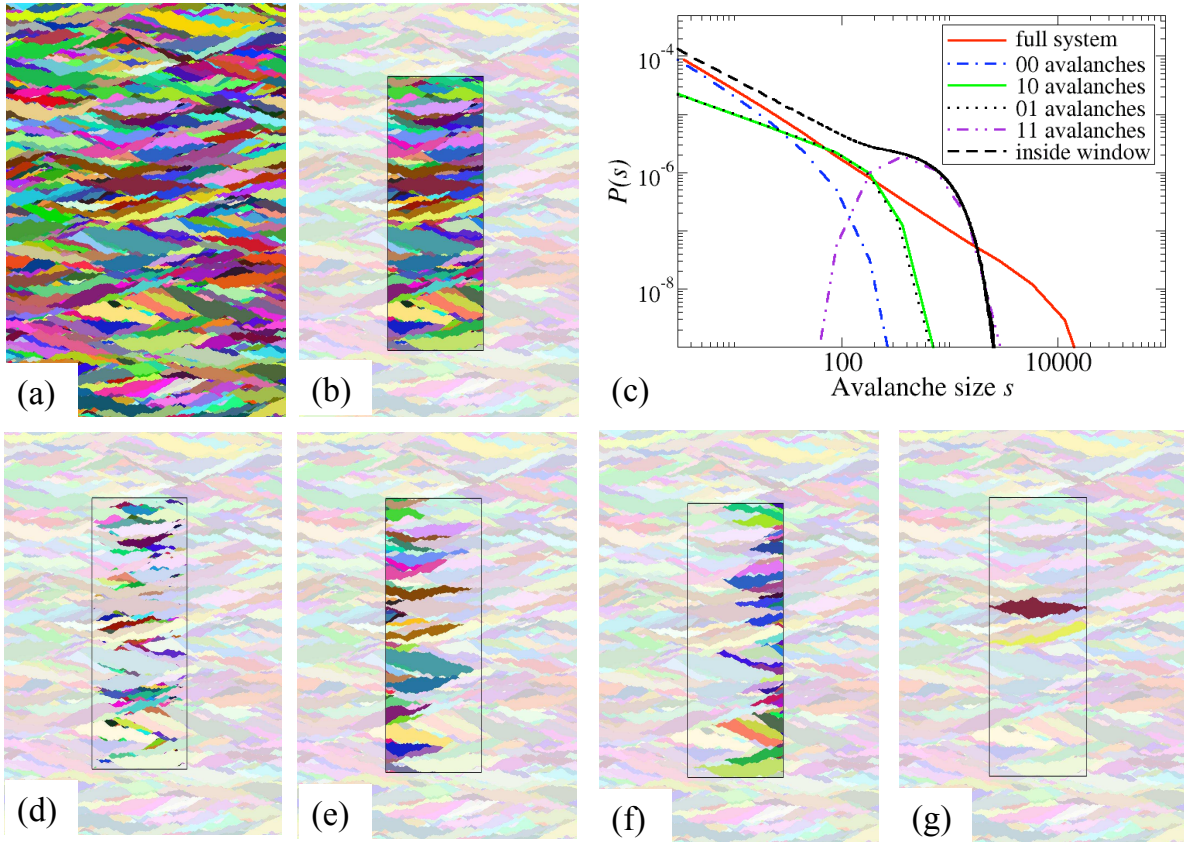


Figure 3.1: Windowed Distributions (a) The full system of avalanches. This figure shows a qKPZ simulation with avalanches. (b) A limited field of view: we can only see part of the system. The avalanches inside the artificial viewing window are brightly colored, and those outside are washed out. Notice that the avalanches within the window are cut off at top and bottom, and (more importantly for short, wide avalanches with roughness exponent $\zeta < 1$) on the two sides. (c) The size distributions for the different types of avalanches: (d) internal 00 avalanches, (e) split 10 avalanches, (f) split 01 avalanches, and (g) spanning 11 avalanches

Figure 3.1(c)) has a very different power law and shape compared to the full system distribution (solid line of Figure 3.1(c)).

In Section 3.5, we show in detail how avalanches which cross boundaries exhibit distinctly different size distributions and critical exponents. For simplicity, we consider a strip geometry where only the left/right boundaries are relevant (since avalanches in our system are flat and wide, few touch the top or bottom). We can therefore separate avalanches into four different categories, 00, 01, 10, and 11, depending on whether avalanches touch (1) or do not touch (0) the left or right boundaries: internal avalanches (00) (Figure 3.1(d)), split avalanches (10 and 01)(Figure 3.1(e) and (f)), and spanning avalanches (11) (Figure 3.1(g)). The internal (00) avalanches share the same power law as that of the full distribution, with a cutoff controlled by both the system size L_k and the window size W . The split (10 or 01) avalanches have a modified power law- a smaller exponent as larger avalanches are counted as smaller halves. (See Figure 3.1)(c)). The spanning avalanches also exhibit a smaller exponent, although this is not obvious in the shape of its scaling function. We can see that it has both an outer cutoff due to L_k and an inner cutoff due to the window size W , since avalanches must be large enough to span the window (purple dash-dotted line in Figure 3.1(c)). The internal and spanning avalanches also have distinct universal scaling functions with a cutoff controlled predominately by the window size for windows comparable to or smaller than the size of L_k . In Section 3.5 and Section 3.6 we give a thorough analysis of these modified power laws, the different scaling shapes, and the results of fits to data.

Having established a sophisticated method of analyzing both experimental and simulation data, we can utilize this analysis to enhance the collection of data in visualization experiments. Section 3.7 has some suggestions for how to collect data and simultaneously analyze the scaling behavior of different magnifications, and extract multiple exponents.

3. Functional forms A main emphasis of our work is that we fit an entire functional form instead of power laws [63], this includes the shape of the scaling function, and analytic and singular corrections to scaling. The benefit of approaching a scaling problem this way is that it allows us to account for both universal and non-universal effects in a consistent way. Writing down the functional form that is given by the data for a certain universality class will also be useful for identifying and characterizing other systems that are thought to belong to the same universality class.

We have found that, to analyze the windowed distributions, we need to first thoroughly examine the spatial structure of avalanches for the full system. In particular, in order to analyze the avalanche pieces left inside the window, we need to define height and width distributions and also joint distributions of sizes and widths. Section 3.4 discusses these and also the results of fits for such distributions for the qKPZ model we are studying. To focus on the scaling region, and minimize lattice effects, we will discuss these distributions in terms of *fractional area distributions*, $A(S) \propto SP(S)$, the average fraction of the system that a given size takes up.

A remarkable result is that size, height, and width distributions can be fitted with a nearly identical functional form. For example the size distribution is:

$$\begin{aligned} A(S|L_k) &= (S/L_k^{1+\zeta})^{2-\tau} \mathcal{A}_{S_k}(S/L_k^{1+\zeta})/S \\ &= S_k^{2-\tau} \exp((U_S S_k^{1/2} - Z_S S_k^{\delta_S}))/S. \end{aligned} \tag{3.1}$$

Here we have the shorthand $S_k = S/L_k^{1+\zeta}$. The width $A(w|L_k)$ and height $A(h|L_k)$ distributions are similar, with the form of $\frac{1}{X} Y^\alpha \mathcal{A}(\mathcal{Y})$, where $X = \{S, h, w\}$ and $Y = \{S/L_k^{1+\zeta}, h/L_k^\zeta, w/L_k\}$. $\mathcal{A}(\mathcal{Y})$ is identical in form to the one quoted above in Eq 3.1.

Fitting the size, height and width distributions at once, we can extract multiple exponents- not only the commonly measured size distribution exponent τ , but also the

exponent ν_k which, as mentioned in point 1, relates the typical width of an avalanche to k , and also the roughness exponent ζ . The roughness exponent ζ , which measures the fluctuations of the interface, is typically quoted for front propagation models as a means of characterizing the universality class. (In our analysis, we have found a range for the roughness exponent ζ (from 0.62 to 0.72) that differs from the literature value 0.63 [53]; we discuss this in Section 3.9.) One must note that the functional forms we choose are a practical tool to summarize existing information. While they may be inspired by analytical calculations, and chosen to be consistent with known asymptotics, they should be trusted only in the ranges over which they have been measured.

4. Multivariable scaling problems. The size distribution in Eq. 3.1 has a scaling form with one scaling variable. However, in this paper we will consider many scaling forms with more than one variable, such as a joint size and width distribution (3.4), or the windowed distributions (Section 3.5 and 3.6). In these cases, two or more scaling variables are important for describing the shape of the distribution (as seen in Figure 3.1(c)). For example, the general form for the 11 windowed distributions is:

$$A_{11}(s|W L_k) = \frac{1}{s} \left(\frac{s_k}{W_k} \right)^{(2-\tau)(1+\zeta)/\zeta} \mathcal{A}_{11}(s_k, W_k). \quad (3.2)$$

Here the scaling functions become distributions with two scaling variables, the rescaled size s_k and rescaled window width W_k . The traditional “scaling collapse” methods become problematic when multiple scaling variables are simultaneously important; this has hitherto retarded the effective study and use of these powerful universal joint distributions.

We present a systematic method for analyzing scaling problems with multiple control variables. In our problem, the two control parameters are the demagnetization factor k , and the window width W . We will show that the interplay between k and W is important for determining the shape of the avalanche size distributions. In particular, we can write

scaling functions for the distributions of the avalanche pieces in terms of these two scaling variables $s_k = s/L_k^{1+\zeta}$ and $W_k = W/L_k$ (as seen in Figure 3.1(c)). For example, the scaling function for the 11 distribution is:

$$\mathcal{A}_{11}(s_k, W_k) = \exp(-(T_{11} + U_{11}s_k^{1/2} + Z_{11}s_k^{\delta_{11}} + D_{11}\left(\frac{s_k}{W_k}\right)^{m_1} + C_{11}\left(\frac{s_k}{W_k^{n_{11}}}\right)^{-m_2}) \quad (3.3)$$

Section 3.6 discusses in detail the functions $\mathcal{A}_{00}(s_k, W_k)$, $\mathcal{A}_{10}(s_k, W_k)$, and $\mathcal{A}_{11}(s_k, W_k)$ that we consider. One may also find the results of fits (figures and tables of parameters) in Section 3.5.

5. SloppyScaling The analysis in this paper is done in the software environment *SloppyScaling* and includes a Bayesian analysis of systematic error bars, which are explained in Section 3.8.4. *SloppyScaling* allows us to fit data without collapses, which as mentioned above is problematic when there is more than one scaling variable involved. Included in the software setup are automatic fits of data to theory functions with nonlinear least-squares and ease of visualizing results. This software may be applied to many different multivariable scaling problems, making full use of universality and the predictions of the renormalization group. All of the fits in this paper and their corresponding figures (including axis labels) were generated directly and automatically using *SloppyScaling*.

3.3 MODEL

We use a model for imbibition fronts to produce avalanches, it is extensively studied, with well-established critical exponents.

We simulate crackling noise using a quenched KPZ model in 1+1 dimensions (see Section 3.8.1 for details on the implementation) [50], with dynamics given by:

$$\frac{\partial h(x, t)}{\partial t} = F - k\langle h \rangle + \gamma \nabla^2 h + \lambda (\nabla h)^2 + \eta(x, h) \quad (3.4)$$

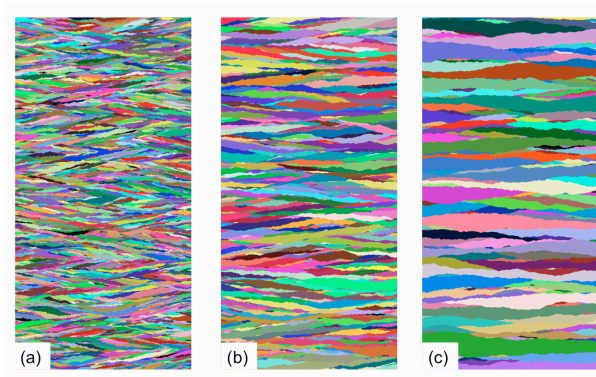


Figure 3.2: Scale Invariance in Crackling Noise. Three simulations of crackling noise, with different “demagnetization fields”, k . (a) $k = 10^{-5}$ (b) $k = 10^{-6}$ (c) $k = 10^{-7}$ (k is what controls the typical avalanche sizes in a given system, giving a characteristic width L_k .) Larger demagnetization fields stop avalanches more strongly, hence large k corresponds to smaller avalanches. The colored regions represent avalanches. The fronts are moving from bottom to top. Notice that the two simulations are statistically similar to one another apart from a rescaling of heights and widths. Note that most of the area is covered by the largest avalanches.

where $h(x, t)$ is the height of the front, F the driving force increasing quasistatically, linear and non-linear terms for the KPZ model controlled by the parameters γ and λ respectively, and η Gaussian quenched disorder. In the spirit of magnetic avalanche models [64], we have added a term analogous to a demagnetization field $-k\langle h \rangle$, which allows us to have pinned fronts at many metastable configurations. Models like these have been simulated [14] mostly near the depinning transition (and with $k = 0$). With $k \neq 0$, we define the area between each pinned front as an avalanche of size S . Avalanches produced by this model are thought to belong to the directed percolation depinning (DPD) universality class [53, 65]. The avalanches are self-affine, long and wide, with $\zeta < 1$. The roughness exponent ζ characterizes the ruggedness of the front, and also governs the scaling of avalanche heights h with widths w , $h \propto w^\zeta$ [14, 66]. In our model, k controls the typical size of the avalanche (Figure 3.2), the larger the k the smaller the typical size of an avalanche. We define the characteristic width of an avalanche in the full, unwindowed system to be $L_k = k^{-\nu_k}$. We

will write all the scaling forms in terms of the length L_k rather than the demagnetizing factor k directly to emphasize the analogies to finite-size scaling, as we are also studying finite *window* sizes compared to the size of L_k .

3.4 AVALANCHE SHAPES AND DISTRIBUTIONS OF THE FULL SYSTEM

In this section we will introduce various avalanche spatial distributions and their scaling forms. These forms will allow us to motivate the windowed distributions, and also serve as an example where traditional collapses may lead to questionable results.

3.4.1 AREA-WEIGHTED SIZE DISTRIBUTIONS

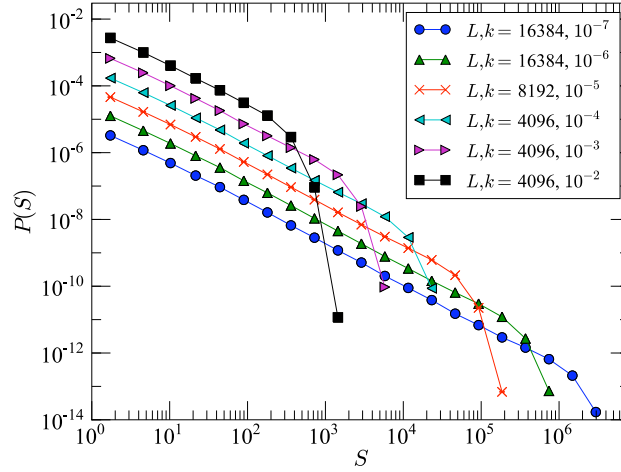
Traditionally, to describe an avalanche size distribution, we write the probability distribution as a power law times a universal scaling function. For example:

$$P(S|L_k) = S^{-\tau} \mathcal{P}(S/L_k^{1+\zeta}). \quad (3.5)$$

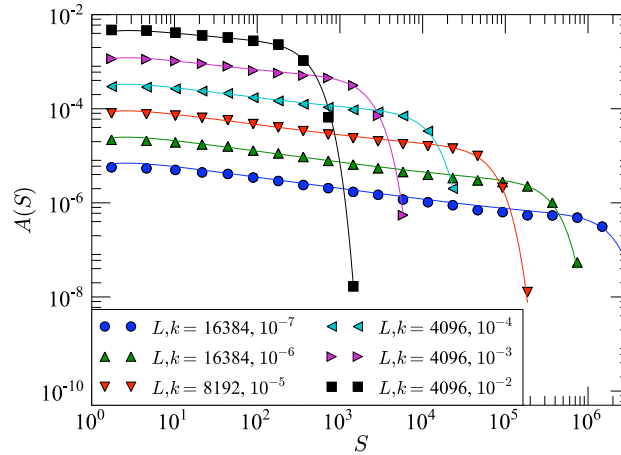
L_k is the characteristic width of an avalanche, and $h \sim L_k^\zeta$ the typical largest height, and therefore the appropriate scaling variable to describe the area of an avalanche is $S_k = S/L_k^{1+\zeta}$.

When studying the spatial properties as in our case, the probability distribution $P(S)$ (Eq. 3.5) is not the best choice, as its normalization is highly affected by non-universal effects at the lattice spacing (Figure 3.3). In fact, for $\tau > 1$, the normalization integral

$$N^{-1} = \int_{a^2}^{\infty} P(S|L_k) dS \sim \int_{a^2}^{L_k^{1+\zeta}} S^{-\tau} dS \sim a^{2(1-\tau)} - L_k^{(1-\tau)(1+\zeta)} \quad (3.6)$$



(a) Size Distribution (Probability)



(b) Area-weighted Size Distribution

Figure 3.3: $A(S)$ vs $P(S)$. Here one can see the difference between the more traditional $P(S)$ and the area-weighted $A(S)$. (a) $P(S)$: most of the area under the curve is from small avalanches, where non-universal lattice effects are important. (b) $A(S)$: the normalization is dominated by large avalanches, avoiding the lattice effects, so that we can focus instead on the dependence on the large scale cutoffs- L_k and, in later sections the window size. The data here is from qKPZ simulations of different k with different simulation size L . The lines in (b) are a result of a joint fit with the maximum height and width distributions. The fitting function and fitting parameters are shown in Table 3.1.

diverges at its lower (ultraviolet) limit $a \rightarrow 0$, but not for $L_k \rightarrow \infty$. Although we could study scaling functions that include a lattice cutoff, it is more interesting to focus on the large (infrared) avalanche cutoff, which depends on L_k in a universal way. To this end, it is more appropriate to make use of the first moment of $P(S)$, and to consider the *area-weighted size distribution* $A(S)$

$$A(S) \sim S \cdot P(S). \quad (3.7)$$

$A(S)dS$ has a natural physical interpretation: it is the fraction of the full system area covered by avalanches with sizes between S and $S + dS$. Its scaling form is thus:

$$\begin{aligned} A(S|L_k) &= L_k^{(\tau-2)(1+\zeta)} S^{1-\tau} \mathcal{A}_{Sk}(S/L_k^{1+\zeta}) \\ &= (S/L_k^{1+\zeta})^{2-\tau} \mathcal{A}_{Sk}(S/L_k^{1+\zeta})/S \\ &= S_k^{2-\tau} \mathcal{A}_{Sk}(S_k)/S. \end{aligned} \quad (3.8)$$

We use the subscripts Sk to distinguish the scaling of the size distributions governed by k from those governed by other control variables. The power of L_k we pull out of the scaling function is needed to normalize $A(S)$ to one, since $A(S)$ is sensitive to the long-distance cutoff. In particular,

$$\begin{aligned} N^{-1} &= \int_{a^2}^{\infty} A(S|L_k) dS = \int_{a^2}^{\infty} S_k^{2-\tau} \mathcal{A}_{Sk}(S_k)/S dS = \int_{a^2/L_k^{1+\zeta}}^{\infty} S_k^{2-\tau} \mathcal{A}_{Sk}(S_k)/S_k dS_k \\ &= \int_{a^2/L_k^{1+\zeta}}^{\infty} S_k^{1-\tau} \mathcal{A}_{Sk}(S_k) dS_k = \int_0^{\infty} S_k^{1-\tau} \mathcal{A}_{Sk}(S_k) dS_k - \int_0^{a^2/L_k^{1+\zeta}} S_k^{1-\tau} \mathcal{A}_{Sk}(S_k) dS_k \\ &\approx 1 - \mathcal{A}_{Sk}(0)(a^2/L_k^{1+\zeta})^{2-\tau} \approx 1 \end{aligned} \quad (3.9)$$

where the last integral converges for $\tau < 2$ ² and becomes small as L_k becomes large. Notice that the normalization of a power law must either diverge at the lower or at the upper

²All of the front propagation models have $1 < \tau < 2$, but we would need to use the second moment S^2 for the 3D nucleated RFIM [67], which has $\tau \sim 2.06$.

limit. By studying avalanches weighted by their first moment, the normalization depends explicitly on L_k , the infrared cutoff. This is the regime we are mainly interested in, since we would like to study the finite size effects imposed by both k and the window size W . Alternatively, as done in [68], one may also define a scale $S_m = \frac{\langle S^2 \rangle}{2\langle S \rangle}$, redefine the sizes as S/S_m and a corresponding $p(S/S_m)$ which has normalization $\int_0^\infty ds sp(s) = 1$. Here $p(s)$ is universal, but is also not a probability distribution in the conventional sense. This definition has an effect equivalent to what we do here: to make the function universal and insensitive to non-universal lattice effects on normalization. Namely, our definitions are related in the following way: $A(S) = \frac{S}{S_m^2} p(S/S_m)$ and $\mathcal{A}_{S_k}(S/S_m) = (S/S_m)^2 p(S/S_m)$. Here we use $S_m \equiv S_k = S/L_k^{1+\zeta}$, which is consistent with their definition of S_m up to a constant factor. We prefer to focus on the more directly interpretable fractional area distribution $A(S)$.

Furthermore, notice that we have been unorthodox in writing the scaling form (3.8) for $A(S|L_k)$ with a power of both L_k and of S outside the scaling function. Normally one factors out a single variable from the scaling function. For example, one could in principle write

$$A(S|L_k) = \frac{1}{S} \mathcal{B}_{S_k}(S_k). \quad (3.10)$$

In this form, $A(S|L_k) dS$ is invariant under rescaling, and also clearly preserves normalization. However, $\mathcal{B}(S_k) = S_k^{2-\tau} \mathcal{A}(S_k)$ vanishes as $S_k \rightarrow 0$, so this form of the scaling function disguises the power law behavior of the avalanche size distribution. By choosing the form \mathcal{A}_{S_k} which is defined to be finite and non-zero as $S \rightarrow 0$, we make manifest both the avalanche size dependence and the system size dependence.

3.4.2 MAXIMUM HEIGHT AND WIDTH DISTRIBUTIONS

In addition to the size distributions, we can also study the avalanche height and width distributions. We define height along the direction of front propagation, measuring the maximum height of an avalanche, and width perpendicular to heights, measuring the maximum width of an avalanche.

How do the height and width distributions scale? An avalanche of height h has size $S \approx h w \sim h h^{1/\zeta} = h^{(1+\zeta)/\zeta}$, so the system area $A(h|L_k)dh$ covered by avalanches with heights between h and $h + dh$ scales as

$$\begin{aligned}
 A(h|L_k)dh &\sim A(S|L_k)dS \\
 &= L_k^{(\tau-2)(1+\zeta)} S^{1-\tau} \mathcal{A}_{S^k}(S/L_k^{1+\zeta}) dS \\
 &= L_k^{(\tau-2)(1+\zeta)} h^{(1-\tau)(1+\zeta)/\zeta} \mathcal{A}_{h^k}(h/L_k^\zeta) dS
 \end{aligned} \tag{3.11}$$

and since $dS/dh \sim h^{1/\zeta}$,

$$\begin{aligned}
 A(h|L_k) &= L_k^{(\tau-2)(1+\zeta)} h^{(2-\tau)(1+\zeta)/\zeta-1} \mathcal{A}_{h^k}(h/L_k^\zeta) \\
 &= (h/L_k^\zeta)^{(2-\tau)(1+\zeta)/\zeta} \mathcal{A}_{h^k}(h/L_k^\zeta)/h \\
 &= h_k^{(2-\tau)(1+\zeta)/\zeta} \mathcal{A}_{h^k}(h_k)/h
 \end{aligned} \tag{3.12}$$

where $h_k = h/L_k^\zeta$ is the appropriate scaling variable to describe the avalanche height.

Similarly, we can write the scaling form for the width distributions as:

$$\begin{aligned}
 A(w|L_k) &= (w/L_k)^{(2-\tau)(1+\zeta)} \mathcal{A}_{w^k}(w/L_k)/w \\
 &= w_k^{(2-\tau)(1+\zeta)} \mathcal{A}_{w^k}(w_k)/w
 \end{aligned} \tag{3.13}$$

where $w_k = w/L_k$ is the scaling variable for widths.

Notice the pattern in all these formulas: $A(X|L)$ is a function with $\mathcal{A}(Y)$ of scaling variables (combinations of X and L invariant under the renormalization group rescaling) multiplying a power of the scaling variable, divided by the independent variable X , making $A(X|L)dX$ invariant under rescaling, allowing it to be universal.

3.4.3 JOINT FIT OF SIZE, HEIGHT AND WIDTH DISTRIBUTIONS

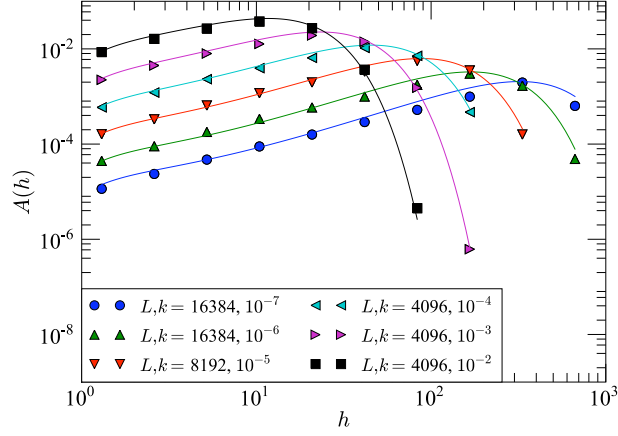
In Figs. 3.3(b), 3.4(a), 3.4(b) we show the size, height and width distributions for our qKPZ simulations at various k , and at different simulation sizes L . The curves are theoretical fits using a functional form of the type

$$\mathcal{A}(Y) = \exp(U_x Y^{1/2} - Z_x Y^{\delta_x}) \exp(A_1^x/x + A_2^x/x^2). \quad (3.14)$$

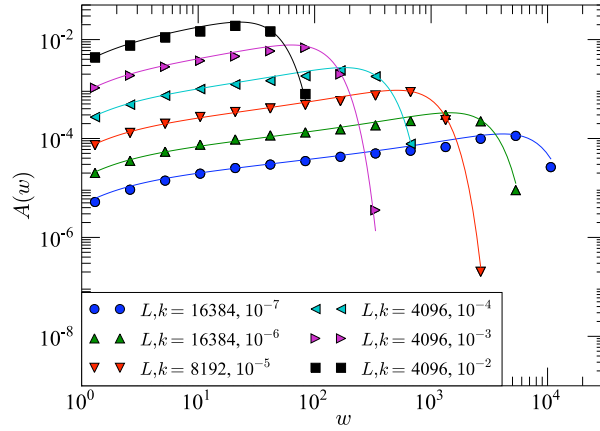
where $x = \{S, h, w\}$, and $Y = \{S_k, h_k, w_k\}$, and $U_x, Z_x, \delta_x, A_1^x, A_2^x$ are (5x3) fitting parameters (results are listed in Table 3.1). The first exponential term is the universal scaling function, while the second accounts for non-universal analytic corrections at small x due to lattice effects [67]. (See Section 3.8.5).

One may ask why we choose this particular scaling form. When fitting data to a function, there are many parameterizations we could use to describe the data. This form is motivated from a functional renormalization group expansion by Le Doussal and Wiese for static avalanche size distributions in a linear model [69]. Our model differs in that there is a nonlinear KPZ term leading to anisotropy, so that our avalanches belong to a different universality class, the DPD universality class.

Le Doussal and Wiese find the avalanche size distribution for the linear model, for all static universality classes (random-bond, random-field, and random-periodic), to



(a) Maximum heights



(b) Maximum widths

Figure 3.4: Area-weighted Avalanche Distributions for Maximum Heights and Widths Area-weighted avalanche distributions of (a) maximum heights, and (b) maximum widths for qKPZ simulations at different k , and simulation sizes L (dots are binned data). The critical exponents were jointly fit with the size distributions $A(S|L_k)$ of Fig. 3.3, using the scaling forms of Eqs. 3.12, 3.13, and 3.14. The best fit values for the critical exponents, parameters for universal scaling functions, and non-universal corrections are given in Table 3.1.

leading order in $d = 4 - \epsilon$ (where d is the dimension of the interface), to be:

$$P(S) \propto S^{-\tau} \exp(C(S/S_m)^{1/2} - \frac{B}{4}(S/S_m)^\delta) \quad (3.15)$$

Here their scaling form includes the large scale cutoff S_m . Le Doussal and Wiese claim that their results for both static and dynamic avalanches agree up to one loop for systems with $\zeta < 1$. Static avalanches are separated by equilibrium configurations (or ground states), and dynamic avalanches are connected through a sequence of metastable states. Our avalanches result from a moving interface near the depinning transition, so they belong to a dynamic universality class. We thus use Eq. 3.15 as inspiration for the scaling form of Eq. 3.14. However, one may note that there is no theoretical basis that it should work, since it is from a distinctly different universality class.

One cannot determine the values of ν_k and ζ independently, if we fit the size, height, or width distributions with Eqns. 3.8, 3.12, and 3.13 separately. For example in the size distribution we can only determine the combination $\nu_k(1 + \zeta)$. We determine the three critical exponents τ , ν_k , and ζ , by jointly fitting the size, height and width distributions.

The results of our fits are reported in Table 3.1 and shown in Figures 3.3(b) and 3.4. In particular, we find $\zeta = 0.62 \pm 0.02$ which is close to the highly-precise value of $\zeta = 0.63$ found in the literature [52, 66, 70–72]. We note that the parameters δ_x , which in principle control the asymptotic decay of the scaling function, are estimated here from a fit to the entire distribution. The quoted errors do not represent a confidence on the asymptotic decay - merely a confidence in the predictions over the range where data has been fit.

Finally, the respective scaling collapses for the size, height, and width distributions are shown in Figures 3.5, 3.6, and 3.7. Although scaling collapses are very useful in verifying critical behavior, we argue that they may be problematic for the purpose of determining critical exponents, and one should fit and make use of functional forms. In Section 3.8.5 we

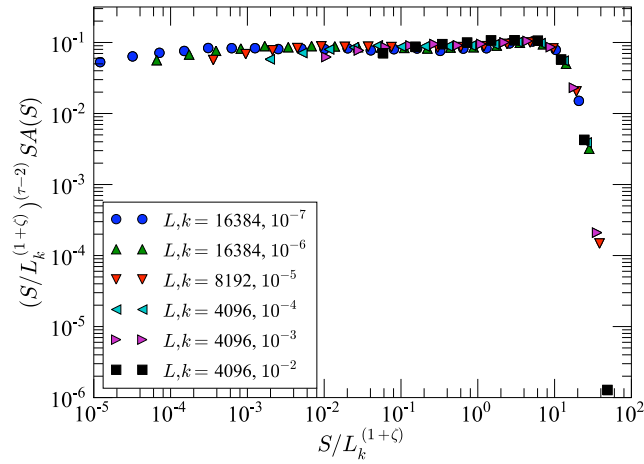


Figure 3.5: Size Distribution $A(S|L_k)$ Scaling Collapse We collapse the size distribution data using the universal exponents of $\tau = 1.24$, $\nu_k = 0.45$, and $\zeta = 0.62$, the best fit values of the joint fit between $A(S|L_k)$, $A(h|L_k)$ and $A(w|L_k)$.

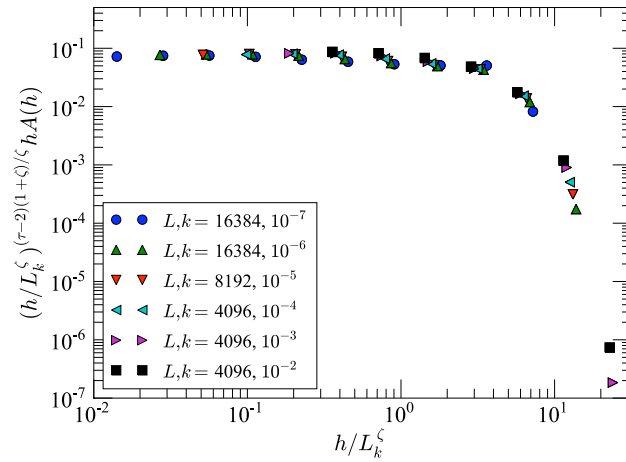


Figure 3.6: Height Distribution $A(h|L_k)$ Scaling Collapse We collapse the simulation data using the universal exponents of $\tau = 1.24$, $\nu_k = 0.45$, and $\zeta = 0.62$, the best fit values of the joint fit between $A(S|L_k)$, $A(h|L_k)$ and $A(w|L_k)$.

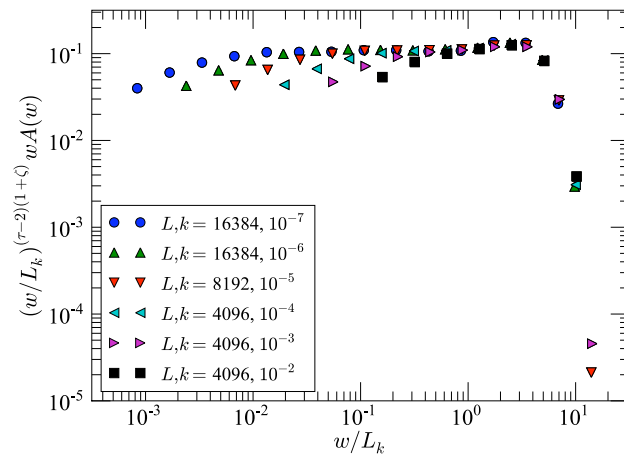


Figure 3.7: Width Distribution $A(w|L_k)$ Scaling Collapse We collapse the width distribution data using the universal exponents of $\tau = 1.24$, $\nu_k = 0.45$, and $\zeta = 0.62$, the best fit values of the joint fit between $A(S)$, $A(h)$ and $A(w)$.

parameter	best fit	standard errors in linear approx.	systematic errors
Universal Exponents			
Shared Exponents			
τ	1.2414	± 0.0006	± 0.04
ν_k	0.4513	± 0.0001	± 0.008
ζ	0.6155	± 0.0004	± 0.02
$\mathcal{A}_{S_k}(S_k) = \exp(U_S S_k^{1/2} - Z_S S_k^{\delta_S})$			
U_S	0.173	± 0.003	± 0.2
Z_S	0.0099	± 0.0002	± 0.01
δ_S	1.832	± 0.004	± 0.3
$\mathcal{A}_{h_k}(h_k) = \exp(U_h h_k^{1/2} - Z_h h_k^{\delta_h})$			
U_h	0.94	± 0.01	± 0.9
Z_h	0.307	± 0.004	± 0.3
δ_h	1.255	± 0.003	± 0.2
$\mathcal{A}_{w_k}(w_k) = \exp(U_w w_k^{1/2} - Z_w w_k^{\delta_w})$			
U_w	0.401	± 0.005	± 0.6
Z_w	0.0291	± 0.0004	± 0.2
δ_w	2.202	± 0.005	± 0.9
Non-Universal Exponents			
$\exp(A_1^x/x + A_2^x/x^2)$			
A_1^s	-0.36	± 0.03	± 2
A_2^s	-0.35	± 0.06	± 4
A_1^h	2.30	± 0.04	± 2
A_2^h	-1.90	± 0.04	± 2
A_1^w	-0.99	± 0.03	± 2
A_2^w	-0.06	± 0.03	± 1

Table 3.1: Best Fit Exponents and Parameters Here are the results of our joint fit for the size $A(S|L_k)$, width $A(w|L_k)$, and height $A(h|L_k)$ distributions. The corresponding universal scaling forms which were fit are quoted in the table alongside the parameter results; on the bottom of the table are multiplicative corrections for each distribution, with x equal to either S , w , and h . Here systematic error bars which account for errors in the theory (see Section 3.8.4 for explanation) are given. The traditional standard error bars are typically ~ 64 times smaller than the systematic error bars quoted; however, they are a gross underestimate of the actual errors expected since our theory is both highly nonlinear and sloppy [73]. We quote each parameter to the significant figure indicated by its standard error, since the parameters are strongly correlated, truncating each parameter to its significant figure would yield a poor fit.

will show how scaling collapses are unable to incorporate the effects of corrections to scaling, and how these corrections may cause a drift in the critical exponents.

3.4.4 LOCAL HEIGHT DISTRIBUTIONS

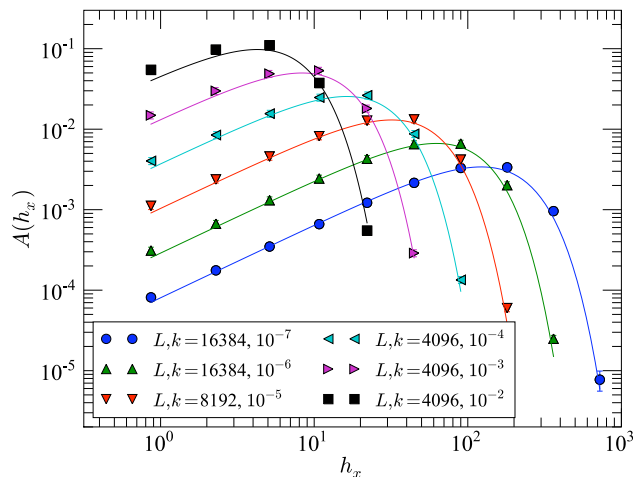


Figure 3.8: Area-weighted Local Height Distributions Here are the area-weighted local height distributions, the fraction of area taken up by a cross sectional height h_x . The fits shown in the figure were with the form of Eq. 3.16, where $\mathcal{A}_{h_x k}$ is the scaling function of the fit to 11 spanning avalanches (Eq: 3.33) which cross both window boundaries, taking $W = 0$. Details for this function are explained in Section 3.5.

In our analysis of the next section, we will make use of another scaling function of the same form: not the maximum height of an avalanche, but the *distribution* of heights given by random cross sections of avalanches. Let $A(h_x|L_k) dh_x$ be the fraction of the system area consisting of points (x, y) where the enclosing avalanche has vertical cross-sectional height at x in the range $(h_x, h_x + dh_x)$, then,

$$A(h_x|L_k) \sim (h_x/L_k^\zeta)^{(2-\tau)(1+\zeta)/\zeta} \mathcal{A}_{h_x k}(h_x/L_k^\zeta)/h_x. \quad (3.16)$$

This distribution gives a different measure of the typical shape of an avalanche. The local height distribution is shown in figure 3.8. Here the curves show a fit we have generated with a scaling function of the fit to 11 spanning avalanches (Eq 3.33) which cross both window boundaries, taking the limit of $W = 0$. Our best measure of the local heights is equivalent to a 11 distribution with window size 1. Details for how this works are provided in the Section 3.5.3.

3.4.5 JOINT DISTRIBUTIONS AND MULTIVARIABLE SCALING FUNCTIONS

Once we have distributions for the measures of size S , width w and height h , we can also explore the forms of joint distributions. The area $A(w, S|L_k) dS dw$ of avalanches in the range of size $(S, S + dS)$ and widths $(w, w + dw)$ will go to zero strongly if the size S becomes either much larger than or much smaller than the typical size $w^{1+\zeta}$ of an avalanche of width w – so we may factor out any combination of powers of w and S without changing the singularity. It still makes sense, though, to factor out the L_k -dependence. If we choose to factor out powers of S , therefore, we find

$$\begin{aligned}
 A(w, S|L_k) & \tag{3.17} \\
 &= \left(\frac{S}{L_k^{1+\zeta}} \right)^{2-\tau} \mathcal{A}_{wSk} \left(\frac{w}{S^{1/(1+\zeta)}}, \frac{w}{L_k} \right) \frac{1}{S S^{1/(1+\zeta)}} \\
 &= L_k^{(\tau-2)(1+\zeta)} S^{1-\tau-1/(1+\zeta)} \mathcal{A}_{wSk} \left(\frac{w}{S^{1/(1+\zeta)}}, \frac{w}{L_k} \right).
 \end{aligned}$$

where again we have a power of a dimensionless scaling variable, times a scaling function, divided by $Sw \sim SS^{1/(1+\zeta)}$ since $A(w, S|L_k)$ is multiplied by $dS dw$ in its invariant form.

The last joint distribution that will be useful is related to right-most pieces of an avalanche. Consider the right-most piece of width x of an avalanche of total width w and total size S ; let this segment have size s . (This will be the size measured by a window that

cuts the avalanche at the left-hand window boundary at x .) Let $A(s, w, S|x, L)$ be the fraction of the system covered by such avalanche pieces. Then, in the same logic as before, this five-variable distribution can be written as a power law times a universal function of four variables:

$$A(s, w, S|x, L) = L_k^{(\tau-2)(1+\zeta)} s^{-\tau-1/(1+\zeta)} \mathcal{A}_{swSxk} \left(\frac{x}{s^{1/(1+\zeta)}}, \frac{S}{s}, \frac{w}{S^{1/(1+\zeta)}}, \frac{w}{L_k} \right). \quad (3.18)$$

One can clearly work out scaling forms for joint distributions of several variables and other combinations. The ones we have discussed here will be needed in our analysis of windowing effects.

3.5 WINDOW EFFECTS

Now that we have laid the groundwork for exploring the shapes of avalanches, we focus on analyzing avalanches inside a viewing window. In this section, we focus on how to define the right power laws and scaling; we also give results for fits, extracting critical exponents. In the next section, we go into more detail about the scaling shapes of these distributions - the universal scaling *functions* for avalanche sizes viewed through windows.

In imaging experiments one often runs into the problem of not being able to see the whole system, distorting the avalanche size distribution. In particular, for Barkhausen noise, typical magnetic avalanches span many decades in size, far beyond the spatial resolution of optical microscopes. The natural solution is to take measurements at a variety of magnifications. Even though at the weakest magnifications the window size $W > L_k$ and most avalanches avoid the window boundaries, the effects of the boundaries will always dominate at the highest magnifications. The analysis in this section not only provides a

method to correct for finite-size-like window effects on exponents, but allows us to actively make use of all the data for a range of magnifications.

We show in detail in this section and the next how the avalanches which cross different boundaries exhibit distinctly different size distributions and critical exponents (Figure 3.1 and 3.9). As described in Section 3.2, we consider the avalanches measured in an infinite strip of width W (Figure 3.1(b)), for a system with characteristic length L_k . We separate avalanches into different categories: internal avalanches (00), split avalanches (10 and 01), and spanning avalanches (11). Let us call $A_{00}(s|W, L_k) ds$ the area fraction covered by such avalanches with sizes in the range $s, s + ds$. (For A_{00} , the segment size equals the total size.) The split (10 or 01) avalanches will have area fraction $A_{10}(s|W, L_k) ds$ for each s . The distribution A_{01} (Figure 3.1(f)) of avalanches touching the right boundary naturally equals A_{10} on average. $A_{11}(s|W, L_k) ds$ is the fraction of the strip spanned by 11 spanning avalanches. We mentioned in Section 3.2 that the 00 avalanches have a power law that matches the full system, whereas the 10, 01, 11 avalanches all have modified power laws with a smaller exponent τ .

Besides different power law scaling, the universal scaling functions for these different avalanche distributions are also distinct. In particular, the cutoff dependence on window size is different for internal avalanches and split avalanches, while the spanning avalanches have both an outer and an inner cutoff due to the window size (since avalanches must be large enough to span the window). We present the fits of these universal scaling functions in this section and discuss their shapes in more detail in the next.

We know that all avalanches in the window are of one of the 00, 10, 01, 11 types, so

$$\int ds A_{00}(s|W, L_k) + 2A_{10}(s|W, L_k) + A_{11}(s|W, L_k) = 1. \quad (3.19)$$

As in the previous section, consider how each of these distributions A_{zz} rescales under

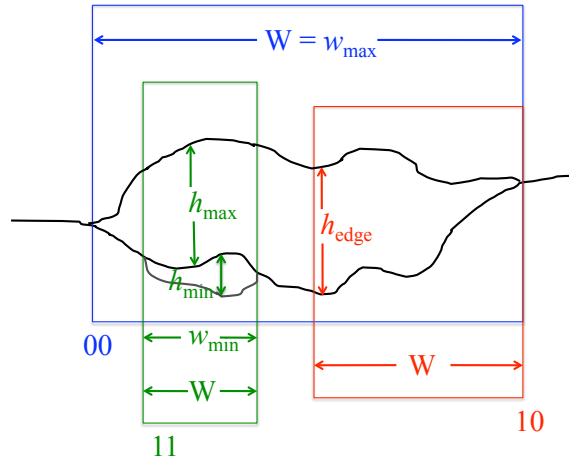


Figure 3.9: An Avalanche Cut by Windows in the Extreme Limits. Drawn here are two fronts separated by an avalanche event. Here we are depicting cases where this avalanche (or its segment) is the maximum avalanche size for the 00, 10, and 11 at different window widths. Boxes of different widths and colors are used to show the cases in which this may happen. The main avalanche may count as a 00 avalanche for a wide window, while part of it would count as a 11 avalanche for a smaller window; it could also count as a 10 avalanche if it happens to cross the window boundary. This figure illustrates our arguments for the shape of the cutoff (the exponent n_{zz}) given a window size W for the 00, 11, 10 cases. Another small avalanche is drawn for the 11 case to show that the minimum size to cross the 11 window also introduces a separate cutoff.

a coarse-graining by a factor b . The zz denote our indices for the various windowed distributions (00, 10, 01, 11). Each $A_{zz}ds$, being a geometrical quantity (a fractional area), must be invariant under rescaling (with two invariant scaling variables):

$$\begin{aligned} A_{zz}(s|W, L_k) ds &= A_{zz}(s/b^{1+\zeta}|W/b, L_k/b) ds/b^{1+\zeta} \\ &= (1/s)\mathcal{B}_{zz}(s/L_k^{1+\zeta}, W/L_k) ds. \end{aligned} \quad (3.20)$$

However, this is clearly not the form which makes the size and window-width dependence of the avalanche sizes manifest. We are allowed to factor powers of the invariant scaling variables W/L_k and $s/L_k^{1+\zeta}$ out of the scaling function \mathcal{B} :

$$\begin{aligned} A_{zz}(s|W_k, L_k) &= \frac{1}{s} \left(\frac{s}{L_k^{1+\zeta}} \right)^{2-\tau_{zz}} \left(\frac{W}{L_k} \right)^{-v_{zz}} \mathcal{A}_{zz} \left(\frac{s}{L_k^{1+\zeta}}, \frac{W}{L_k} \right) \\ &= L_k^{(\tau_{zz}-2)(1+\zeta)+v_{zz}} W^{-v_{zz}} s^{1-\tau_{zz}} \mathcal{A}_{zz} \left(\frac{s}{L_k^{1+\zeta}}, \frac{W}{L_k} \right). \end{aligned} \quad (3.21)$$

The appropriate powers of s , L_k , and W to pull outside depend upon which of the three distributions we are considering. For the distributions A_{00} and A_{10} , A_{01} , we choose τ_{zz} and v_{zz} (powers of the invariant scaling variables $X = s/L_k^{1+\zeta}$ and $Y = W/L_k$) to make the resulting scaling function go to a constant at small X and/or Y . This way the power laws we pull out describe the behavior of the limit of small s , and the way in which the avalanches are cut off by the window size (as s approaches $W^{1+\zeta}$) are described by the scaling function. On the other hand for A_{11} there are no small avalanches (they have to be large enough to span the window), and as $L_k \rightarrow \infty$, all avalanches span the window and become 11 avalanches, and in this limit the distribution will not go to zero, so for this distribution we instead pull out powers of W and s .

3.5.1 INTERNAL AVALANCHES

First let us consider $A_{00}(s|W, L_k)ds$, the window area spanned by avalanches of sizes in $(s, s + ds)$ that do not touch the boundaries. This can be computed explicitly from the function $A(w, S|L_k)$ (Eq. 3.17) which gives the area covered by avalanches of width w and size S (note that for 00 avalanches, the segment pieces $s = S$):

$$\begin{aligned}
A_{00}(s|W, L_k) &= \int_a^W \frac{W-w}{W} A(S, w|L_k) dw \\
&= \int_a^W dw \frac{W-w}{W} L_k^{(\tau-2)(1+\zeta)} S^{1-\tau-1/(1+\zeta)} \mathcal{A}_{wSk} \left(\frac{w}{S^{1/(1+\zeta)}}, \frac{w}{L_k} \right) \\
&= L_k^{(\tau-2)(1+\zeta)} S^{1-\tau-1/(1+\zeta)} \int_a^W dw \frac{W-w}{W} \mathcal{A}_{wSk} \left(\frac{w}{S^{1/(1+\zeta)}}, \frac{w}{L_k} \right) \quad (3.22)
\end{aligned}$$

where $(W-w)/W$ is the probability that an avalanche whose center lies within the window is entirely contained in the window (i.e., the avalanche center lies within $(W-w)/2$ of the center of the window). Changing variables from w to $\Omega = w/s^{1/(1+\zeta)}$,

$$\begin{aligned}
A_{00}(s|W, L_k) &= L_k^{(\tau-2)(1+\zeta)} s^{1-\tau} \int_{a/s^{1/(1+\zeta)}}^{W/s^{1/(1+\zeta)}} d\Omega \frac{W - s^{1/(1+\zeta)}\Omega}{W} \mathcal{A}_{wSk} \left(\Omega, \Omega \left(\frac{s}{L_k^{1+\zeta}} \right)^{\frac{1}{(1+\zeta)}} \right) \\
&= L_k^{(\tau-2)(1+\zeta)} s^{1-\tau} \mathcal{A}_{00}(s/W^{1+\zeta}, W/L_k), \quad (3.23)
\end{aligned}$$

with no explicit dependence on the window width W (so $\nu_{00} = 0$), and the same critical exponent $\tau_{00} = \tau$ that is given by the non-windowed distribution. Note that Eq. (3.23) is of the general form given by Eq. (3.20) and (3.21). This scaling equation is also consistent with our numerics: the normalization of the distribution for small avalanches is independent of W , and $\tau_{00} = 1.26 \pm 0.02$ is consistent with the bulk $\tau = 1.24 \pm 0.04$.

Using this scaling form, we fit the 00 data (jointly with 11 and 10 data) with a scaling

function given by a parameterized functional form:

$$A_{00}(s|W, L_k) = L_k^{(\tau-2)(1+\zeta)} s^{1-\tau} \exp(-(T_{00} + U_{00}s_k^{1/2} + Z_{00}s_k^{\delta_{00}} + C_{00}(\frac{s_k}{W_k^{n_{00}}})^{m_{00}}) \exp((A_1^{00}/s + A_2^{00}/s^2)) \quad (3.24)$$

with $s_k = s/L_k^{(1+\zeta)}$. Our fit for the parameter n_{00} is 1.62, which we believe to be $1 + \zeta$ (see next section). This makes the term $s_k/W_k^{n_{00}} = S/W^{1+\zeta}$ which is another natural invariant scaling variable.

Figure 3.10 shows the results of a nonlinear least squares fit, with shaded areas as estimations of fluctuations in the theory corresponding to systematic error bars on our parameters. In Eq. 3.24, τ , ζ , (and ν_k which is hidden in L_k) are universal exponents shared amongst the three different distributions, A_1^{00} and A_2^{00} are (non-universal) analytic corrections to scaling reflecting lattice effects on small avalanches, and the other parameters encapsulate the shape of the universal scaling function \mathcal{A}_{00} . The fitted results for the other universal and non-universal parameters are quoted in Table 3.2. We describe the scaling shapes and their motivation in more detail in Section 3.6.

One may note the exponent ζ in our fits is fixed to the literature value of 0.63. If we allow for a free fit on all the parameters, it shifts to $\zeta = 0.68 \pm 0.02$. Although the free fit is 2.5σ away from the accepted value of ζ , the fit with fixed $\zeta = 0.63$ has only a 50% higher cost than the free fit minimum, suggesting an average of 0.5σ drift on the parameters instead of 2.5σ as seen in Table 3.2. This suggests three cautions (1) The estimate on our systematic error (0.02) is a lower bound estimate, and in fact the systematic error should be higher. (2) The fact that our systematic error should be higher also implies that the scaling functions are imperfect and may be improved upon. (3) There could be corrections due to a crossover that depends on both λ and k which we have not accounted for, which are

distorting the fit. The subtleties and nuances in measuring the exponent ζ , and the possible origins of this drift are discussed in more detail in Section 3.9.

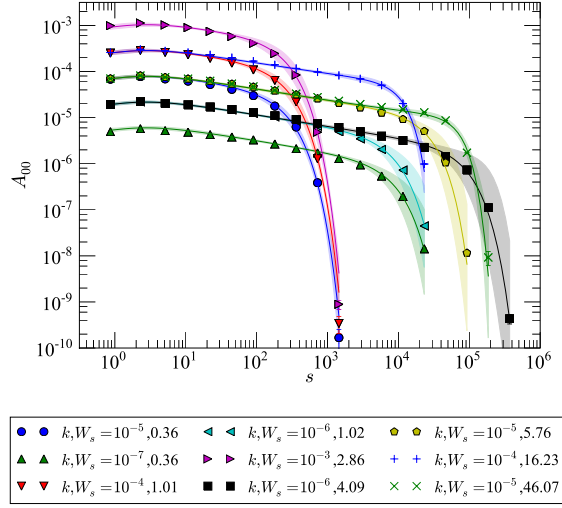


Figure 3.10: Internal Avalanches Data and Fit Shown here are the area-weighted size distributions for internal (00) avalanches. The lines are the joint best fit of A_{00} , A_{10} and A_{11} to the functional forms of equations 3.24, 3.27, and 3.33, whereas the shaded areas are the fluctuations in theory corresponding to the systematic covariant errors on our exponents and parameters (individual parameter best fit values and errors are quoted in Table 3.2).

3.5.2 SPLIT AVALANCHES

Next, consider the avalanches that are split by one side of the window, say the left side, with the distribution $A_{10}(s|W, L_k)$. Physically, for small avalanches s and large L_k/W this is clearly proportional to $1/W$: the small avalanches extend only a small distance into

the window (smaller than the window width), so the fractional area covered by them is proportional to one over the width of the window. This leaves us with a scaling form

$$A_{10}(s|W, L) = \tag{3.25}$$

$$\frac{1}{W} L^{(\tau'-2)(1+\zeta)} s^{1-\tau'+1/(1+\zeta)} \mathcal{A}_{10}(s/L_k^{1+\zeta}, W/L_k).$$

with τ' to be determined. Note again that Eq. (3.25) is of form Eq. (3.20).

We can also write A_{10} in terms of the distribution of right-most pieces $A(s, w, S|x, L_k)$ from Eq. 3.18, integrating over all possible sizes S , all possible widths w , and all possible pieces x (from lattice size a to window width W):

$$\begin{aligned} A_{10}(s|W, L_k) &= \int_{a^2}^{\infty} dS \int_a^{\infty} dw \int_a^W \frac{dx}{W} A(s, w, S|x, L_k) \\ &\sim \left(\frac{s}{L_k^{1+\zeta}} \right)^{2-\tau} \frac{1}{s^2 s^{1/(1+\zeta)}} \int_{a^2}^{L_k^{1+\zeta}} dS \int_a^{L_k} dw \int_a^W \frac{dx}{W} \mathcal{A}_{swSxk} \left(\frac{x}{s^{1/(1+\zeta)}}, \frac{S}{s}, \frac{w}{S^{1/(1+\zeta)}}, \frac{w}{L_k} \right) \\ &= \left(\frac{s}{L_k^{1+\zeta}} \right)^{2-\tau} \frac{1}{s} \int_{a^2/s}^{L_k^{1+\zeta}/s} d \left(\frac{S}{s} \right) \int_{a/s^{1/(1+\zeta)}}^{L_k/s^{1/(1+\zeta)}} d \left(\frac{w}{s^{1/(1+\zeta)}} \right) \\ &\quad \times \int_{a/s^{1/(1+\zeta)}}^{W/s^{1/(1+\zeta)}} \frac{s^{1/(1+\zeta)}}{W} d \left(\frac{x}{s^{1/(1+\zeta)}} \right) \mathcal{A}_{swSxk} \left(\frac{x}{s^{1/(1+\zeta)}}, \frac{S}{s}, \frac{w}{S^{1/(1+\zeta)}}, \frac{w}{L_k} \right) \\ &= \frac{1}{W} L_k^{(\tau-2)(1+\zeta)} s^{1-\tau+1/(1+\zeta)} \mathcal{A}_{10}(s/L_k^{1+\zeta}, W/L_k) \end{aligned} \tag{3.26}$$

dx/W is the relative probability that the avalanche intersects the left-hand boundary, and we have changed the integration limits at ∞ to the avalanche length scale L_k . (For $w < x < W$, the original distribution is naturally zero.) After we rewrite the integration variables in terms of the invariant scaling variables, we can organize the form of the scaling function into the form of Eq. 3.25. This tells us that $\tau' = \tau$. These results are consistent with our numerical fits: W has an exponent of minus one, and τ' is equal to the system τ .

With the correct power laws pulled out, we can now write down a function to describe

the data and cutoff:

$$A_{10}(s|W, L_k) = \frac{1}{W} L_k^{(\tau-2)(1+\zeta)} s^{1-\tau+1/(1+\zeta)} \exp(-(T_{10} + U_{10}s_k^{1/2} + Z_{10}s_k^{\delta_{10}} + C_{10}(\frac{s_k}{W_k^{n_{10}}})^{m_{10}})) \exp((A_1^{(10)}/s + A_2^{(10)}/s^2)) \quad (3.27)$$

Again, our best fit n_{10} is nearly $1 + \zeta$, so $s_k/W_k^{n_{10}} \sim s/W^{1+\zeta}$. Also note that this distribution has the same functional form as A_{00} in eqn 3.24 aside from a factor of $s^{1/(1+\zeta)}/W$ in front.

Figure 3.11 shows the results of a joint nonlinear least squares fit with the 00 and 11 avalanche data, with shaded areas representing estimations of fluctuations in the theory corresponding to systematic error bars on our parameters. Here, as in the 00 distributions, τ , ζ (and ν_k which is included in L_k and the scaling variables s_k and W_k) are universal exponents shared amongst the three different distributions, A_1^{10} and A_2^{10} are (non-universal) analytic corrections to scaling reflecting lattice effects on small avalanches, while the other parameters describe the shape of the universal scaling function $\mathcal{A}_{10}(s_k, W_k)$. Fitted results for the other universal and non-universal parameters are quoted in Table 3.2. We describe the scaling shape and its motivation in more detail in section 3.6.

3.5.3 SPANNING AVALANCHES

Finally, consider the spanning avalanche distribution A_{11} . First, remember that most of the area in general is spanned by the largest avalanches (since $\tau < 2$). Therefore, as $L_k \rightarrow \infty$, 100% of the area is covered by avalanches of widths much larger than W , and hence A_{11} must integrate to one in this limit. This makes it natural to pull out only powers of W and s outside the scaling form for A_{11} .

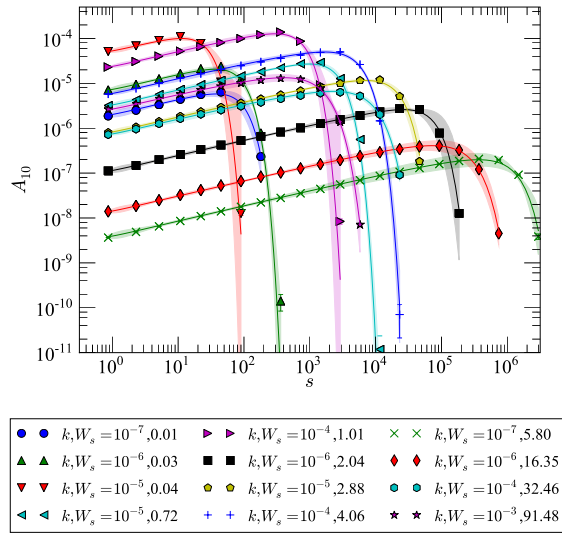


Figure 3.11: Split Avalanches Data and Fit. Shown here are the area-weighted size distributions for split (10) avalanches with different k and window size W . The lines are the joint best fit of A_{00} , A_{10} and A_{11} to equations 3.24, 3.27, and 3.33, whereas the shaded areas are the fluctuations in theory corresponding to the covariant systematic errors on our exponents and parameters (individual parameter best fit values and errors Table 3.2).

Second, notice that the size of an 11 avalanche is basically given by its height. More specifically, as $W \rightarrow 0$, the avalanches have size $s = Wh_x$, where h_x is the height of the vertical cross section of the avalanche. Hence we can write A_{11} in the limit $W \rightarrow 0$ in terms of the distribution $A(h_x|L_k)$ of randomly chosen vertical cross sections of avalanches (eqn 3.16), choosing $h_x = s/W$:

$$\begin{aligned} A_{11}(s|W=0, L_k) ds &\sim_{W \rightarrow 0} dh_x A(h_x=s/W|L_k) \\ A_{11}(s|W=0, L_k) &\sim_{W \rightarrow 0} \frac{1}{W} A(h_x=s/W|L_k) \end{aligned} \quad (3.28)$$

where $dh_x/ds = 1/W$. Remembering from Eq. (3.16) that

$A(h_x|L_k) \sim (h_x/L_k^\zeta)^{(2-\tau)(1+\zeta)/\zeta} \mathcal{A}_{h_x k}(h_x/L_k^\zeta)/h_x$, we substitute s/W for h_x and take the limit of $W_k \rightarrow 0$ in Eq. 3.28 to give:

$$A_{11}(s|W=0, L_k) \sim_{W_k \rightarrow 0} \frac{1}{W} \left(\frac{s}{W L_k^\zeta} \right)^{(2-\tau)(1+\zeta)/\zeta} \mathcal{A}_{h_x k} \left(\frac{s}{W L_k^\zeta} \right) / (s/W), \quad (3.29)$$

we cancel the two W 's and add the dependence on the second scaling variable $W_k = W/L_k$ to derive the scaling form for A_{11} :

$$A_{11}(s|W, L_k) = \frac{1}{s} \left(\frac{s}{W L_k^\zeta} \right)^{(2-\tau)(1+\zeta)/\zeta} \mathcal{A}_{11} \left(s/(W L_k^\zeta), W/L_k \right). \quad (3.30)$$

Here $\lim_{Y \rightarrow 0} \mathcal{A}_{11}(X, Y) = \mathcal{A}_{h_x k}(X)$ and thus $\int \mathcal{A}_{11}(X, 0) dX = 1$ (implied by the fact that almost all avalanche area touches both boundaries as $W/L_k \rightarrow 0$). Also notice that since:

$$X = \frac{s}{W L_k^\zeta} = \frac{s}{L_k^{(1+\zeta)}} \frac{L_k}{W} = s_k \cdot \frac{1}{W_k}, \quad (3.31)$$

we can rewrite $A_{11}(s|W, L_k)$ as:

$$A_{11}(s|W, L_k) = \frac{1}{s} \left(\frac{s_k}{W_k} \right)^{(2-\tau)(1+\zeta)/\zeta} \mathcal{A}_{11} \left(\frac{s_k}{W_k}, W_k \right). \quad (3.32)$$

Figure 3.12 shows the results of a joint fit with the simulation data of the previous 00 and 10 distributions. For the 11 distributions we use the functional form:

$$A_{11}(s|W L_k) = \frac{1}{s} \left(\frac{s_k}{W_k} \right)^{(2-\tau)(1+\zeta)/\zeta} \exp \left(- \left(T_{11} + U_{11}s_k^{1/2} + Z_{11}s_k^{\delta_{11}} + D_{11} \left(\frac{s_k}{W_k} \right)^{m_1} + C_{11} \left(\frac{s_k}{W_k^{n_{11}}} \right)^{-m_2} \right) \right) \exp(A_1^{(11)}/s) \quad (3.33)$$

τ (and also ζ and ν_k which are hidden in the scaling variables s_k and W_k) are universal exponents shared amongst the three different distributions, A_{11}^1 is the (non-universal) analytic correction to scaling reflecting lattice effects on small avalanches, while the other parameters describe the shape of the universal scaling function $\mathcal{A}_{11}(s_k, W_k)$. Note that we don't include the term A_{11}^2 , as we have done in the 00 and 10 distributions; this term turns out to be the same as another term in the universal scaling function in the limit of $W \rightarrow 0$, and so it is redundant. (See Section 3.8.5). The best fit universal and non-universal parameters are given in Table 3.2. We discuss in more detail the motivation and form of the scaling function $\mathcal{A}_{11}(X, Y)$ in Section 3.6.

We also test the limiting case of our scaling function with our data sets of $W = 1$ in Figure 3.8 of Section 3.4.5. The curves drawn in Figure 3.8 are with the function given in equation 3.33, using the best fit values of the joint fit of A_{11} , A_{10} and A_{00} . Notice that the predictions of equation 3.33 matches the data for $W_k = 0$, indicating our function satisfies $\lim_{Y \rightarrow 0} \mathcal{A}_{11}(X, Y) = \mathcal{A}_{h_x k}(X)$ as expected.

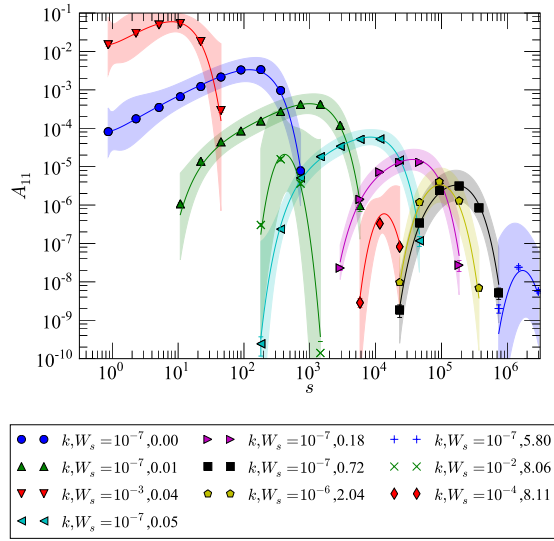


Figure 3.12: Spanning Avalanches Data and Fit Shown here are the area-weighted size distributions for spanning (11) avalanches with different k and window size W . The lines are the joint best fit value using the functional forms using equations 3.24, 3.27, and 3.33, whereas the shaded areas are the fluctuations in theory corresponding to the systematic errors on our exponents and parameters (individual parameter best fit values and errors are quoted in Table 3.2).

Parameter	Best Fit	Standard Errors in Linear Approx.	Systematic Errors	Drift from Best Fit with free ζ
-----------	----------	--------------------------------------	-------------------	--

Universal Exponents

τ	1.2636	± 0.0006	± 0.02	-0.006
ν_k	0.4630	± 0.0002	± 0.01	-0.02
ζ	0.63 (fixed)	± 0.0007	± 0.02	+0.05

$$\mathcal{A}_{00}(s_k, W_k) = \exp(-(T_{00} + U_{00}s_k^{1/2} + Z_{00}s_k^{\delta_{00}} + C_{00}(\frac{s_k}{W_k^{n_{00}}})^{m_{00}}))$$

T_{00}	2.488	± 0.004	± 0.1	-0.01
U_{00}	-0.150	± 0.005	± 0.1	+ 0.04
Z_{00}	0.0040	± 0.0004	± 0.01	-0.0009
δ_{00}	2.21	± 0.03	± 0.9	+0.06
C_{00}	5.60	± 0.01	± 0.7	+1.8
m_{00}	1.371	± 0.003	± 0.1	-0.04
$n_{00}(1 + \zeta)$	1.621	± 0.004	± 0.7	+0.04

$$\mathcal{A}_{10}(s_k, W_k) = \exp(-(T_{10} + U_{10}s_k^{1/2} + Z_{10}s_k^{\delta_{10}} + C_{10}(\frac{s_k}{W_k^{n_{10}}})^{m_{10}}))$$

T_{10}	1.437	± 0.004	± 0.1	-0.1
U_{10}	0.244	± 0.244	± 0.1	-0.03
Z_{10}	0.027	± 0.001	± 0.03	+0.005

Continued on next page

Table 3.2 – continued from previous page

Parameter	Best Fit	Standard Errors in Linear Approx.	Systematic Errors	Drift from Best Fit with free ζ
δ_{10}	1.64	± 0.01	± 0.4	-0.06
C_{10}	1.153	± 0.004	± 0.2	+0.7
m_{10}	1.962	± 0.005	± 0.2	+0.04
$n_{10}(1 + \zeta)$	1.624	± 0.004	± 0.1	+0.06

$$\mathcal{A}_{11}(s_k, W_k) =$$

$$\exp(-(T_{11} + U_{11}s_k^{1/2} + Z_{11}s_k^{\delta_{11}} + D_{11}(\frac{s_k}{W_k})^{m1} + C_{11}(\frac{s_k}{W_k^{n_{11}}})^{-m2})$$

T_{11}	0.47	± 0.03	± 1.2	-0.3
U_{11}	-0.5	± 0.1	± 3.6	-0.5
Z_{11}	0.21	± 0.06	± 1.7	+0.4
δ_{11}	1.102	± 0.03	± 1.0	-0.12
D_{11}	0.52	± 0.03	± 1.0	+0.1
C_{11}	0.83	± 0.05	± 1.6	-0.3
m1	1.48	± 0.01	± 0.4	-0.0008
m2	1.64	± 0.02	± 0.6	-0.02
$n_{11}(1 + \zeta)$	1.655	± 0.004	± 0.1	+0.02

Continued on next page

Table 3.2 – continued from previous page

Parameter	Best Fit	Standard Errors in Linear Approx.	Systematic Errors	Drift from Best Fit with free ζ
Corrections to Scaling $A_1^{zz}/s + A_2^{zz}/s^2$				
A_1^{00}	-0.94	± 0.02	± 0.5	+0.06
A_2^{00}	0.27	± 0.01	± 0.4	-0.04
A_1^{10}	0.15	± 0.01	± 0.4	-0.2
A_2^{10}	-0.07	± 0.01	± 0.3	+0.1
A_1^{11}	0.8	± 0.07	± 2.1	-0.3

Table 3.2: Best Fit Exponents and Parameters for Windowed Distributions. Here are the results of our joint fit for the windowed A_{00} , A_{11} , A_{10} distributions. The corresponding scaling forms which were fit are quoted in the table alongside the parameter results. Here systematic error bars which account for errors in the theory (see Section 3.8.4 for explanation) are given. The traditional standard error bars are typically ~ 30 times smaller than the systematic error bars quoted. The last column is the drift in parameters seen when allowing ζ to be a free parameter. Notice that these numbers are more or less similar or smaller than the estimated systematic error, except for ζ . (The problems in measuring ζ are discussed in Section 3.9) As in Table 3.1, we quote several digits more than the error bars warrant for individual parameters, because the errors are strongly correlated; truncating each parameter to its significant figures would yield a poor fit.

3.6 SCALING SHAPES AND RESULTS

In the previous section we wrote down scaling functions for each type of avalanche inside a window. In principle there are many possible parameterizations we can choose that would be able to capture the behavior of the data. In this section we explain how and why we chose each one, and also discuss the scaling function in the limit of small windows.

3.6.1 SCALING SHAPES AND FUNCTIONAL FORMS

We would like to capture the scaling behavior of both the finite size of the avalanches, and the effect of the window size on the distributions. We choose forms inspired by a functional renormalization group expansion for static avalanche size distributions for all universality classes [69], and further motivated by heuristic arguments for the cutoff dependence on the two scaling variables, $s_k = s/L_k^{1+\zeta}$ and $W_k = W/L_k$.

Similar to in Section 3.4.3, we start with an avalanche size distribution of the form:

$$\mathcal{A}(s_k) = \exp(-(T + U s_k^{1/2} + Z s_k^\delta)) \quad (3.34)$$

We expect that as $W \rightarrow \infty$, we will not see the effect of the window size, and the scaling forms will go to the limit of our proposed avalanche size distribution in Eq. 3.34. Keeping this in mind, we would like to write a function of $\mathcal{A}(s_k, W_k)$, including the effect of the window size. For the 00 and 10 distributions, we expect the avalanche sizes to be cutoff by the window size W when $W/L_k < 1$, hence a cutoff dependent on s_k/W_k^n should be expected, where $n > 0$. While when $W \gg L_k$, their scaling forms should go to the limit of our proposed avalanche size distribution in Eq. 3.34. Therefore for the 00 and 10

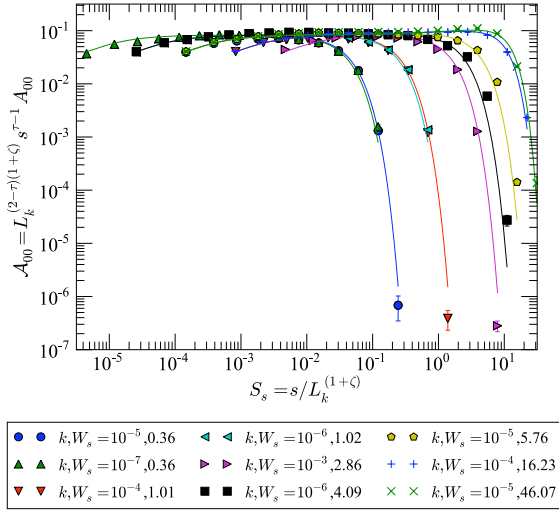
avalanches, we propose a scaling form of:

$$\mathcal{A}_{zz}(s_k, W_k) = \exp\left(-\left(T_{zz} + U_{zz}s_k^{1/2} + Z_{zz}s_k^{\delta_{zz}} + C_{zz}\left(\frac{s_k}{W_k^{n_{zz}}}\right)^{m_{zz}}\right)\right). \quad (3.35)$$

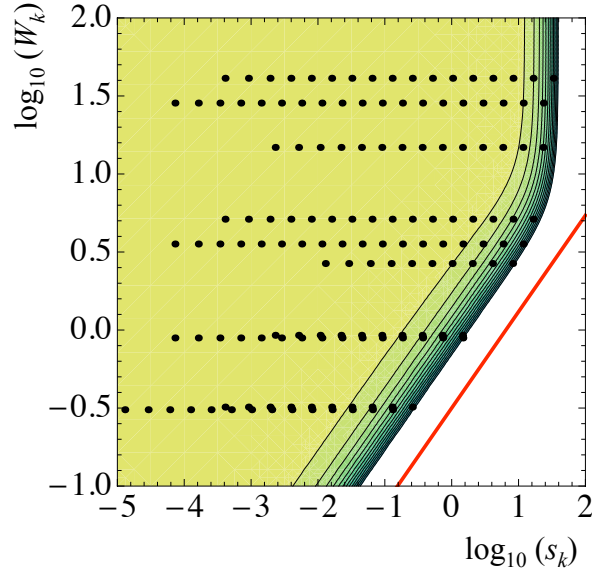
We have heuristic arguments for what this n_{zz} value should take. Figure 3.9, a schematic of an avalanche cut by different windows, is meant to help illuminate our discussion. For the 00 internal avalanches, the largest avalanche contained fully within the window should have a width w that is roughly W . And since $s_{max} \sim w_{max}h_{max} \sim w_{max}^{1+\zeta}$, then $s_{max} \sim W^{1+\zeta}$ and it follows that $s_k \sim W_k^{1+\zeta}$, giving us an expectation value of $n_{00} = 1 + \zeta$. Numerically, we find $n_{00} \sim 1.62$ when we fix $\zeta = 0.63$. The fit plotted against one of the scaling variables s_k and also the contour plot of the scaling shape is shown in Figure 3.13.

For the 10 or 01 split avalanches, since we are effectively measuring the ends of avalanches that spill into the window, n_{10} depends on what the shape of the avalanche is at the edges. The largest portion of an avalanche to spill into the window will again be limited by the size of the window W . Here the shape follows the roughness of the two fronts preceding and following the avalanche, where $h(x) \sim x^\zeta$ for each, so plausibly $h_{edge} = h_{after} - h_{before} \sim W^\zeta$. The size is then limited by $s_{max} \sim w_{max}h_{edge} \sim W^{1+\zeta}$, giving us an expectation value of $n_{10} = 1.63$. Numerically, we find $n_{10} \sim 1.62$ (ζ is estimated from 0.62 – 0.72 in our various measures), matching our expectation. The fit plotted against one of the scaling variables s_k and also the contour plot of the scaling shape is shown in Figure 3.14.

Now we move on to discuss the 11 spanning avalanches. Here the situation is slightly more complicated than the previous two cases, due to the distribution being strongly cut off at two length scales, as one may note from the shapes of the distributions shown in Figure 3.12. First of all the avalanches need to be large enough to cross the window, implying an inner cutoff that depends on $W_k^{1+\zeta}/s_k$ (i.e. the cutoff is for $s_{min}/s \lesssim 1$ and



(a)



(b)

Figure 3.13: Internal Avalanches Scaling Function. (a) Scaling collapse showing $\mathcal{A}_{00}(s_k, W_k)$ as a function of s_k . The separate curves show the effects of the scaled window size W_k . (b) Logarithmic contour plot of best fit scaling function against both scaling variables s_k and W_k . Each contour reflects a drop of a factor of e in the scaling function. The black dots are at locations of the simulated data points used in the fit indicating where the fit should be a reliable prediction. The red solid line is $\log_{10} W_k = n_{00} \log_{10} s_k$ which is the slope at the large avalanche cutoff, with $n_{00} = 1.62$, the best fit value. ($n_{00} = 1 + \zeta = 1.63$ is the expected value from our heuristic arguments).

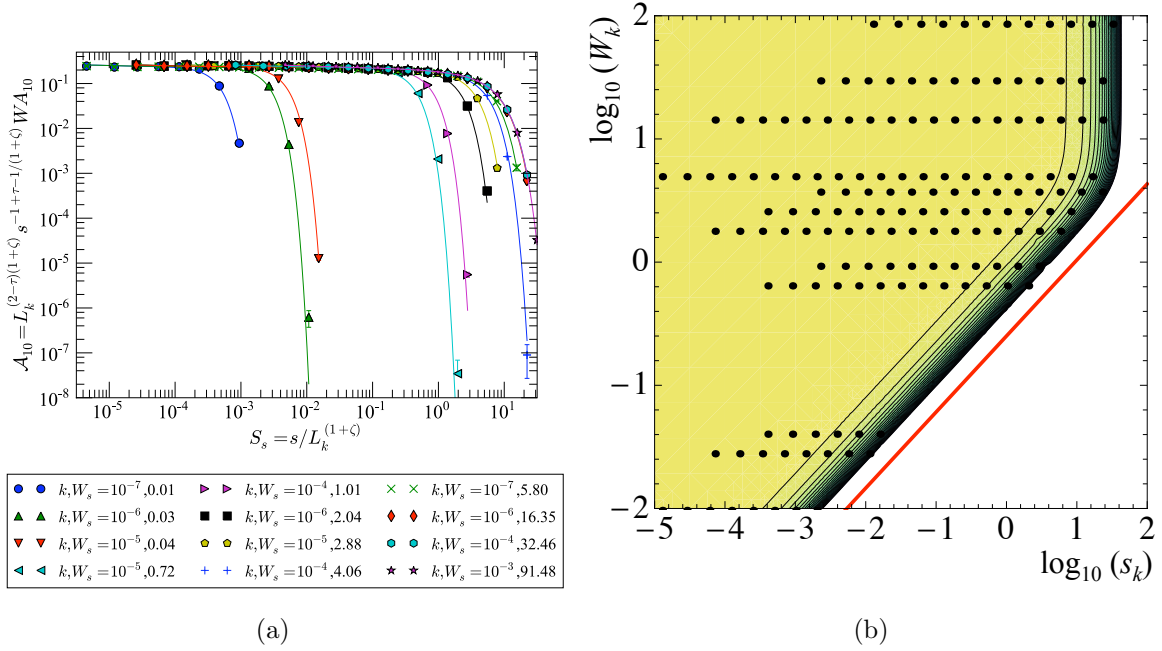


Figure 3.14: Split Avalanches Scaling Function. (a) Scaling collapse showing $\mathcal{A}_{10}(s_k, W_k)$ as a function of s_k . The separation between curves shows the dependence on the scaled window size W_k . (b) Logarithmic contour plot of best fit scaling function against both scaling variables s_k and W_k . Each contour reflects a drop of a factor of e in the value of the scaling function. The black dots are at locations of the simulated data points used in the fit. The red solid line is $\log_{10} W_k = n_{10} \log_{10} s_k$ which is the slope at the large avalanche cutoff, with $n_{10} = 1.62$, the best fit value.

so $s_{min}/s = W_k^{1+\zeta}/s_k$); here the argument for the minimum size 11 avalanches follows from a similar argument for the maximum size 00 avalanches. The smallest avalanche that is able to span the window will have a width $w_{min} = W$, whereas $h_{min} \sim w_{min}^\zeta$, and $s_{min} \sim h_{min}w_{min} \sim W^{1+\zeta}$. However, in this case s_k should be in the denominator of the scaling variable, since for $s_{max} \gg s > s_{min}$ the probability of the having a spanning avalanche grows as s increases. For the outer cutoff we expect that the maximum size is given by the window size W and the typical maximum height, i.e. $s_{max} \approx Wh_{max}$ which implies that $s_k^{max} \approx W_k^{max}(h^{max}/L_k^\zeta)$. This rescaled height (h^{max}/L_k^ζ) is constant. Therefore the cutoff for the large size avalanches should depend on s_k/W_k . Hence, we propose the scaling form below for the 11 spanning avalanches:

$$\mathcal{A}_{11}(s_k, W_k) = \exp \left(- \left(T_{11} + U_{11}s_k^{1/2} + Z_{11}s_k^{\delta_{11}} + C_{11} \left(\frac{s_k}{W_k^{n_{11}}} \right)^{-m_2} + D_{11} \left(\frac{s_k}{W_k} \right)^{m_1} \right) \right) \quad (3.36)$$

where C_{11} controls the strength of the inner cutoff and D_{11} the outer cutoff.

Figure 3.15(a) shows the shape of the scaling function plotted against one scaling variable s_k , and Figure 3.15(b) gives the contour plot of this function against both variables. The best fit value of n_{11} is $n_{11} \sim 1.65$, whereas the expected was $n_{11} = 1 + \zeta = 1.63$.

Finally, one may note that in our system all the n_{zz} turn out to fit to our expected $1 + \zeta$ within the error bars of ζ . One may be tempted to set n_{zz} as $1 + \zeta$ and have fewer fit parameters in one's form; however, we recognize that our geometrical arguments do not hold for front propagation that is super-rough with $\zeta > 1$, or for models that allow overhangs, so we leave n_{zz} as a free parameter to signify this geometrical constraint.

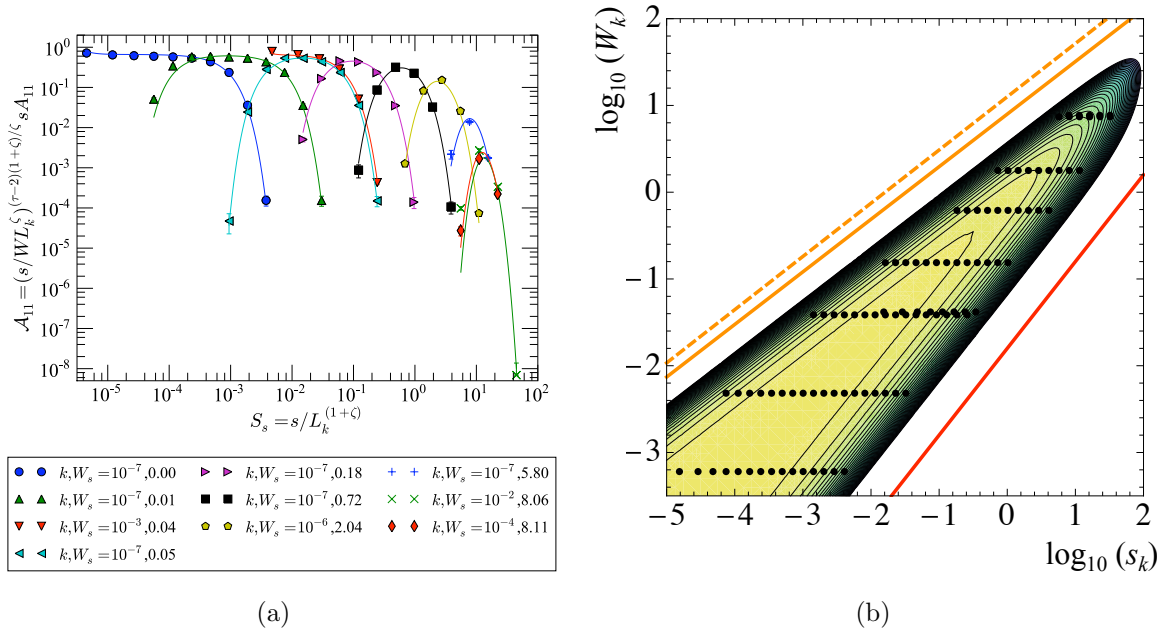


Figure 3.15: Spanning Avalanches Scaling Function. (a) Scaling collapse showing $\mathcal{A}_{10}(s_k, W_k)$ as a function of s_k . The curves move leftward and become more sharply rounded with increasing W_k . (b) Logarithmic contour plot of best fit scaling function. Each contour reflects a drop of a factor of e in the scaling function. The black dots are at locations of the simulated data points used in the fit. The upper orange solid line is the slope of the contour plot at the small avalanche cutoff, and has $\log_{10} W_k = 1/1.65 \log_{10} s_k$ where 1.65 is the best fit n_{11} value. The orange dashed has $\log W_k = 1/1.63 \log_{10} s_k$ where 1.63 is the $1 + \zeta$ value. The lower red solid line is $\log_{10} W_k = \log_{10} s_k$ which is the slope at the large avalanche cutoff.

3.6.2 THE LIMIT OF SMALL WINDOWS

Although there are noticeable imperfections in the theory function, the agreement is impressive between theory and simulation as seen in figures 3.13, 3.14, and 3.15 .

The scaling function for each of the three distributions is a competition between two types of terms: the rescaled size $s_k = S/L_k^{1+\zeta}$ and the rescaled window size $W_k = W/L_k$. Upon examining the fit parameters of the scaling function, all three distributions share the characteristic that at small W_k the terms with pure powers of $s_k^{1/2}$ and $s_k^{\delta_{zz}}$ become unimportant, leaving only $s_k/W_k^{n_{zz}}$ for the 00 and 10 distributions, and for the 11 a s_k/W_k term. Notice that for the 00 and 10 distributions, since n_{zz} is $1 + \zeta$, the L_k dependence disappears for the universal scaling function at small W_k . Therefore, the shape of the scaling function is cut off mainly by the window size W . In fact removing the s_k terms for these functions does not affect the shape for $W_k < 5$. For experiments that study systems in the same universality class as this one, this implies that data may be measured at large magnifications (small windows) and fit to extract exponents and scaling behavior without the extra, often unknown, scale of L_k .

3.7 SUGGESTIONS FOR EXPERIMENTS AND CONCLUSIONS

What does our analysis imply for current experiments? How should one conduct the experiment and analyze the data? Here we discuss for the particular case of magnetic avalanches in Barkhausen noise, how to take into account window effects and further enhance the collection of data.

There are two optical methods for detecting avalanche distributions for Barkhausen noise in 2D thin films, and both make use of the magneto-optical Kerr effect (MOKE).

When a polarized beam of light reflects off a magnetized sample, the reflected polarization is affected depending on the magnetization. A second polarizer can be used to filter this signal, and then using either a photodiode [6], or an optical microscope [7, 47], we can collect data about the avalanches from the signal. For experiments using a photodiode (let us call this “laser reflectometry”), one can only measure the total magnetization change over time, and not individual avalanches. For experiments using an optical microscope (let us call this “avalanche visualization”), one can resolve individual avalanches and their shape.

In laser reflectometry experiments [6] we only have information for the magnitude of magnetization as a function of time, and cannot see which avalanches touch the boundary. Furthermore, in current techniques the laser spots are Gaussian in shape, and do not have sharp boundaries. However, there seems to be no fundamental reason why the illuminated region could not be optically generated with uniform illumination and sharp edges, up to some diffraction limit depending upon the geometry of the experiment. (A typical avalanche of interest is a few microns in size, large compared to the wavelength of optical light which is 400-700 nm). If one could make the edges of the laser spots sharper, one could adjust the laser spots to flicker between two sizes, one with a radius slightly larger than the other. Events that occur with the same magnitude in both the large size measurement and the smaller size measurement would be 00 internal avalanches. More elaborate sequences of spot shapes could be used to further distinguish 01 and 10 split avalanches from 11 spanning avalanches.

For avalanche visualization experiments [7, 47, 61], it is straightforward to separate the data into 00, 10, 01, and 11 avalanches for systems which have our strip geometry and flat fronts with $\zeta < 1$. Our analysis will remain valid with minor corrections due to real-world experimental circumstances. For example, sometimes the propagation direction of the front is not parallel to the top and bottom boundaries. In this case there would be corrections

depending on the angle of the tilt θ and the size of the window. The local heights h_x would need to be adjusted with the factor of $\cos\theta$. The 10, and 01 avalanches would be cut off at an angle, but for self-affine (short, wide) avalanches these size corrections are likely irrelevant.

For materials with dipolar interactions and zig-zag shaped fronts [7, 74], we are less confident that our methods can be applied without modification. The large vertical extent of the zig-zag front suggests that all four boundaries of the window will matter; therefore we will need to divide avalanches into more categories (0000, 1000, 0100, 0010, 1010...). The analysis for these types of avalanches will be more complicated. This would be an interesting problem to pursue by simultaneous analysis of simulations and the experimental data.

Knowing how to deal with window effects can be an important tool for these visualization experiments. By combining data at several magnifications (corresponding to different window sizes), we resolve a larger range of length scales. Higher magnifications will show the small avalanches, while lower magnifications will allow us to both capture larger avalanches and explore more fully the 00 internal avalanches. For example, if our CCD camera recording the images has a resolution of 1000^2 pixels, and we have a magnification of up to 5x-50x, we can simultaneously explore a range of window sizes and extend our effective spatial resolution from 1000^2 to 10000^2 .

More generally, this paper has provided the tools needed to extract from the experimental data for systems of similar interface dynamics the critical exponents τ , ζ and the universal scaling functions \mathcal{A}_{Sk} , \mathcal{A}_{hk} , etc. For these experiments, we can also measure widths and heights and the average shape, giving us an independent measure of ζ , and the universal scaling function $\mathcal{A}_{h_x k}$. Our detailed analysis and comprehensive methods presented in

this paper enable a more powerful interpretation of current experiments, and improved construction of future experiments.

3.8 METHODS AND SOFTWARE

3.8.1 NUMERICAL SIMULATION

The avalanche simulations in this paper were produced using a quenched KPZ model [50, 51], with dynamics given by:

$$\frac{\partial h(x, t)}{\partial t} = F - k\langle h \rangle + \gamma \nabla^2 h + \lambda (\nabla h)^2 + \eta(x, h) \quad (3.37)$$

where $h(x, t)$ is the height of the front, F the driving force, k the “demagnetization field”, linear and non-linear terms for the KPZ model controlled by the parameters γ and λ respectively, and η gaussian random noise. This was run for system sizes of width L 4096, 8192, and 16384. The simulations have been run in a strip geometry (4096×8192 , 8192×16384 , and 16384×32768) and the bottom half of the simulations have been truncated to avoid transient effects due to the initially flat front. The left-right boundaries have periodic boundary conditions.

The simulations are done using a discrete cellular automaton model, in which the displacement of the string h , the time t and the space x are all discretized and take integer values [17, 53]. For a configuration $\{h_i\}$, we compute the local force F_i at each site i , leading to a discretized version of Eq. 3.37

$$F_i = F - k\langle h_i \rangle + \frac{\gamma}{a^2} \sum_{nn} (h_{i+nn} - h_i) + \frac{\lambda}{a^2} \sum_i (h_{i+i} - h_{i-1})^2 + \eta_i(h_i), \quad (3.38)$$

where the sum runs over all the nearest neighbors nn for the site i , a is the discretization length that we set to 1, and $\eta_i(h_i)$ is a random force. The automaton dynamics are as

follows: (1) increment the external field until one site is unstable ($F_i > 0$); (2) determine for each site along the interface whether it is stable ($F_i < 0$) or unstable ($F_i > 0$); (3) advance all unstable sites by one step $h_i = h_i + a = h_i + 1$ in parallel, generating a new value of the pinning force $\eta_i(h_i)$; (4) repeat until no sites are unstable (the end of the avalanche); (5) repeat (1-4) until the front passes the top of the simulated window.

3.8.2 NONLINEAR LEAST SQUARES FITTING

We use nonlinear least squares methods for fitting data to theory functions, minimizing a cost defined as:

$$C(\theta) = \frac{1}{2} \sum_i \left(\frac{y_i^{theory} - y_i^{data}(\theta)}{\sigma_i} \right)^2 \quad (3.39)$$

Here θ are the parameters, y the function value, and σ_i the error on the data points. The weight σ in our case is determined by fluctuations from run to run. Namely, we bin the data (in equispaced log bins) for each of N simulations, calculate the standard deviation of this value across runs, divide by $\sqrt{N-1}$ to get the fluctuation in the mean of that bin.³

In our distributions, small avalanches occur more often (leading to small error bars), but large avalanches are more important, and the smallest avalanches suffer from non-universal lattice effects. So during the fitting process there is a tradeoff between fitting the region where there is good data and where the variations are most important. We use a number of methods to compensate for this imbalance. (1) We set a minimum error bar (1% of the data value) on the data points, making the error bars on smaller avalanches larger, and therefore decreasing their weight.⁴ (2) Analytic and singular corrections to scaling can

³This definition of fluctuations in the (simulation) data assumes that the error in each bin is uncorrelated.

⁴We choose this 1% empirically. We adjust error bars to be large enough so that the theory is not distorted over the data points with small error bars, but not so large that the points don't matter. Therefore this value depends on the size of the error bars overall in the data set.

also account for non-universal effects. We include analytic corrections to scaling for the lattice effects in our scaling functions. These corrections appear in all distributions we discuss. A more detailed discussion is in Section 3.8.5. (3) One may also skip points that have non-universal behavior when fitting. For our fits in this paper, all points are included.

Another issue arises in regions where one has sparse data; there may be bins that do not have any observations. For these zeros, the error bar should not be zero! We can use maximum likelihood methods to estimate theoretical errors. Say we have N experiments, and bin the data with L_i sizes in each bin i . With the median size in the bin S_i , the expected probability for each size is $\rho_i = A(S_i)/S_i$, where $A(S)$ is the theoretical distribution of sizes, and so getting a zero in one of the bins will have the probability $p = (1 - \rho_i)^{NL_i}$. Using maximum likelihood, this results in a cost of $C = -\log p = -NL_i \log(1 - \rho_i) \sim NL_i \rho$ given that ρ is small. The residual we add to the total cost is therefore:

$$r_{zero} = \sqrt{NL_i \rho_i(\theta)}. \quad (3.40)$$

This calculation is generalizable to sparse data that is non-zero- say one has n events in a bin for N measurements, then the probability is $p = \frac{(NL_i)!}{n!(NL_i-n)!} (1 - \rho_i)^{NL_i-n} \rho_i^n$, and the appropriate error bar we get is approximately $\sigma = \frac{1}{NL_i}$. One could then use the larger of the error bar given by this argument or the statistical error bars from the simulation. In practice, for our simulations, we find it sufficient to use the statistical error bars but to compensate with minimum error bars given by Eq. 3.40.

In non-linear least squares fitting, we can also include priors in the cost if we have assumptions or information a priori about the parameters. For example, in our problem, we put priors on the exponents inside the scaling functions (n_{00} , δ_{00} , etc) to prevent them from going to large values and forcing their corresponding coefficients to zero. As a result our

cost function now becomes:

$$C(\theta) = \frac{1}{2} \sum_i \left(\frac{y_i^{theory} - y_i^{data}(\theta)}{\sigma_i} \right)^2 + \sum n^2 + \log(\delta_{11}^2) \quad (3.41)$$

In Eq. 3.41, n represents all the arbitrary exponents that occur inside the scaling functions (n_{zz} , m_{zz} , δ_{zz} etc...). $\log(\delta_{11}^2)$ is included to prevent δ_{11} from going to zero.

A clear understanding of these techniques for fitting is important for increasing the reliability of our results, and acknowledging its limitations. In a following subsection, Section 3.8.4, we will further discuss how to estimate the reliability of results inferred by fitting data to a theory, generating systematic error bars for fitting results.

3.8.3 SOFTWARE FOR FITTING

To facilitate the exploration of this problem, we have developed a software environment, *SloppyScaling*, in Python. This code is downloadable at <http://www.lasp.cornell.edu/sethna/Sloppy/SloppyScaling/SloppyScaling.htm>. The main features of this code include various nonlinear-least squares fitting methods [75], automatic plotting for visualization, and methods for generating systematic error bars on the theory.

3.8.4 SYSTEMATIC ERROR BARS

We have quoted in our results systematic error bars instead of the more commonly used standard error bars in the parameters. Standard errors given by the covariance matrix are expected to be erroneous for our problem, since our problem is highly nonlinear in the parameters, and also sloppy- parameter combinations in the sloppiest directions can vary an infinite amount without affecting the fit. We use a method due to Frederiksen et. al [73] for Bayesian estimation of errors. This method involves assuming that given a theory (M)

which is imperfect, a spread of parameters (each corresponding to different models) may fit the data(D) in an equally acceptable matter. We can define a probability of a certain model with

$$P(\theta|D, M) = \exp(-C(\theta)/T) \quad (3.42)$$

where $C(\theta)$ is the cost at a given set of parameters θ , and the effective temperature T sets a scale for the fluctuations away from the best fit. Since the cost at the best fit parameters C_{bf} is a measure of how well the theory is doing, we choose $T = 2C_{bf}/N$, where N is the number of parameters with "equipartition" allowing each degree of freedom a contribution of $\frac{1}{2}T$ to the total cost.

Ideally, after defining such a probability, one should sample parameter space to determine the systematic error bars on parameters. However, in our functions sampling is non-trivial due to parameter evaporation [76], the "entropy" for parameters drifting to infinity overwhelms their cost in degrading the resulting fits. Therefore, we make a quadratic estimate of the fluctuations in predictions, essentially using propagation of error to estimate the systematic error. The covariance matrix gives an error σ_{stat} that assumes the temperature of 1, corresponding to $P(\theta|D, M) = \exp(-C(\theta))$. Using propagation of error, we calculate the systematic error according to our effective temperature $T = 2C_{bf}/N$:

$$\sigma_{sys} = \sqrt{T}\sigma_{cov} \quad (3.43)$$

The shaded plots are generated by sampling according to the Hessian at the best fit, weighting our steps in each eigendirection by the inverse square root of the eigenvalue, and scaling the steps with a low temperature (T_L). Then for our ensemble of parameters we calculate the fluctuations in the theory (residuals δr_{ens}) corresponding to the ensemble. We scale up these fluctuations according to the temperature defined by the best fit, or

$$\delta r_T = \sqrt{\frac{T_{bf}}{T_L}} \delta r_{ens},$$

$$\delta r_T = \Sigma \frac{\partial r}{\partial \theta} \delta \theta_T \tag{3.44}$$

We have also estimated systematic errors by removing large k curves (which we believe have larger corrections), and looking at the corresponding drift in exponents and parameters. The estimate of the systematic error that this procedure gives is often similar (sometimes smaller) to the one using our temperature-scaled propagation of error.

3.8.5 CORRECTIONS TO SCALING

Corrections to scaling play an important role in our scaling functions, their inclusion accounts for non-universal effects, and helps increase the reliability of universal predictions. In each of the scaling functions in this paper we have included analytic corrections to scaling that capture the lattice effects of our automata simulations. They are of the form:

$$\exp(A^1/S + A^2/S^2) \tag{3.45}$$

This expansion for small S corrects for the lattice effects on small size avalanches which we believe to be present in the distributions. One can imagine that experiments may have other origins of non-universal effects, such as a nonlinear signal amplifier or distorting lens; one should always attempt to account for and include these [67].

One caveat is that, just as adding extra free parameters does not necessarily increase the quality of one's fits, adding corrections is not a guarantee for increasing the accuracy of one's scaling function. One should be careful in checking that the terms included in the corrections to scaling behave as expected in the region of interest, are subdominant when taking the appropriate limits, and do not confuse the main universal scaling function, either by canceling out terms or having the same effect. An example of this complication is seen

in our studies of using the limit of the 11 distribution at $W = 0$ for the local height distributions.

In sections 3.4.4 and 3.5.3, we take the view point of using the parameterized form of $A_{11}(s|L_k, W = 0)$ as the proper limit of $A(h_x|L_k)$. However, this data should be matched as well by $A_{11}(s|L_k, W = 1)$, since in effect this is what we are fitting for the local height distributions. We can view the ratio between the two functions as a multiplicative correction to scaling from lattice effects (without considering the corrections to scaling for lattice effects in equation 3.45):

$$\begin{aligned}
f(h_x, L_k) &= \frac{A_{11}(s|L_k, W = 1)}{A_{11}(s|L_k, W = 0)} & (3.46) \\
&= \exp\left(-\left(U_{11}\left(\frac{h_x}{L_k^{1+\zeta}}\right)^{1/2} + Z_{11}\left(\frac{h_x}{L_k^{1+\zeta}}\right)^{\delta_{11}} + C_{11}\left(\frac{h_x}{L_k^{1+\zeta-n_{11}}}\right)^{-m_2}\right)\right) \\
&= \exp\left(-\left(U_{11}L_k^{-1/2}h_s^{1/2} + Z_{11}L_k^{-\delta_{11}}h_s^{\delta_{11}} + C_{11}L_k^{(1+\zeta-n_{11})m_2}h_x^{-m_2}\right)\right)
\end{aligned}$$

Here we define $h_s = h_x/L_k^\zeta$. Note however that for the term $C_{11}L_k^{(1+\zeta-n_{11})m_2}h_x^{-m_2}$, the value of the fit for n_{11} equals 1.65, which is within the range of error for $1 + \zeta = 1.63 \pm 0.02$. Therefore this term is nearly $C_{11}h_x^{-m_2}$, where $m_2 = 1.61 \pm 0.6$. This term then has the same effect as the correction to scaling term A_2^{11}/s^2 at small W (since $s \sim hW$ for 11 avalanches at small W). Since A_2^{11}/s^2 is only significant in the range of small s , which only occur in the 11 distributions at small W , these two parameters serve the same purpose, and it is redundant to include both for the fits. We therefore remove the term A_2^{11}/s^2 for the 11 distributions for our fits.

One can also check the corrections and see all powers of L_k are negative, and the multiplicative correction approaches unity as we get closer to the critical point. With our current fit, the term with $L_k^{-1/2}$ dominates the corrections. Notice that, originally, to account for lattice effects, we have added corrections in integer powers of h_x ($\exp(A_1^{11}/h_x + A_2^{11}/h_x^2)$),

which are subdominant compared to $L_k^{-1/2}$. This implies that there are more dangerous corrections to scaling than originally inferred. By this method, one might check if the corrections originally included are sufficient- in this case they are close, but could be improved upon by systematically adding similar terms.

In a continuum case, the concept of local heights h_x should describe a smooth shape tracing the depinning line, in our automata, since the smallest width is naturally 1 lattice spacing, the smallest possible window width is $W = 1$. In measuring the local heights, this discreteness limits the smoothness of the shape of h_x , and gives rise to the corrections we see. Here we've seen that if we "know" from other measurements (in our case the 11 spanning avalanches) the right limit the universal scaling form should take, we may find the form of the corrections.

3.8.6 SCALING COLLAPSES AND THEIR LIMITATIONS

We have argued at various points in the paper that scaling collapses are limited and may lead to questionable results. Here we will illustrate an example of this. Using the critical exponents given by a free fit of the windowed distributions (ζ allowed to vary), we collapse the sizes, heights and widths. Comparing the figures included here and the ones in Section 3.4 (Figures 3.5, 3.6, and 3.7.), one can see that the collapses are of similar quality.

The fact that such distinct values of ζ can yield similar quality collapses may imply (1) our "systematic error" bars on ζ , estimated to be ± 0.02 , are in reality much larger, (2) collapses do not incorporate non-universal corrections to scaling, and these may have an important effect, (3) collapses are not a reliable way of verifying the values of critical exponents. In particular, we expect corrections to scaling due to large k to be responsible for the drift in exponents.

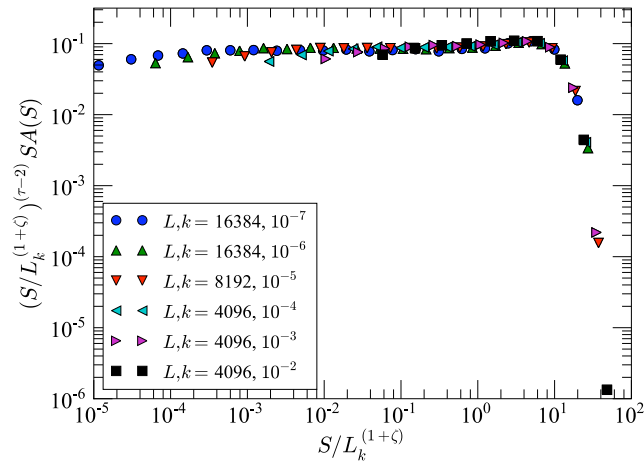


Figure 3.16: Size distribution collapse Here we collapse the size distributions with exponents $\tau = 1.25$, $\nu_k = 0.44$, and $\zeta = 0.68$. Notice that the collapses are similar to the ones shown in Figure 3.5. Here only the combination of $\nu_k(1 + \zeta)$ affect the scaling collapse, the large shifts in ν_k and ζ mostly cancel in the product, yielding similar collapses.

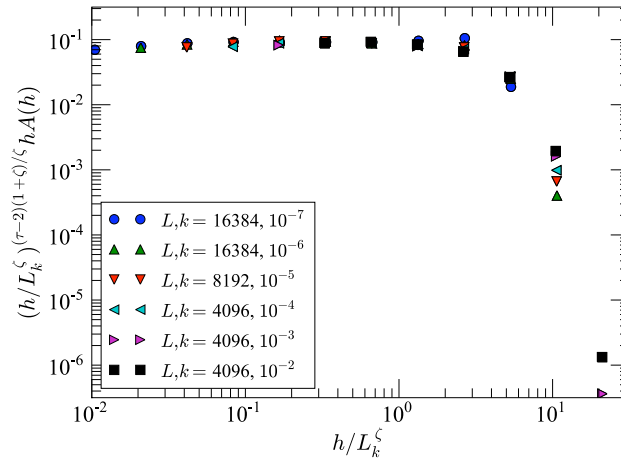


Figure 3.17: Height distribution collapse Here we collapse the size distributions with exponents $\tau = 1.25$, $\nu_k = 0.44$, and $\zeta = 0.68$. Here only the combination of $\nu_k \zeta$ affect the scaling collapse, the large shifts in ν_k and ζ mostly cancel in the product, yielding similar collapses. Comparing this with the collapse shown in Figure 3.6, we see that the two collapses are comparable in quality, where in Figure 3.6 the large avalanche cutoff is collapsed nicely, and here the smaller avalanches are collapsed better.

With these software tools and analytical methods, data at critical points may be analyzed while including multiple scaling variables, allowing for the treatment of a broad range of experiments, and also allowing for a far more rigorous estimation of statistical and systematic errors. By using automatic fits to entire scaling functions, instead of traditional collapses, and by estimating systematic error bars, we facilitate the interpretation of data with multiple scaling variables and analytic corrections to scaling. This advance will allow for better characterization not only of noise in magnetic thin films and similar avalanche dynamics, but should be broadly applicable to all applications of critical phenomena and scaling theories to experiments and simulations.

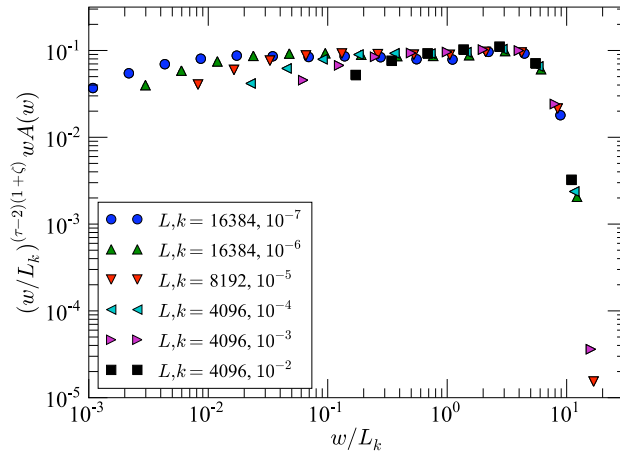


Figure 3.18: Width distribution collapse Here we collapse the size distributions with exponents $\tau = 1.25$, $\nu_k = 0.44$, and $\zeta = 0.68$. Notice that the collapses are similar to the ones shown in Figure 3.7. Here only the combination of ν_k affects the scaling collapse and $(\tau - 2)(1 + \zeta)$ affects the shape of the scaling collapse. Since ν_k does not change significantly, the quality of the collapses are similar.

3.9 THE ROUGHNESS EXPONENT ζ

In the investigations presented in this chapter, we have found that the estimates of the critical exponent ζ have been problematic. In this section, we will discuss various means of measuring this exponent, the significance of the range of values we find from various measurement methods, possible origins of this range, and implications for future research. We emphasize that any value of ζ in the range we observe (0.62 ± 0.02 to 0.72 ± 0.02) can describe all of our data essentially equivalently well.

The shape of the front has been studied as an identifying feature for front propagation models, which is usually characterized by defining a roughness exponent ζ , which is measured through a height-height correlation function:

$$C(r) = \langle (h(x+r) - h(x))^2 \rangle \sim r^{2\zeta} \quad (3.47)$$

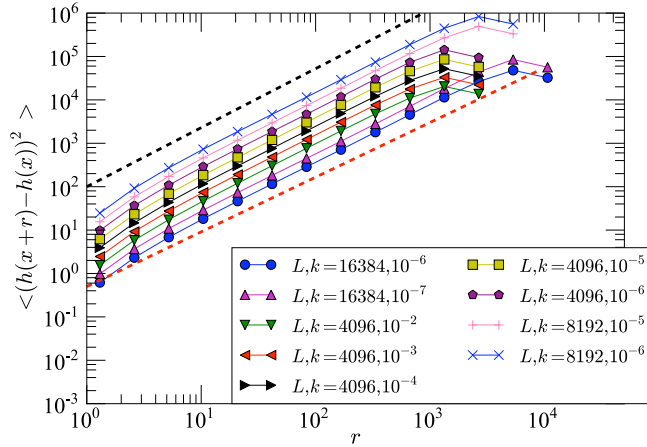


Figure 3.19: Height-height Correlations for the qKPZ Simulations Shown here are the roughness exponents for various simulation sizes L and k . We measure the height-height correlation function $C(r) \sim \langle (h(x+r) - h(r))^2 \rangle$. A power law fit shows ζ falls between 0.63 and 0.68. The lower red-dashed line shows $\zeta = 0.63$ and upper black-dashed line $\zeta = 0.68$. The lines were shifted to show each individual power law.

The quenched KPZ model we use is conjectured to belong to the Directed Percolation Depinning (DPD) universality class [14], which is conjectured in turn to belong to the Directed Percolation (DP) universality class. For a pinned interface in DPD, the roughness exponent $\zeta = 0.63 \pm 0.01$ [50, 51] matches that of the ratio of correlation length exponents in DP $\nu_{\perp}/\nu_{\parallel} = 0.6326 \pm 0.0002$ [77]. (Here $\xi_{\perp} \sim |p - p_c|^{\nu_{\perp}}$ and $\xi_{\parallel} \sim |p - p_c|^{\nu_{\parallel}}$, where p is the branching probability, and p_c is the percolation threshold.). One may note that for a moving interface, the picture is less well known; there has been numerical study that shows $\zeta = 0.70$ [52, 78], but also arguments that the interface under this condition is not self-affine [53], that the moving regions have $\zeta = 1$ and the pinned regions have $\zeta = 0.63$. One could imagine that our demagnetizing force, like the velocity in DPD, could lead to a heterogeneous mixture of different scaling regions, converging to $\zeta = 0.63$ as $k = 0$.

Figure 3.19 shows measurements of the height-height correlations in our model. Using

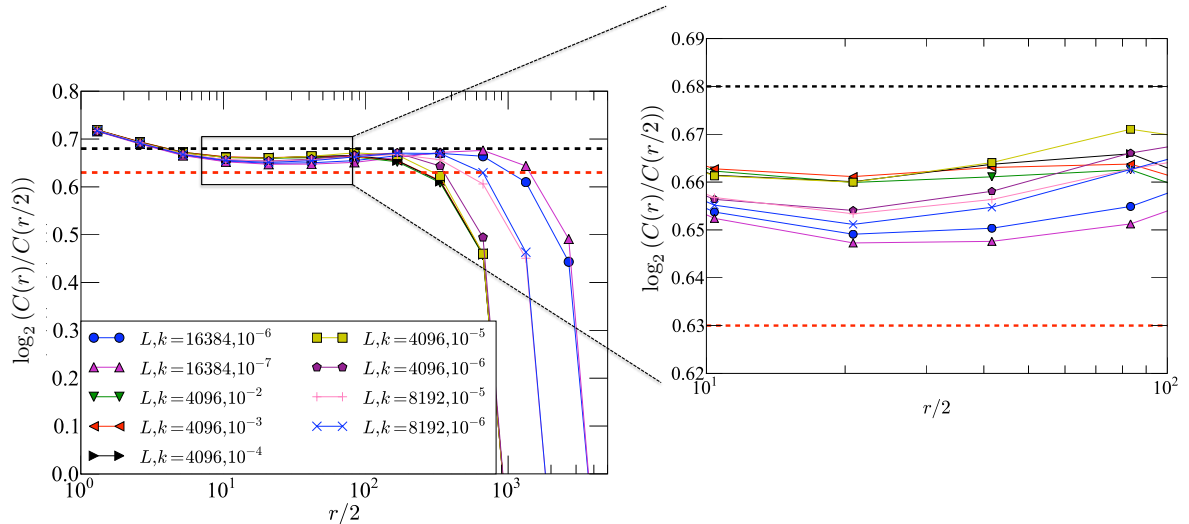


Figure 3.20: Roughness Exponents for the qKPZ Simulations Shown here are the measurements of the local-log slope $\ln[C(r)/C(r/2)]/\ln(2)$ of the height-height correlation function; this is a measure for the roughness exponents for various simulation sizes L and k . The results of the local-log slope $\ln[C(r)/C(r/2)]/\ln(2)$ is consistent with what is seen in Figure 3.19. The lower red-dashed line shows $\zeta = 0.63$, corresponding to directed-percolation depinning (DPD) and suggested by literature to be the correct value for our model. Whereas the upper black-dashed line shows $\zeta = 0.68$ which is the result of our fits of windowed avalanche distributions. In the blowup of the region of $r/2 = 10 - 100$, we can see there is a trend of larger ζ corresponding to larger k simulations.

finite-size scaling for a numerical fit, we see that as k is tuned away from zero, ζ falls between 0.64 and 0.68, increasing with k . Measuring the local log-slope, one can see clearly a drift in the measured exponent in Figure 3.20.

The range of our estimates (varying from $\zeta = 0.63 \pm 0.02$ to $\zeta = 0.72 \pm 0.02$) is large compared to our error estimates; however, best fits with ζ fixed within this range had costs within 1.5 times that of the best fit value, indicating both that our quadratic estimates for the systematic errors are too small and that it may be challenging to definitively measure ζ in either simulation or experiment.

In our fits we find that $\zeta = 0.62 \pm 0.02$ for the size, width and height distributions joint fit, and $\zeta = 0.68 \pm 0.02$ for the 00, 10, 11 joint distributions. Notice that although the direction of front propagation is in general along the y -axis in our problem, portions of the front will be at various angles to the y -axis. Since the local direction of the front propagation is not fixed, we can also choose a rotationally invariant definition of height and width: defining the height and width of an avalanche along the axes of the moment of inertia tensor. We define root-mean-square heights and widths as the square root of its eigenvalues. So if we fit *rms* heights and widths jointly, we get $\zeta = 0.72 \pm 0.02$ much higher than 0.62 measured along the global axes. The difference in these two exponents seems to indicate that the local avalanche shape has a different geometry than the global avalanche front. Many front propagation models spontaneously break rotational symmetry through the orientation of the front. (Envision a circular front growing from a point, with differing front orientations.) Note, however, that the qKPZ dynamics is anisotropic, breaking rotational invariance.

We have also looked at fits with the windows scaling functions involving subsets of simulations with different k . Using smaller values of k generally lead to fits of ζ closer to

0.63. This may point to imperfections in our theory function (are we missing some of the scaling behavior dealing with k ?), or corrections to scaling (analytic or singular). One possibility is that there is a residual crossover effect having to do with another relevant variable. In the anisotropic form of the qKPZ model, the nonlinear term (Eq. 3.4) λ is a relevant variable, and is non-zero under renormalization [13, 14, 79], and although we simulate the model at fixed λ , we have observed there is a crossover effect following a direction having to do with both k and λ . We note that without the nonlinear KPZ term the qKPZ model becomes the quenched Edwards-Wilkinson (qEW) model, and that for the qEW $\zeta > 1$. Literature suggests there also may be a crossover effect due to a runaway fixed point [79]. We think these last two possibilities can be explored with more simulations done on different λ and k , examining a crossover to the linear version of the qKPZ model (the quenched Edwards-Wilkinson), to make a more complete picture of the phase space.

CHAPTER 4

A SCALING FUNCTION DESCRIPTION OF A CROSSOVER BETWEEN TWO MODELS OF DEPINNING ¹

In experimental systems where scaling is observed, it is common to have more than one fixed point influencing the behavior, and it is usually tricky to tune the system such that there are no crossover effects. As we will demonstrate in this chapter, an accurate description of the observed behavior may be provided by functional forms that account for shifts in the scaling laws as a function of the crossover parameter. We use our methods to examine a crossover between the qEW (quenched Edwards-Wilkinson model) and qKPZ (quenched Kardar-Parisi-Zhang) model, which are examples of disordered interface sitting at the depinning transition.

4.1 INTERFACES IN RANDOM MEDIA

Models that describe a fluctuating interface are a simple way to describe physical systems that exhibit wiggles in their morphology. There has been evidence that with a suitable choice of terms these simplistic models may mimic many interesting phenomena, including fluid imbibition, crack front roughening, dislocation hardening, superconducting flux lines, the equilibrium motion of piles of rice down an incline, and domain wall motion in

¹This chapter represents preliminary, unpublished work done in collaboration with Stefano Zapperi and James P. Sethna.

magnets [13, 14]. Indeed, in Chapter 3, we've used a model in this class to generate avalanches for the study of avalanche scaling through observation windows. These simple models have been studied in many contexts, through analytic studies, simulations and comparing observations from experiments. In this chapter, we will examine ways to study a crossover between two of these models, the quenched Edwards-Wilkinson model (qEW) and the quenched Kardar-Parisi-Zhang (qKPZ) model.

The equations of an interface in a disordered environment may be written generally as follows. Let the 1-dimensional interface, $h(x, t)$ be driven by a force $H(t)$ through a disordered environment with a local quenched random force $\eta(h(x), x)$:

$$\frac{\partial u}{\partial t} = F[h](x) + \eta(h(x), x) - D[h](x) + H(t). \quad (4.1)$$

$F[h](x)$ is a general interaction kernel, which controls the interface morphology, and is dependent on $h(x)$ and x . Here $F[h](x)$ could represent short-range surface tension in the interface ($\nabla^2 h$), or long-range interfacial self-interaction fields such as dipole fields in magnets or elastic strains in delamination fracture (as a suitable convolution). $H(t)$ is a time-dependent external driving force. Equations of this form have been extensively studied using continuum simulations [80–83], automata [17, 18, 80, 84–86], and field-theoretic ϵ -expansions [16, 80, 87–91]

Notice that if we set $\frac{\partial h}{\partial t} = 0$, we arrive at a steady-state force equilibrium, where $H(t) = H_0 = -\eta(h(x), x) - F[h](x)$. The interface $h(x, t)$ sits at a local minima in the energy landscape at this point. First, let's consider the case $D[h](x) = 0$, if we increase $H(t) = H_0 + \epsilon$, the force balance is disturbed, and the front only stops if at some point $\eta(h(x), x)$ is large enough to counter this force. Therefore, in any finite random system, there exists some $H_{depinning}$, such that the interface moves without stopping when $H(t) > H_{depinning}$, but when $H(t) < H_{depinning}$, the interface is stuck in a minima.

In simulations, $D[h]$ represents a restoring force that ‘self-organizes’ the depinning transition to the fixed point. This $D[h]$ allows simulations to access many metastable states, without having to enforce an actual quasi-static field. In simulations describing magnets, this term is the demagnetization force [92] $D[h] \equiv -k\langle h \rangle_x$ which approximates the effects of the long-range dipolar field cost of a net advance in the front. We employ the same type of force in studying the qEW and qKPZ models.

How well do simple mathematical caricatures capture the behavior of systems with complicated microscopic interactions, such as magnetic domain wall motion or superconducting flux lines? To answer this question, one tries to compare predictions from calculations and simulations, such as exponents and scaling functions, against experimental measurements. One characterization of this class of models is a geometrical exponent, the roughness exponent ζ , that describes the interface morphology, which is the exponent that corresponds to the coarse graining operation of the heights. Namely, when we change all length scales by a factor b , or $x \rightarrow bx$, then $h \rightarrow b^\zeta h$, or,

$$h(x) \sim b^{-\zeta} h(bx). \quad (4.2)$$

For many experiments and simulations, it is convenient to measure ζ by computing the the height-height correlation of the interface².

$$\langle h(x)h(x+r) \rangle \sim r^{2\zeta} \quad (4.3)$$

ζ should be uniquely determined by which universality class the system belongs to. However, in practice, the observed ζ varies (See table 4.1) even for the same type of system, such as paper wetting. In the previous chapter, we saw a drift in the roughness exponent from tuning the nonlinear term in our qKPZ model. We argue that measuring a single exponent for these systems may prove inadequate, that real-world systems may be

²As we shall see in the next section, this measurement is only valid for $\zeta < 1$.

exhibiting crossover behavior. The variation in these exponents may be due to a subtle crossover between universality classes, and in the next section, we will present a way of measuring if this is true, and quantifying the crossover with a crossover exponent.

experiment	ζ	Reference
Fluid flow	0.73	[93]
	0.81	[94]
	0.65-0.91	[95]
Paper wetting	0.63	[51]
	0.62-0.78	[96]
Bacteria growth	0.78	[97]
Burning fronts	0.71	[98]

Table 4.1: Roughness Exponents in Experiments. Table reproduced from [14]. Notice that there is a wide range of ζ reported, even for the same experimental system.

Crossovers have been studied for similar systems [51], however theoretical studies have proven challenging in different ways [79]. For thin film magnets, the experiments [7, 61, 99] observe a crossover between short-range and mean-field universality classes as long-range dipolar fields are introduced, which can be done by changing the thickness of the film. However, for models of that type, simulations are challenging, both because of the long-range fields and because of the striking zig-zag morphologies that emerge and compete with the avalanche behavior. In the next section, we will analyze a numerically more tractable, but analytically challenging crossover [79]: the transition between the linear, super-rough, quenched Edwards-Wilkinson model (qEW) and the nonlinear quenched KPZ model (qKPZ) [13, 51]. We focus on the crossover behavior of the height-height correlation function.

4.2 PRELIMINARY RESULTS

The isotropic qEW and anisotropic qKPZ have the general structure of Equation 4.1, where for qEW, $F[h] = \gamma \nabla^2 u$ and for qKPZ $F[h] = \gamma \nabla^2 h + \lambda (\nabla h)^2$. Using the automaton simulation employed in 3, we tune λ/γ from 0 to 5, and observe how the behavior changes. Figure 4.1 shows how the front morphology qualitatively changes while we increase the nonlinear parameter λ . Notice that with increasing λ the fronts between events are flatter than at small λ .

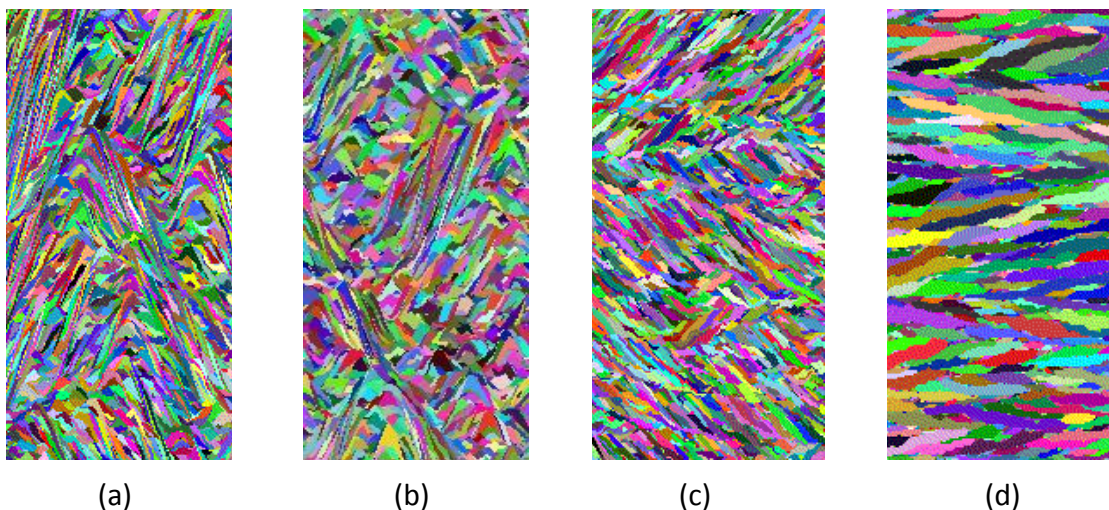


Figure 4.1: Crossover of qKPZ to qEW Model. Fronts generated from simulations with the nonlinear KPZ term coefficients set to (a) $\lambda = 0$, (b) $\lambda = 0.001$, (c) $\lambda = 0.1$, (d) $\lambda = 5$. The random colors represent the area between each pinned front. One can see that the morphology of the interfaces change dramatically as λ increases.

According to Equation 4.3, naively one would assume we could recover the exponent ζ by measuring the local-log slope of the height-height correlation functions (Figure 4.2) for both the qEW and qKPZ fixed points. From other numerical studies, for qEW, we expect $\zeta_{EW} = 1.19 - 1.25$ (Cellular automata [17, 100] models show $\zeta_{EW} = 1.25 \pm 0.01$; continuous string models [101] found $\zeta_{EW} = 1.19 \pm 0.01$). For qKPZ, we expect $\zeta_{KPZ} = 0.63$ [18].

However, there are two things about Figure 4.2 worth noting: (1) the slope-measure of ζ drifts between 0.63 and 1.0 as we change λ , (2) the measured value is never greater than 1 as is naively expected for the linear qEW model.

The second issue has an easy resolution: for $\zeta > 1$, when the interface is ‘superrough’, the height cannot grow faster than linearly with distance, so the height-height correlation function cannot directly exhibit a power law larger than 1 [102]. Instead, we need to consider the finite-size scaling form,

$$C_{EW}(r|L) \sim L^{2\zeta_{EW}}(r/L)^2 \mathcal{C}_{EW}(r/L). \quad (4.4)$$

and measure the roughness exponent ζ_{EW} as a function of the system size.

The drift in the exponent ζ , however, proves to be more complicated to explain. The role of λ in generating this crossover from qEW to qKPZ has only been studied qualitatively [18, 81, 84, 86], with no full description of the crossover scaling [19]. We can use a crossover function that describes the drift between the two limits. For qKPZ (Fig. 4.1c), the correlation function in a system size L takes the finite-size scaling form

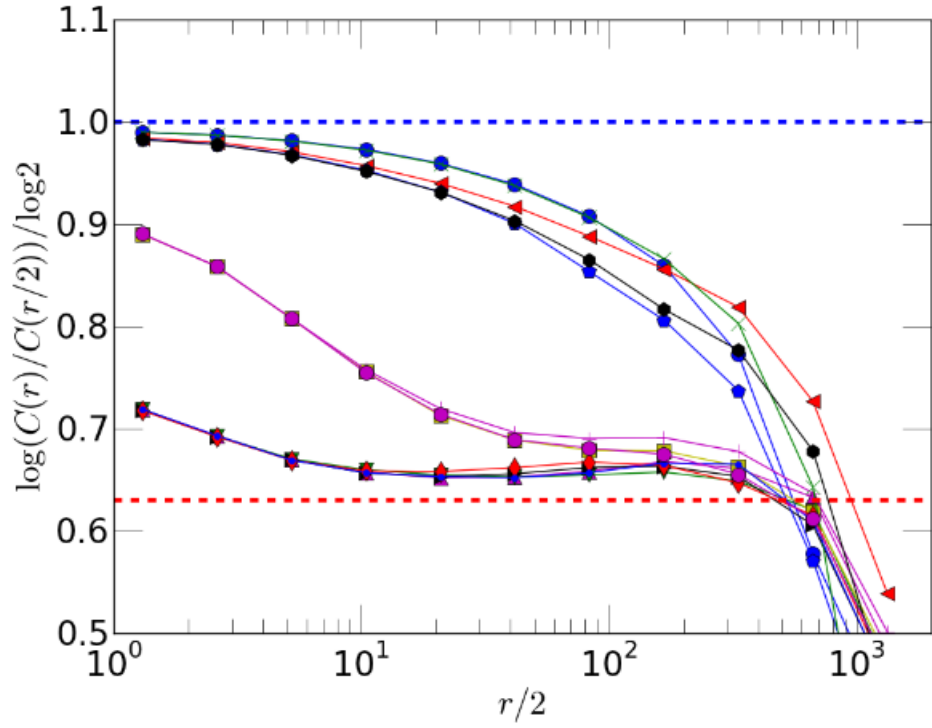
$$C_{KPZ}(r|L) = A r^{2\zeta_{KPZ}} \mathcal{C}_{KPZ}(r/L). \quad (4.5)$$

The crossover describes the RG flow from the qEW fixed point to the qKPZ as the relevant parameter λ is added. The scaling form for the height-height correlation function is thus that of a relevant variable λ added to the qEW scaling:

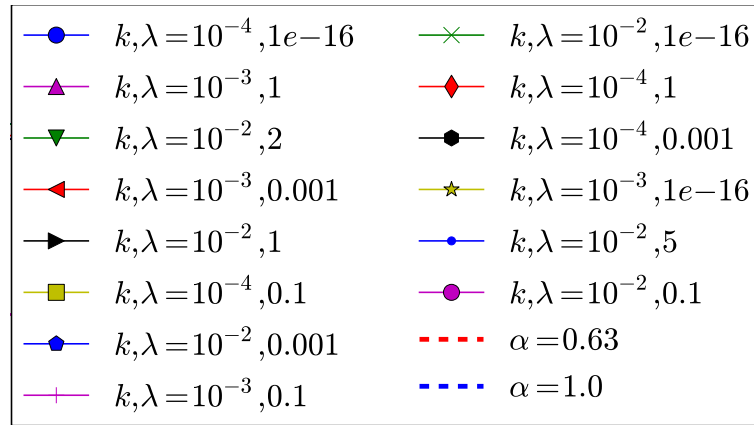
$$C(r|L, \lambda) = L^{2\zeta_{EW}} \mathcal{C}(r/L, \lambda^\phi r) \quad (4.6)$$

. For $\lambda \gg 0$, $C(r|L, \lambda) \rightarrow C_{KPZ}(r|L)$, therefore,

$$\begin{aligned} \mathcal{C}(r/L, \lambda^\phi r) &= r^{2\zeta_{KPZ}} \mathcal{C}_{KPZ}(r/L) A(\lambda) / L^{2\zeta_{EW}} \\ &= (r/L)^{2\zeta_{KPZ}} L^{2(\zeta_{KPZ} - \zeta_{EW})} A(\lambda) \mathcal{C}_{KPZ}(r/L) \\ &= (r/L)^{2\zeta_{KPZ}} (\lambda^\phi L)^{2(\zeta_{KPZ} - \zeta_{EW})} \mathcal{C}_{KPZ}(r/L). \end{aligned} \quad (4.7)$$



(a)



(b)

Figure 4.2: Local Log Slope. The measured local-log slope of the height-height correlation function for varying λ and k . The dashed red line is $\zeta = 0.63$, the dashed black line is $\zeta = 1.0$. The curves nearest to $\zeta = 1$ are for small λ , with ζ increasing as we increase λ .

In the last equation we solve for $A(\lambda)$ using the fact that $\mathcal{C}(r/L, \lambda^{\phi r})$ must be a scaling function with only invariant combinations of r , L , λ . Furthermore, we have, at the other limit $\lambda = 0$, that $\mathcal{C}(r/L, 0) \sim (r/L)^2$. Using this, Equation 4.7, and including finite size effects $\exp(-Mr/L)$, we can construct a function that obeys these limits:

$$C(r|L, \lambda) = r^{2\zeta_{KPZ}} (\tanh(\lambda))^{2(\zeta_{KPZ} - \zeta_{EW})\phi} \frac{A_1}{A_2 + (r/L)^{2\zeta_{KPZ} - 2} (\tanh(\lambda)L)^{2(\zeta_{KPZ} - \zeta_{EW})}} \exp(-Mr/L) \quad (4.8)$$

We use as an interpolating form $\tanh(\lambda)$ which at small argument goes as λ , and at large argument goes to 1, and obeys the scaling limits at both qEW and qKPZ. Note that this scaling form has three control variables, and that there exists a singularity at small λ in the form of a divergent non-universal amplitude $A \sim \lambda^{2(\zeta_{KPZ} - \zeta_{EW})\phi}$ in the qKPZ correlation function (eqn 4.5) as $\lambda \rightarrow 0$.

The current form of Equation 4.8 gets us a measure of $\zeta_{EW} > 1$ which is more consistent with the literature than the naive measure of the slope of the power law. It also accounts for finite-size effects in the form and the non-universal amplitude of the qKPZ fixed point.

4.3 UNRESOLVED ISSUES

There remain questions about whether with our automata simulation we are able to see the qEW fixed point. It has been suggested ³ that interactions or lattice effects that break a statistical tilt symmetry (STS) [103] $h \rightarrow h + cx$, will drive the behavior of a qEW simulation to the qKPZ fixed point [19]. It is known that terms which break the STS, such as an anharmonic energy term $(\delta h_x)^2$ in the Hamiltonian [81], or the KPZ term $\lambda(\nabla h)^2$ do

³attributed to discussions with Kay Wiese

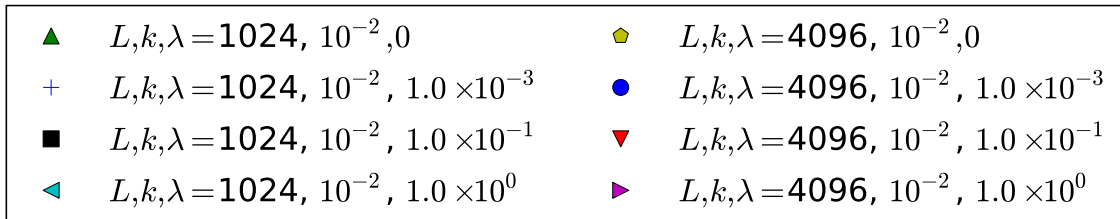
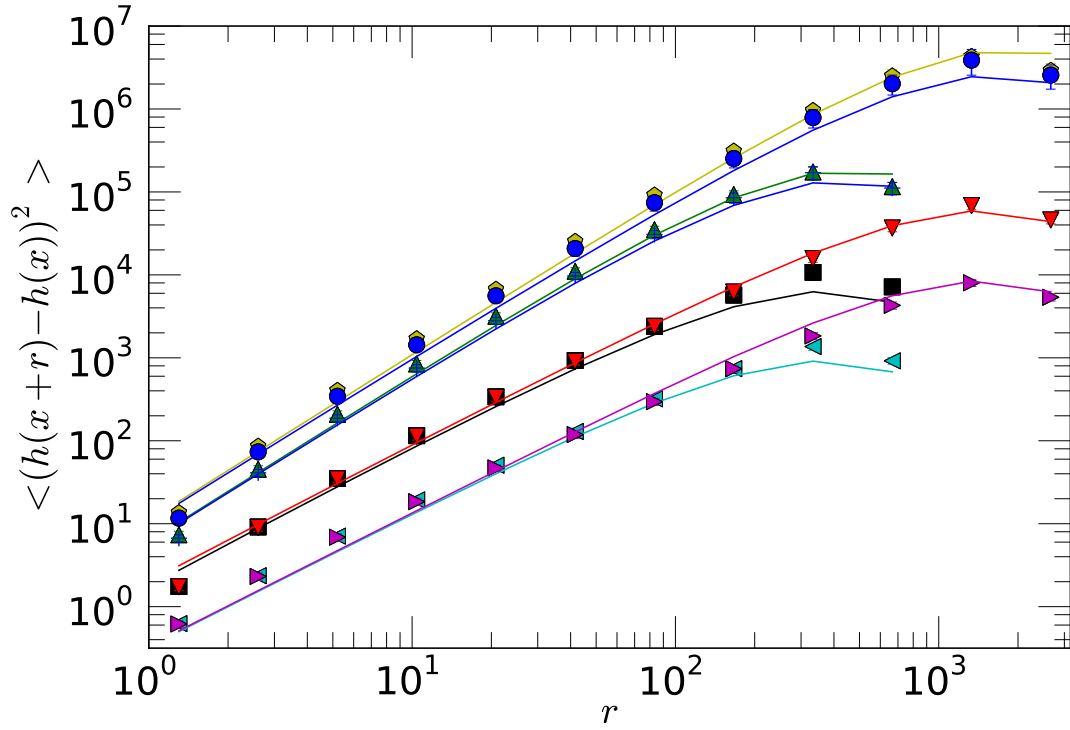


Figure 4.3: Height-height Correlation Function. The numerics generated with an automata code are well described by Equation 4.8 with fit parameters $\zeta_{KPZ} = 0.78 \pm 0.003$, $\zeta_{EW} = 1.20 \pm 0.02$, $\phi = 1.02 \pm 0.04$, $A_1 = 0.37 \pm 0.09$, $A_2 = 1.0 \pm 0.2$, $M = 4.1 \pm 0.07$

exhibit behavior more indicative of a qKPZ fixed point. The lattice automata breaks this symmetry, especially at small distances. However, it has not been systematically studied how or what the magnitude of the effect is.

The roughness exponent ζ can be measured in other ways, other than with the height-height correlation function mentioned above. In particular, we can measure instead the Fourier transform of the heights (the structure factor):

$$S(q) = \left| \sum_j h_j \exp(-iqj) \right|^2 \sim q^{-(1+2\zeta)}. \quad (4.9)$$

Shown in figure 4.4 is our measure of this structure factor for a qEW automata simulation with $\lambda = 0$, we can see that it is unclear (to within error bars) whether or not we are measuring ζ_{qEW} , or are driven to a smaller exponent by the lattice.

We can also measure the roughness exponent with the mean-width fluctuation (Figure 4.5) (the variance of the length of the interface) $\langle w(L)^2 \rangle$ as a function of system-size L ,

$$\langle w(L)^2 \rangle \sim L^{2\zeta}. \quad (4.10)$$

This picture is consistent with what we see in the structure factor, that it is ambiguous whether or not we can see the true qKPZ fixed point, and also, we do not have a definitive measure of ζ to within error bars of our data point.

In the next section, we will present a proposal for a continuous time piecewise linear simulation to address this issue, that although far from being free of lattice effects, can allow us to quantify the symmetry breaking in a more controlled way, and verify the magnitude of its effects.

Another subtlety stems from a relevant term we introduced in our simulations, the self-organizing avalanche-limiting term $D[h](x)$ in Equation 4.1. Since it is a relevant

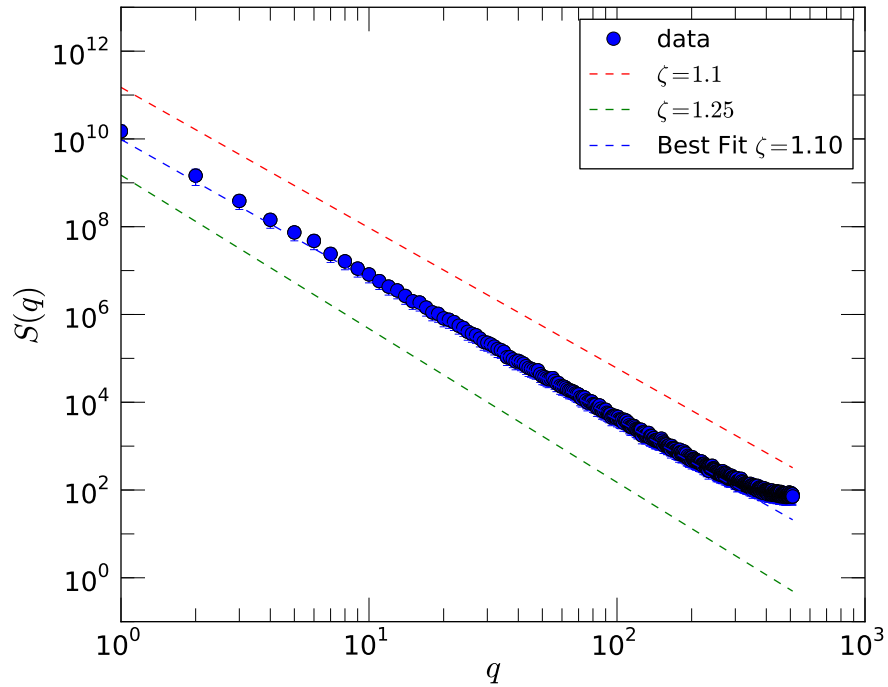


Figure 4.4: Structure Factor. This is the Fourier transform of heights from simulations with the qEW equations with $\lambda = 0$, $k = 0.01$, $\gamma = 1$, and $L = 1024$. According to Equation 4.9, the slope should be given by $-(1 + 2\zeta)$. A best fit yields $\zeta = 1.1 \pm$, however, as one can see from the dashed line $\zeta = 1.25$ is also within error bars of the solution, so there is ambiguity to determining this exponent.

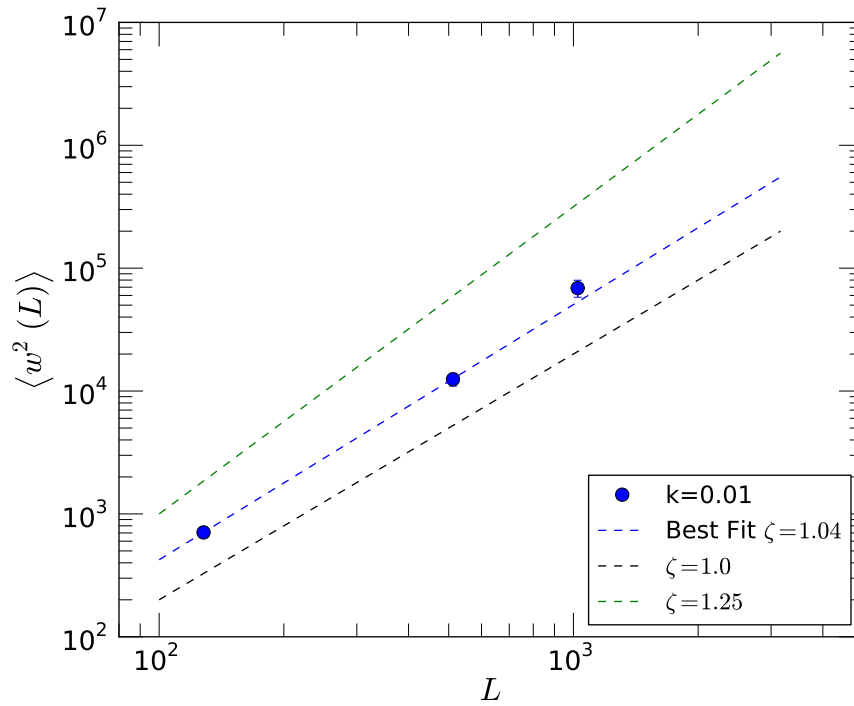


Figure 4.5: Mean-squared Elongation. Measuring the fluctuations in the length of the interface across different system sizes also gives a measure of ζ (Equation 4.10). However, here, with just three data points so far, the best fit is $\zeta = 1.04$.

perturbation away from the fixed point, it should also affect the height-height correlation function. Simulations (including ours) use the demagnetization form $D[h] = -k\langle h \rangle$ described above. However, analytical studies [46, 69] often choose a stopping force $-m^2h(x)$, giving a nice measure of the average length scale. We have found empirically that the correlation length for a demagnetizing field $-k\langle h \rangle$ scales as $L_k \sim k^{-\nu_k}$ with $\nu_k = 0.45$. One can show that using the stopping force one has $L_m \sim 1/m$ [69]. Preliminary simulations show that the mean-squared elongation is cutoff earlier by finite-size effects if we use m instead of the k term.

4.4 CONTINUOUS TIME PIECEWISE LINEAR SIMULATION

In trying to resolve the many issues in accurately capturing our crossover, we have developed and partially implemented a continuous time piecewise linear simulation, which would allow a controlled way of accessing the qEW fixed point. In designing the concept, we also expect the simulation will be flexible enough to test other ideas, such as the widely accepted equivalence of continuous-time and discrete (cellular automata) models.

ODE-solvers exist for simulating interfaces in disordered media, however, they are computationally slow. In the context of avalanches, the bulk of the computational time is spent near the starting and stopping points of avalanches. One resolution is thresholding, assuming the avalanche stops once the velocity crosses below a small threshold. The problem with this approach is it can prematurely split ‘paused’ avalanches in two, and it also sacrifices the accuracy of the configuration at which the front is pinned.

Notice in the Equation 4.1, for the qEW model, $F[u](x) = \gamma \nabla^2 u(x)$ and $D[u](x) = -k\langle u \rangle$ are linear in u . In an intriguing approach to continuous front motion, Rosso and

Krauth [82, 83] introduced a *piecewise linear* disorder force $\eta(u(x), x)$. The linearity of this model, presents an opportunity for using linear algebra to replace the slow pieces of the trajectory, allowing for numerically precise resolution of starting and stopping-points of avalanches.

We can write the linear disorder as,

$$\eta(h(x_i), x_i) = c_i h(x_i) + a_i. \quad (4.11)$$

The stationary points of the qEW model:

$$\partial h / \partial t = \gamma \nabla^2 u + \eta(u(x), x) - m^2 u(x) + H \quad (4.12)$$

are given by solving an (efficient) cyclic tridiagonal system:

$$M_{ij} h_j = w_i \quad (4.13)$$

with diagonal terms $M_{ii} = -2\gamma - 2m^2 + c_i$, off-diagonal terms $M_{i,i\pm 1} = \gamma$, and source terms $w_i = -a_i + H$. If we start out at a stationary configuration with $\partial h / \partial t = 0$ or equivalently $M_{ij} h_j = w_i$, then a new avalanche starts only after H is increased enough to push part of the interface past a point where the local random force slope c_i changes. At such points, we can use an efficient update scheme⁴ to solve for the new minimum without re-decomposing the matrix (even when long-range fields are included). Similarly, during the propagation of an avalanche (when the external field H is fixed) one can solve for the final equilibrium position by a ‘coarse-grained’ method determining the front position within the granularity of the piecewise linear grid, and then a linear solution for the final equilibrium point.

Our current implementation in Python is a hybrid method, using a traditional ODE solver for the fast parts of the avalanche propagation, but solves for the zero-velocity

⁴These are analogues to the Sherman-Morrison formula [104] which update the inverse or other matrix decomposition in a time much faster than the original decomposition.

configuration with the linear-solver after the front velocity slows to a small value. For the crossover studies aforementioned, where precise duration measurements are not crucial, we can implement a variant of Middleton’s algorithm [105] and Rosso and Krauth’s algorithm for a long-range elastic string [82], utilizing no-passing to identify the rough configuration, and then linearly solving for the stationary state. By randomly staggering the force cusps in the piecewise linear force, we can impose the statistical tilt symmetry perfectly (especially if we allow for free boundary conditions). By aligning them, we can induce a (presumably weak) crossover field to qKPZ.

Other questions in the overall field could be answered using this efficient, precise solver. For traditional simulations, how many small avalanches are missed as one creeps up the external field, and how many avalanches are chopped during ‘pauses’ for a given convergence criterion? For experiments, how does the use of a velocity threshold distort the avalanche duration distribution and the average temporal shape? [106]. We could also use our algorithm to test the correspondence between continuous-time and automata models. Are the ‘pauses’ where the avalanches nearly stop, where only a few ‘saddle-node’ degrees of freedom dominate the dynamics, truly irrelevant to the dynamics? Or do the universal predictions of the renormalization-group as reflected in the automata models only describe the avalanches during the collective periods when many degrees of freedom are active? Finally, it is recognized that the continuous-time dynamics is a mean-field fixed point for infinite-range interactions [107], albeit different from the true fixed point [87] describing experiments and simulations⁵. This suggests that for sufficiently long-range forces, there should be a crossover scaling from the saddle-node dynamics for smaller avalanches to the

⁵The development of a ‘cusp’ in the disorder correlator was a key initial result of the functional renormalization group methods; this cusp implies that the long-range automaton with abrupt avalanche initialization and halting is the correct mean-field theory, rather than the slow saddle-node bifurcations of continuous-time mean-field dynamics.

cuspidal dynamics for large avalanches. This picture could perhaps resolve some of the longstanding dynamical puzzles in the Barkhausen noise power spectra [108].

4.5 OUTLOOK

Although the qEW to qKPZ crossover has remaining questions to be resolved, we have presented a clean way of describing the crossover. A new algorithm with more controllable ways of tuning the crossover could lead to a more definitive answer, but the scaling form and methods we have presented with our current simulations should provide a useful framework with which to explore any new data.

SLOPPYSCALING USER DOCUMENTATION

Welcome to *SloppyScaling*! This is a module designed to help match scaling theories to data. Below is a concise user documentation meant to get one started.

A.1 PRELIMINARIES

A.1.1 PYTHON

We use the convenient matplotlib and scipy functionality of Python. The module is written assuming the following dependencies:

- Python 2.7
- Numpy 1.6 and Scipy 0.9
- Matplotlib version 1.0

Most of the functionality is backwards compatible with and has been tested with Python 2.5 and Python 2.6.

A.1.2 INSTALLATION

The most recent version of the code is available for download at <https://github.com/gdurin/SloppyScaling>. Once the files are downloaded, if you would like to be able to access the module through Python in any folder, stick your files in a folder and add the folder path to your PYTHONPATH in your .cshrc, .bashrc, or .profile files. Then you should be good to go!

For example, suppose I put my files in `~/usr/bin/SloppyScaling/`.

For .cshrc the command is:

```
setenv PYTHONPATH /usr/bin/SloppyScaling:${PYTHONPATH}
```

For .bashrc or .profile:

```
export PYTHONPATH=/usr/bin/SloppyScaling:$PYTHONPATH
```

Conversely, you could also just keep a copy of the files in whichever folder you are working in and not worry about all that.

A.1.3 HOW TO LOOK FOR HELP

One way to get a list of the functions available for each module and object and their descriptions is to use the *pydoc* package available in the Python standard library.

pydoc SloppyScaling

In IPython, typing “`help <function name>`” will provide the docstring for each function. For general Python errors, or other issues, turning to google is usually very helpful. Otherwise, e-mail the developers.

A.2 THE SLOPPYSCALING MODULE

The main module is composed of four classes for inputting the scaling theory and importing data. Before we get started, we'll specify some terminology we use below:

- **independent variables** This is the specifications of a particular data set, corresponding most often to control variables in an experiment, such as the temperature and field, (h, t) in the Ising model, or the reverse voltage bias and laser power, (V, W) in a photoelectric experiment.
- **parameters** These are the parameters that are in the scaling theory. For example, when fitting a straight line to (X, Y) data, $Y = AX + B$, (A, B) are the parameters.
- **standard error of the mean** This is meant to represent the fluctuations in estimating the mean from a given sample size. The standard error of the mean is usually estimated by calculating the standard deviation of the samples σ_I , then dividing by the square root of the sample size N , σ_I/\sqrt{N} .
- **covariance matrix** This is a matrix that gives the covariance between data entries i and j , and has dimensions of the $M \times M$, where M is the length of the data set. The covariance matrix gives a two-dimensional estimate of the variance, accounting for correlations between data points, whereas just specifying the standard error of the mean for each value assume uncorrelated data.

A.2.1 THE SCALINGTHEORY CLASS

A `ScalingTheory` object specifies the theory function $Y(X)$, which is also a function of the independent variables for each curve. Parameters specify the function, and most often

should include the universal critical exponents. The theory function should be represented as a string that is a valid Python command. The variables are unpacked on the fly and the string is executed. Example of implementation:

```
sizeHisto = ScalingTheory('S**(-tau)*numpy.exp(-(S*(R-Rc)**sigma)/XS)**nS)',      # theory equation
                          'tau, sigma, XS, nS, Rc', (1.5,0.5,1.0,1.0,2.0),          # parameter names and values
                          independentNames = 'R',                                # independent variable names
                          scalingX = 'S*r**sigma', scalingY = 'D*S**tau',        # scaling variables
                          scalingXTeX = r'$S r^\sigma$',                          # LaTeX forms for plotting purposes
                          scalingYTeX = r'$D S^\tau$',
                          title= 'Avalanche histogram$',                          # title of theory
                          scalingTitle= 'Avalanche histogram scaling plot',
                          Xname = 'S', XscaledName='Ss', Yname = 'D',            # names for variables
                          normalization = True)                                  # whether function needs normalization
```

A.2.2 THE DATA CLASS

A Data object contains a series of curves labeled by independent variables. Data X, Y, ErrorBarY (optional) is stored separately (so they need to be the same length). The label for each set of curves should be defined as a tuple, for example in the Ising model the label would be (h, t) for each data set. The ErrorBarY, if provided, is assumed to be the standard errors of the means. Each curve can be loaded from a file with the method **InstallCurve**, it assumes the file is read in file format. There is also a method **LoadCovMatrix**, which attaches a covariance matrix to each curve, to be used for fitting and calculation of error bars if desired.

A.2.3 THE MODEL CLASS

A Model object connects a ScalingTheory object to a Data object. It's primary task is to calculate the residuals (difference between theory and data, weighted by error bars or the covariance matrix) (method:**Residual**) and the cost (method:**Cost**). According to

these, it can provide a best fit of the theory to the data (method:**BestFit**), and plot the results of the fit (method:**PlotBestFit**) and the scaling collapse.

A.2.4 THE COMPOSITEMODEL CLASS

A CompositeModel object combines several Model objects into one. The main job of the CompositeModel is to combine parameter lists and initial values into a single structure, and then to impose that structure on the individual theories. Shared parameters are identified and dealt with accordingly. CompositeModel makes use of Model class methods for plotting and calculating costs.

A.3 ADDITIONAL CAPABILITIES

A.3.1 FITTING TECHNIQUES

Various options exist for fitting with nonlinear least-squares algorithms in SloppyScaling, the can be specified when calling the methods **Model.BestFit** or **CompositeModel.BestFit**, with the option *method= <keyword>*. Keywords and corresponding algorithms are as follows:

- 'lm' or None: `scipy.optimize` Levenberg-Marquadt
- 'lm.accel': Levenberg-Marquardt + acceleration
- 'bold' : Delayed gratification
- 'boldAccel': delayed gratification + acceleration

Details on these algorithms can be found in Ref. [109].

Other than a choice of fitting algorithm, we can tweak the fitting routine in the following ways. One can also choose to fix parameters to various values by the optional argument *fixedParams* with a list of tuples [(‘param1’, val1), (‘param2’, val2)...] and so on. We can also add priors to the Cost function by providing them to the **Model.Residual** method via the optional argument *dictResidual* in the form of a dictionary, with the keys being the independent values of the data set to which they apply.

A.3.2 MONTE-CARLO ENSEMBLE PREDICTIONS

We include capabilities to perform importance sampling [110] on a *SloppyScaling* Model, to access this, include in your script or in your IPython terminal

```
from ensemble import ensemble
```

The function *ensemble* takes a *SloppyScaling* Model and does a weighted Monte-Carlo random walk in parameter space to generate an ensemble of parameters of an acceptable cost range defined by the magnitude of the best fit cost. The resulting ensemble is saved as a Python *pickle* object, which then you can use directly with the *SloppyScaling* **Model** class function *PlotEnsemblePredictions* to make shaded plots of your scaling theory, or with the module *PlotEnsembles* to make histograms of your ensemble predictions, projections of your ensemble cloud to 2 or 3-dimensions, or the shaded plots of your scaling theory. Figure A.1 shows an example of such a shaded plot, which reflects the range of uncertainty for the theory function against a data set measuring piano tuners in cities (we will discuss this example in Section A.4.1).

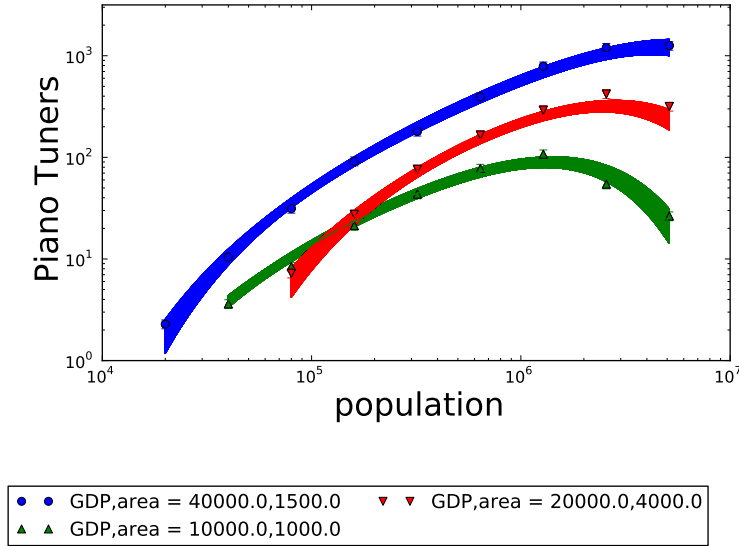


Figure A.1: Shaded Theory Predictions The colored regions represent the uncertainty in the theory generated from a Monte-Carlo sampling of the parameter space.

A.3.3 CONVENIENCE FUNCTIONS FOR ORGANIZATION

There are a few other convenience functions we provide in the module *Utils*, which include generating a list of tuples for all combinations of the independent variables when given a list or range, and generating a dictionary of *matplotlib* colors plus symbols for use in plotting each individual data set.

A.4 EXAMPLES

The way I like to program is just try things and see if they work. Hopefully the following examples are descriptive enough to get you launched.

A.4.1 EXAMPLE OF ONE SCALING FUNCTION

In the first example, we will try to measure the scaling of piano tuners in a cities in three regions (this is made up data). This is a classic Fermi problem, but also inspired by the paper [111]. We've decided that the number of piano tuners in a city scales roughly with its population, but is cut off by limitations on the space available (so area means average area per capita). There is also a baseline level of piano tuners determined by whether the average population can afford pianos, which is dependent on GDP. So we have a theory that the number of piano tuners is a function of area and GDP.

$$\text{pianotuners} = \text{population}^{\alpha} F\left(\frac{\text{area}^{\gamma}}{\text{population}}, \frac{\text{population}^{\beta}}{GDP}\right) \quad (\text{A.1})$$

We can set up the script included below to define a **ScalingTheory**, a **Data**, and a **Model**, which we will name **City**.

```
1 from numpy import exp
2 import os
3 import SloppyScaling
4 reload(SloppyScaling)
5 import WindowScalingInfo as WS
6 reload(WS)
7 import Utils
8 reload(Utils)
9
10 name = 'piano_tuners' # This is the name used in the data files
11
12 #####
13 # set up all the variables for the ScalingTheory
14 #####
15
16 Xname = 'x'
17 XnameTeX = 'population'
18 XscaledName = 'xs'
```

```

19 Xscaled = 'x/GDP**beta'
20 XscaledTeX = r'$population^{\beta}/GDP$'
21 WscaledName = 'As'
22 Wscaled = 'area**gamma/x'
23 WscaledTeX = r'$area^{\gamma}/population$'
24
25 Yname = 'PianoTuners'
26 YnameTeX = 'Piano Tuners'
27 Ytheory = 'x**alpha*exp(-c*(1.0*area**gamma/x))*exp(-a*(x/(1.0*GDP**beta)))*(d*GDP
           /10**4)' # this is the theory of how piano tuners scale
28 Yscaled = 'x**(-alpha)*PianoTuners*(10**4/(d*GDP))' # formula for scaling collapse
29 YscaledTeX = r'tuners $\times$ population^{-\alpha} / F(GDP)$'
30
31 title = 'Piano Tuners in the City'
32
33 scalingTitle = 'Scaling Collapse'
34
35 parameterNames = "alpha,beta,gamma,a,c,d"
36
37 # initial parameter guess for fitting
38 initialParameterValues = (1.1,0.9,1.2,0.003,0.1,0.0005)
39
40 # initialize a ScalingTheory with all the variables defined above
41 theory = SloppyScaling.ScalingTheory(Ytheory, parameterNames, \
42     initialParameterValues, 'GDP,area', \
43     scalingX = Xscaled, scalingY = Yscaled,scalingW = Wscaled,\
44     scalingXTex = XscaledTeX, \
45     scalingYTeX = YscaledTeX, \
46     scalingWTeX = WscaledTeX, \
47     title = title, \
48     scalingTitle = scalingTitle, \
49     Xname=Xname, XnameTeX=XnameTeX, XscaledName=XscaledName, \
50     Yname=Yname, YnameTeX=YnameTeX, \
51     normalization = None)
52
53 # initialize a Data object
54 data = SloppyScaling.Data()
55

```

```

56 #####
57 # declare the data set labels, independent variables
58 #####
59
60 independentNames = 'GDP','area'
61 independentValues= [(40000.0,1500.0),(10000.0,1000.0),(20000.0,4000.0)]
62
63 Symbol, Color = Utils.MakeSymbolsAndColors(independentValues)
64
65 #####
66 # load the data
67 #####
68 loaded = 0
69 for independent in independentValues:
70     GDP, area = independent
71     fileName = name+'_gdp_'+str(GDP)+'_area_'+str(area)+'.txt'
72     success = data.InstallCurve(independent, fileName, \
73         defaultFractionalError=0.1,\
74         pointSymbol=Symbol[independent], \
75         pointColor=Color[independent])
76     loaded += success
77
78 nFiles = len(independentValues)
79
80 if loaded == nFiles:
81     print "Loaded %2d/%2d files (%s)" % (loaded, nFiles, name)
82 else:
83     print "======"
84     print "Attention! %2d/%2d files are missing (%s)" % (nFiles-loaded, nFiles, name)
85     print "======"
86
87 #####
88 # combine theory and data into Model
89 #####
90
91 City = SloppyScaling.Model(theory, data, name, independentValues)

```

Now that we have the **City** model set up, we can open IPython, and say:

```
run CityModule.py
```

To see what the **City** model can do, let us type "City." into the command prompt and press tab, you should see a list with all the functions.

```
In [15]: City.  
City.AnalyJac           City.Residual  
City.BestFit            City.SST  
City.Cost               City.data  
City.MergeFixedAndVariableParams City.getAxis  
City.PlotBestFit        City.getLabel  
City.PlotEnsemblePredictions City.name  
City.PlotFunctions      City.sorting  
City.PlotResiduals     City.theory  
City.R_square
```

Let's execute

```
City.PlotBestFit()
```

, which generates the output:

```
initial cost = 594478.59707  
fitting took (mins) 0.00405515034993  
number of function evals: [177]  
fitting took (mins) 0.00401621659597  
number of function evals: [353]  
optimized cost = 28.4257680692  
=====  
Fitted Parameters (with one sigma error) =====  
alpha= 1.062805 +/- 0.042500  
beta= 0.932665 +/- 0.075609  
gamma= 1.087784 +/- 0.096873  
a= 0.004082 +/- 0.002753
```

c= 11.786177 +/- 9.273463

d= 0.000080 +/- 0.000043

=====

and three figures of the fit (Figure A.2), the collapse (Figure A.3, and the weighted residual (Figure A.4).

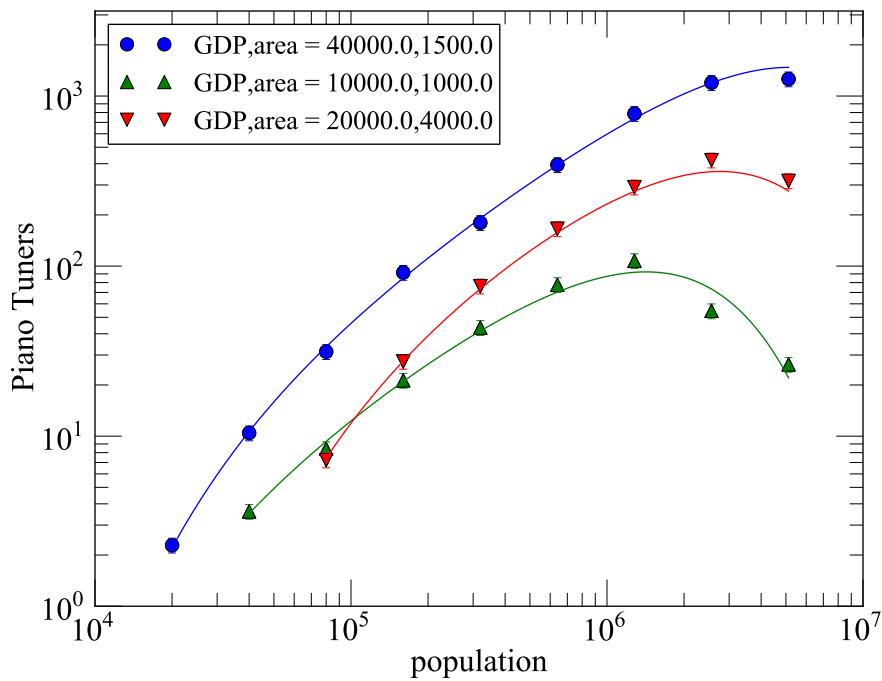


Figure A.2: The Piano Tuner Data and Fit

A.4.2 EXAMPLE OF A JOINT THEORY

Now that we know how to set up an individual theory, setting up a **CompositeModel** is just one step more. Let us measure instead the number of rats in a city, and let's say we've set up this measure as a separate **Model** called **Rats**. And the intriguing thing about the

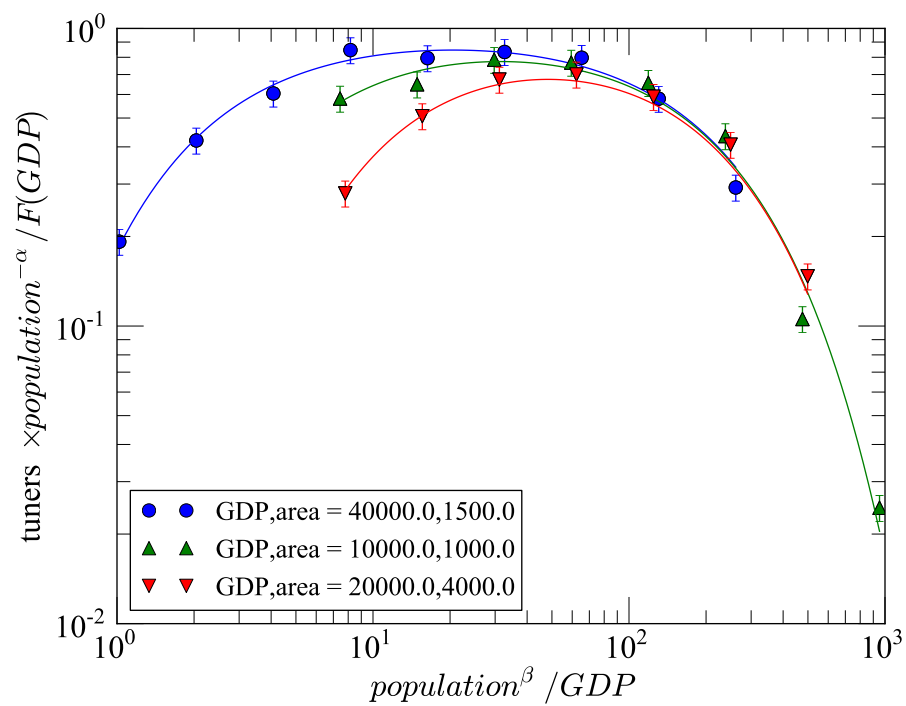


Figure A.3: The Piano Tuner Data Collapse

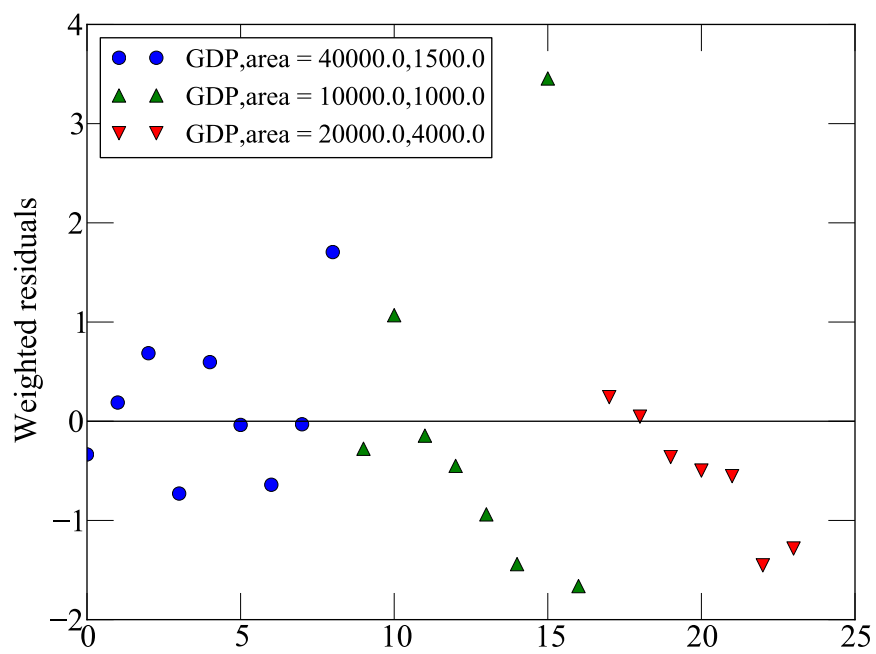


Figure A.4: The Piano Tuner Fit Residuals

rats is that they roughly scale the same way with population size as piano tuners do with exponent α , and the scale invariant quantities and their exponents β and γ are also the same, but of course there are less rats when the population is sparser and richer, so the scaling function is different and given by something like $G\left(\frac{\text{area}^\gamma}{\text{population}}, \frac{\text{population}^\beta}{GDP}\right)$.

$$\text{rats} = \text{population}^\alpha G\left(\frac{\text{area}^\gamma}{\text{population}}, \frac{\text{population}^\beta}{GDP}\right) \quad (\text{A.2})$$

To connect these two models, the commands one needs to run is:

```
import CityModule as City
import RatsModule as Rats

jointModel = SloppyScaling.CompositeModel("RatsAndPiano")

obj_mod = City
m = getattr(obj_mod, City)
jointModel.InstallModel("City", m)

obj_mod = Rats
m = getattr(obj_mod, Rats)
jointModel.InstallModel("Rats", m)
```

and you have a **CompositeModel** that will fit all three models at once, with shared parameters. For example you can execute:

```
jointModel.BestFit()
```

which generates the output:

```
initial cost = 597725.020273
fitting took time (mins): 0.0143965482712
number of function_calls: [582]
optimized cost = 66.8324647715
```

```
=== Fitting parameters (with one sigma error)=====
```

```
alpha = 1.111934 +/- 0.013164
beta = 0.868941 +/- 0.048116
gamma = 1.157076 +/- 0.086911
a = 0.002368 +/- 0.001056
c = 6.323110 +/- 4.245200
d = 0.000043 +/- 0.000007
r1 = 0.000467 +/- 0.000293
r2 = 0.163527 +/- 0.090991
r3 = 0.043401 +/- 0.006945
```

```
=====
```

where r1, r2, r3 are the parameters associated with the rats theory, alpha, beta, gamma the parameters shared between the two theories.

Six figures total will be shown when executing the above command, three of them from the piano tuners data and fit like the ones shown in the single theory (piano tuners) example (Figure A.2, A.3, A.4), in addition there will be figures from the data and theory of the rats, including the fit (Figure A.5), the collapse (Figure A.6), and the residuals (Figure A.4).

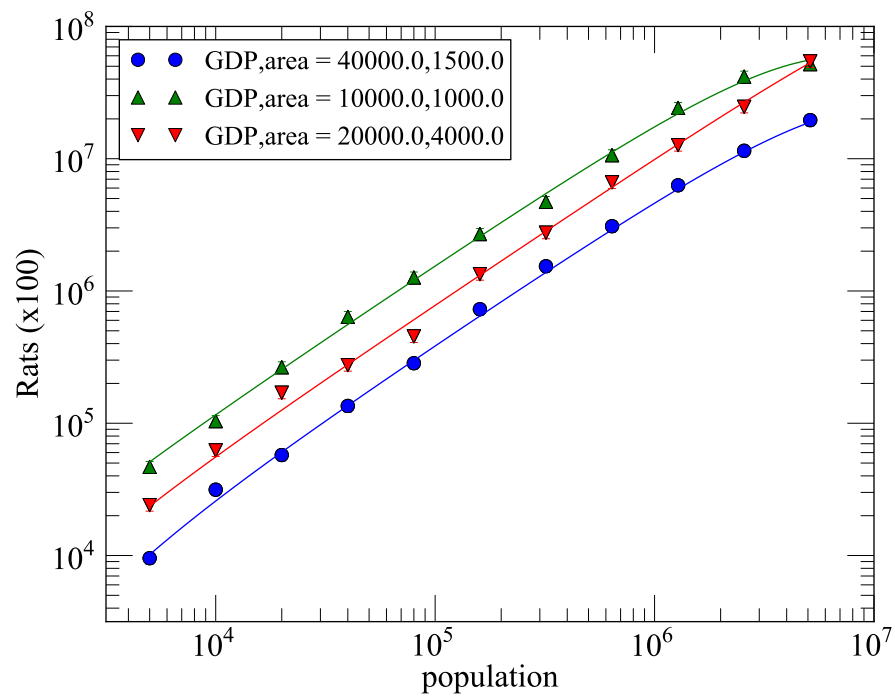


Figure A.5: Rats in the City Data and Fit

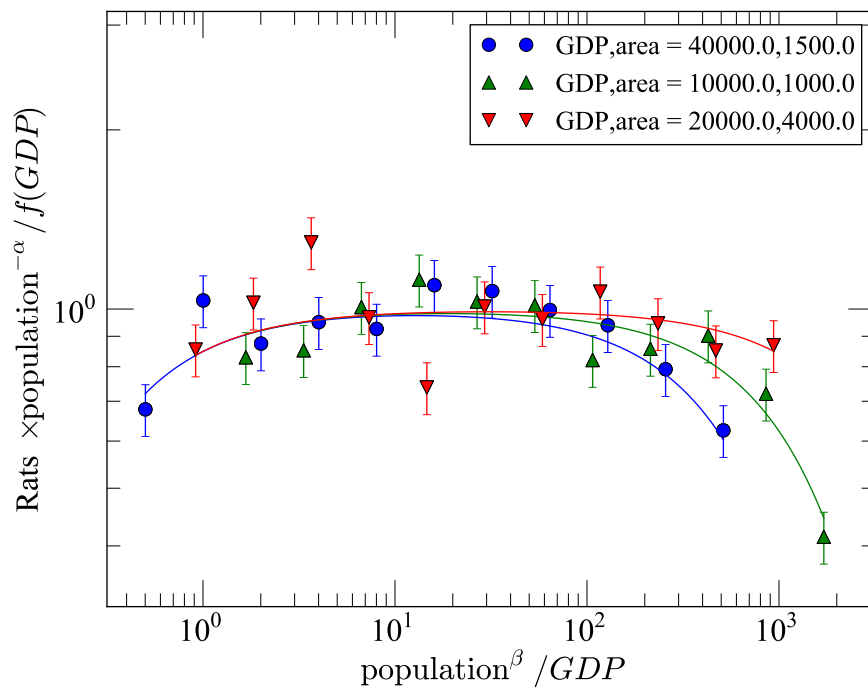


Figure A.6: Rats in the City Data Collapse

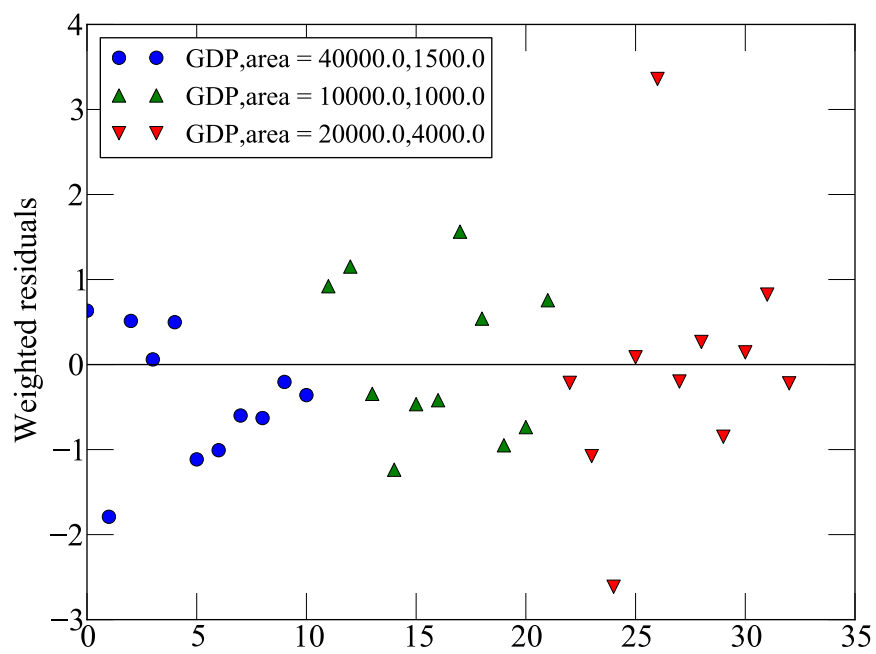


Figure A.7: Rats in the City Residuals

A.5 FREQUENTLY ASKED QUESTIONS

- **Why doesn't your program automatically detect the scaling function for my data?**

There are actually efforts out there that try to find equations and detect math relations: for example: Eureka (<http://creativemachines.cornell.edu/eureka>). We have not done this. In our experience, humans are still better than computers at finding an elegant function which obeys the limits we know for problems in critical phenomena. Also, in the process of parametrizing and refining the answer, we tend to learn a lot about the system at hand. However, having *SloppyScaling* interface with something like Eureka would be very valuable functionality.

- **This is too difficult. Is there an easier interface?**

We find that the scripting environment is very flexible for use, however, for people who want a more intuitive interface, there is a GUI under development [22].

REFERENCES

1. L. Onsager, “Crystal statistics. i. a two-dimensional model with an order-disorder transition,” *Physical Review* **65** no. 3-4, (1944) 117.
2. B. M. McCoy and T. T. Wu, *The Two-Dimensional Ising Model*. Harvard University Press, 1973.
3. V. Yurov and A. B. Zamolodchikov, “Correlation functions of integrable 2d models of the relativistic field theory: Ising model,” *International Journal of Modern Physics A* **6** no. 19, (1991) 3419–3440.
4. G. Delfino and G. Mussardo, “The spin-spin correlation function in the two-dimensional Ising model in a magnetic field at $T = T_c$,” *Nuclear Physics B* **455** no. 3, (1995) 724–758.
5. B. B. Machta, *Criticality in Cellular Membranes and the Information Geometry of Simple Models*. PhD thesis, Cornell University, 2012.
<http://www.lassp.cornell.edu/sethna/pubPDF/MachtaPhD.pdf>.
6. E. Puppin, “Statistical properties of Barkhausen noise in thin Fe films,” *Phys. Rev. Lett.* **84** no. 23, (2000) 5415–5418.
7. K. S. Ryu, H. Akinaga, and S. C. Shin, “Tunable scaling behaviour observed in Barkhausen criticality of a ferromagnetic film,” *Nat. Phys.* **3** no. 8, (2007) 547–550.
8. G. Durin and S. Zapperi, “The Barkhausen effect,” in *The Science of Hysteresis*, G. Bertotti and I. Mayergoyz, eds., vol. II. Apr., 2004. [arXiv:cond-mat/0404512](https://arxiv.org/abs/cond-mat/0404512).
9. A. Rosso, P. Le Doussal, and K. J. Wiese, “Avalanche-size distribution at the depinning transition: A numerical test of the theory,” *Phys. Rev. B* **80** (Oct, 2009) 144204. <http://link.aps.org/doi/10.1103/PhysRevB.80.144204>.
10. A. Mughal, L. Laurson, G. Durin, and S. Zapperi, “Effect of dipolar interactions for domain-wall dynamics in magnetic thin films,” *Magnetics, IEEE Transactions on* **46** no. 2, (2010) 228–230.
11. K. A. Dahmen, J. P. Sethna, and O. Perkovic, “Hysteresis, Barkhausen noise, and disorder induced critical behavior,” *IEEE Transactions On Magnetics* **36** (2000) 3150–3154.
12. A. Dobrinevski, P. Le Doussal, and K. J. Wiese, “Nonstationary dynamics of the alessandro-beatrice-bertotti-montorsi model,” *Physical Review E* **85** no. 3, (2012) 031105.
13. M. Kardar, “Nonequilibrium dynamics of interfaces and lines,” *Phys. Rep.* **301** (July, 1998) 85–112, [arXiv:cond-mat/9704172](https://arxiv.org/abs/cond-mat/9704172).
14. A. L. Barabási and H. E. Stanley, *Fractal concepts in surface growth*. Cambridge Univ Pr, 1995.

15. T. Nattermann, S. Stepanow, L.-H. Tang, and H. Leschhorn, “Dynamics of interface depinning in a disordered medium,” *Journal de Physique II* **2** no. 8, (1992) 1483–1488.
16. O. Narayan and D. S. Fisher, “Threshold critical dynamics of driven interfaces in random media,” *Phys. Rev. B* **48** (1993) 7030–7042.
17. H. Leschhorn, “Interface depinning in a disordered medium—numerical results,” *Physica A* **195** no. 3-4, (1993) 324–335.
18. H. Leschhorn, “Anisotropic interface depinning: Numerical results,” *Phys. Rev. E* **54** no. 2, (Aug, 1996) 1313–1320.
19. P. Le Doussal and K. J. Wiese, “Functional renormalization group for anisotropic depinning and relation to branching processes,” *Phys. Rev. E* **67** no. 1, (Jan, 2003) 016121.
20. G. Durin, Y.-J. Chen, and J. P. Sethna, “Sloppy scaling software.”
<http://www.lassp.cornell.edu/sethna/SloppyScaling/SloppyScaling.htm>, 2010.
21. M. Transtrum, *Information Geometry for Nonlinear Least-Squares Data Fitting and Numerical Calculation of the Superconducting Superheating Field*. PhD thesis, Cornell University, 2011.
<http://www.lassp.cornell.edu/sethna/pubPDF/TranstrumPhD.pdf>.
22. G. Durin, Y.-J. Chen, and J. P. Sethna, “Sloppy scaling software (gui development).”
<https://github.com/gdurin/SloppyScaling/tree/gui/GUI-branch>, 2013.
23. A. Zamolodchikov, “Integrals of motion and S-matrix of the (scaled) $T = T_c$ Ising model with magnetic field,” *Int. J. Mod. Phys. A* **4** no. 16, (1989) 4235–4248.
24. H. Tarko and M. Fisher, “Theory of critical point scattering and correlations. iii. the Ising model below t_c and in a field,” *Physical Review B* **11** no. 3, (1975) 1217.
25. M. Fisher and R. Burford, “Theory of critical-point scattering and correlations. i. the Ising model,” *Physical Review* **156** no. 2, (1967) 583.
26. M. Caselle, M. Hasenbusch, A. Pelissetto, and E. Vicari, “The critical equation of state of the two-dimensional ising model,” *Journal of Physics A: Mathematical and General* **34** (2001) 2923.
27. S. Veatch, O. Soubias, S. Keller, and K. Gawrisch, “Critical fluctuations in domain-forming lipid mixtures,” *Proceedings of the National Academy of Sciences* **104** no. 45, (2007) 17650.
28. A. R. Honerkamp-Smith, S. L. Veatch, and S. L. Keller, “An introduction to critical points for biophysicists; observations of compositional heterogeneity in lipid membranes,” *Biochimica et Biophysica Acta - Biomembranes* **1788** no. 1, Sp. Iss. SI, (2009) 53–63.
29. S. L. Veatch, P. Cicuta, P. Sengupta, A. Honerkamp-Smith, D. Holowka, and B. Baird, “Critical fluctuations in plasma membrane vesicles,” *ACS Chemical Biology* **3** no. 5,

(2008) 287–293.

30. B. B. Machta, S. Papanikolaou, J. P. Sethna, and S. L. Veatch, “Minimal model of plasma membrane heterogeneity requires coupling cortical actin to criticality,” *Biophysical journal* **100** no. 7, (2011) 1668–1677.
31. B. B. Machta, S. L. Veatch, and J. P. Sethna, “Critical casimir forces in cellular membranes,” *Phys. Rev. Lett.* **109** (Sep, 2012) 138101.
32. F. Heberle, J. Wu, S. Goh, R. Petruzielo, and G. Feigenson, “Comparison of three ternary lipid bilayer mixtures: Fret and esr reveal nanodomains,” *Biophysical journal* **99** no. 10, (2010) 3309–3318.
33. S. Veatch and S. Keller, “Seeing spots: Complex phase behavior in simple membranes,” *Biochimica Et Biophysica Acta - Molecular Cell Research* **1746** no. 3, (DEC 30, 2005) 172.
34. P. Schofield, “Parametric representation of the equation of state near a critical point,” *Physical Review Letters* **22** no. 12, (1969) 606–608.
35. P. Schofield, J. Litster, and J. Ho, “Correlation between critical coefficients and critical exponents,” *Physical Review Letters* **23** no. 19, (1969) 1098–1102.
36. C. N. Yang, “The spontaneous magnetization of a two-dimensional Ising model,” *Phys. Rev.* **85** (Mar, 1952) 808–816. <http://link.aps.org/doi/10.1103/PhysRev.85.808>.
37. T. Wu, B. McCoy, C. Tracy, and E. Barouch, “Spin-spin correlation functions for the two-dimensional Ising model: Exact theory in the scaling region,” *Physical Review B* **13** no. 1, (1976) 316.
38. A. Aharony and M. E. Fisher, “Universality in analytic corrections to scaling for planar Ising models,” *Phys. Rev. Lett.* **45** (Sep, 1980) 679–682. <http://link.aps.org/doi/10.1103/PhysRevLett.45.679>.
39. M. Barma and M. E. Fisher, “Two-dimensional Ising-like systems: Corrections to scaling in the Klauder and double-Gaussian models,” *Physical Review B* **31** no. 9, (1985) 5954.
40. A. Aharony and M. E. Fisher, “Nonlinear scaling fields and corrections to scaling near criticality,” *Phys. Rev. B* **27** (Apr, 1983) 4394–4400. <http://link.aps.org/doi/10.1103/PhysRevB.27.4394>.
41. J. J. Waterfall, F. P. Casey, R. N. Gutenkunst, K. S. Brown, C. R. Myers, P. W. Brouwer, V. Elser, and J. P. Sethna, “Sloppy-model universality class and the Vandermonde matrix,” *Physical review letters* **97** no. 15, (2006) 150601.
42. L. N. Trefethen *et al.*, *Chebfun Version 4.2*. The Chebfun Development Team, 2011. <http://www.maths.ox.ac.uk/chebfun/>.
43. “Ising correlations supplemental materials.” <http://www.lassp.cornell.edu/sethna/ScalingFunctions/2DIsing/>.
44. U. Wolff, “Collective Monte-Carlo updating for spin systems,” *Physical Review Letters*

- 62** no. 4, (JAN 23, 1989) 361–364.
45. J. P. Sethna, K. A. Dahmen, and C. R. Myers, “Crackling noise,” *Nature* **410** no. 6825, (2001) 242–250.
 46. P. Le Doussal and K. J. Wiese, “Distribution of velocities in an avalanche,” *EPL (Europhysics Letters)* **97** no. 4, (2012) 46004.
 47. A. Magni, G. Durin, S. Zapperi, and J. P. Sethna, “Visualization of avalanches in magnetic thin films: temporal processing,” *J. Stat. Mech: Theory Exp.* **2009** (2009) P01020.
 48. A. Schwarz, M. Liebmann, U. Kaiser, R. Wiesendanger, T. W. Noh, and D. W. Kim, “Visualization of the Barkhausen effect by magnetic force microscopy,” *Phys. Rev. Lett.* **92** no. 7, (2004) 77206.
 49. D. A. Christian, K. S. Novoselov, and A. K. Geim, “Barkhausen statistics from a single domain wall in thin films studied with ballistic hall magnetometry,” *Phys. Rev. B* **74** no. 6, (Aug, 2006) 064403.
 50. L. H. Tang and H. Leschhorn, “Pinning by directed percolation,” *Phys. Rev. A* **45** no. 12, (1992) 8309–8312.
 51. S. V. Buldyrev, A.-L. Barabási, F. Caserta, S. Havlin, H. E. Stanley, and T. Vicsek, “Anomalous interface roughening in porous media: Experiment and model,” *Phys. Rev. A* **45** no. 12, (Jun, 1992) R8313–R8316.
 52. S. V. Buldyrev, A. L. Barabási, S. Havlin, J. Kertesz, H. E. Stanley, and H. S. Xenias, “Anomalous interface roughening in 3D porous media: experiment and model,” *Physica A* **191** no. 1-4, (1992) 220–226.
 53. H. Leschhorn, “Anisotropic interface depinning: Numerical results,” *Phys. Rev. E* **54** no. 2, (Aug, 1996) 1313–1320.
 54. E. Vives, J. Ortín, L. Mañosa, I. Ràfols, R. Pérez-Magrané, and A. Planes, “Distributions of avalanches in martensitic transformations,” *Phys. Rev. Lett.* **72** (Mar, 1994) 1694–1697. <http://link.aps.org/doi/10.1103/PhysRevLett.72.1694>.
 55. F.-J. Pérez-Reche, B. Tadic, L. Mañosa, A. Planes, and E. Vives, “Driving rate effects in avalanche-mediated first-order phase transitions,” *Phys. Rev. Lett.* **93** (Nov, 2004) 195701. <http://link.aps.org/doi/10.1103/PhysRevLett.93.195701>.
 56. M. S. Welling, C. M. Aegerter, and R. J. Wijngaarden, “Self-organized criticality induced by quenched disorder: Experiments on flux avalanches in NbH_x films,” *Phys. Rev. B* **71** no. 10, (2005) 104515.
 57. K. J. Maloy and J. Schmittbuhl, “Dynamical event during slow crack propagation,” *Phys. Rev. Lett.* **87** (Aug, 2001) 105502. <http://link.aps.org/doi/10.1103/PhysRevLett.87.105502>.
 58. R. Planet, S. Santucci, and J. Ortín, “Avalanches and Non-Gaussian Fluctuations of the Global Velocity of Imbibition Fronts,” *Phys. Rev. Lett.* **102** no. 9, (2009) 94502.

59. C. M. Aegerter, R. Günther, and R. J. Wijngaarden, “Avalanche dynamics, surface roughening, and self-organized criticality: Experiments on a three-dimensional pile of rice,” *Phys. Rev. E* **67** no. 5, (2003) 51306.
60. C. M. Aegerter, K. A. Lőrincz, M. S. Welling, and R. J. Wijngaarden, “Extremal dynamics and the approach to the critical state: Experiments on a three dimensional pile of rice,” *Phys. Rev. Lett.* **92** no. 5, (2004) 58702.
61. D.-H. Kim, S.-B. Choe, and S.-C. Shin, “Direct observation of barkhausen avalanche in co thin films,” *Phys. Rev. Lett.* **90** no. 8, (Feb, 2003) 087203.
62. S. Papanikolaou, F. Bohn, R. L. Sommer, G. Durin, S. Zapperi, and J. P. Sethna, “Universality beyond power laws and the average avalanche shape,” *Nat. Phys.* (2011) .
63. O. Perković, K. A. Dahmen, and J. P. Sethna, “Disorder-induced critical phenomena in hysteresis: Numerical scaling in three and higher dimensions,” *Phys. Rev. B* **59** no. 9, (1999) 6106.
64. F. Colaiori, “Exactly solvable model of avalanches dynamics for Barkhausen crackling noise,” *Adv. Phys.* **57** no. 4, (2008) 287–359.
65. H. Leschhorn and L. H. Tang, “Avalanches and correlations in driven interface depinning,” *Phys. Rev. E* **49** no. 2, (1994) 1238–1245.
66. A. Rosso and W. Krauth, “Origin of the roughness exponent in elastic strings at the depinning threshold,” *Phys. Rev. Lett.* **87** no. 18, (Oct, 2001) 187002.
67. J. P. Sethna, K. A. Dahmen, and O. Perkovic, “Random-Field Ising Models of Hysteresis,” in *The Science of Hysteresis*, G. Bertotti and I. Mayergoyz, eds., vol. II. Apr., 2004. [arXiv:cond-mat/0406320](https://arxiv.org/abs/cond-mat/0406320).
68. A. Rosso, P. Le Doussal, and K. J. Wiese, “Numerical calculation of the functional renormalization group fixed-point functions at the depinning transition,” *Phys. Rev. B* **75** no. 22, (2007) 220201.
69. P. Le Doussal and K. J. Wiese, “Size distributions of shocks and static avalanches from the functional renormalization group,” *Phys. Rev. E* **79** no. 5, (May, 2009) 051106.
70. L. H. Tang and H. Leschhorn, “Pinning by directed percolation,” *Phys. Rev. A* **45** no. 12, (1992) 8309–8312.
71. K. Sneppen, “Self-organized pinning and interface growth in a random medium,” *Phys. Rev. Lett.* **69** no. 24, (1992) 3539–3542.
72. L. A. N. Amaral, A.-L. Barabási, S. V. Buldyrev, S. T. Harrington, S. Havlin, R. Sadr-Lahijany, and H. E. Stanley, “Avalanches and the directed percolation depinning model: Experiments, simulations, and theory,” *Phys. Rev. E* **51** no. 5, (May, 1995) 4655–4673.
73. S. L. Frederiksen, K. W. Jacobsen, K. S. Brown, and J. P. Sethna, “Bayesian ensemble approach to error estimation of interatomic potentials,” *Phys. Rev. Lett.* **93** no. 16, (Oct, 2004) 165501.

74. B. Cerruti and S. Zapperi, “Barkhausen noise from zigzag domain walls,” *J. Stat. Mech.: Theory Exp.* **2006** (2006) P08020.
75. M. K. Transtrum, B. B. Machta, and J. P. Sethna, “Geometry of nonlinear least squares with applications to sloppy models and optimization,” *Phys. Rev. E* **83** no. 3, (2011) 036701.
76. M. K. Transtrum, B. B. Machta, and J. P. Sethna, “Why are Nonlinear Fits to Data so Challenging?,” *Phys. Rev. Lett.* **104** no. 6, (2010) 60201.
77. J. W. Essam, A. J. Guttmann, and K. De’Bell, “On two-dimensional directed percolation,” *Journal of Physics A: Mathematical and General* **21** (1988) 3815.
78. H. A. Makse and L. A. N. Amaral, “Scaling behavior of driven interfaces above the depinning transition,” *EPL* **31** (1995) 379.
79. P. Le Doussal and K. J. Wiese, “Functional renormalization group for anisotropic depinning and relation to branching processes,” *Phys. Rev. E* **67** no. 1, (2003) 16121.
80. H. Leschhorn, T. Nattermann, S. Stepanow, and L. H. Tang, “Driven interface depinning in a disordered medium,” *Ann. Physik* **6** (1997) 1–34.
81. A. Rosso and W. Krauth, “Origin of the roughness exponent in elastic strings at the depinning threshold,” *Phys. Rev. Lett.* **87** no. 18, (Oct, 2001) 187002.
82. A. Rosso and W. Krauth, “Roughness at the depinning threshold for a long-range elastic string,” *Phys. Rev. E* **65** (2002) 025101.
83. A. Rosso, A. K. Hartmann, and W. Krauth, “Depinning of elastic manifolds,” *Phys. Rev. E* **67** (2003) 021602.
84. L.-H. Tang and H. Leschhorn, “Pinning by directed percolation,” *Phys. Rev. A* **45** no. 12, (Jun, 1992) R8309–R8312.
85. H. Leschhorn, “Interface motion in a random medium: mean field theory,” *J. Phys. A* **25** (1992) L555.
86. H. Leschhorn and L.-H. Tang, “Avalanches and correlations in driven interface depinning,” *Phys. Rev. E* **49** no. 2, (Feb, 1994) 1238–1245.
87. O. Narayan and D. S. Fisher, “Critical behavior of sliding charge-density waves in 4-epsilon dimensions,” *Phys. Rev. B* **46** (1992) 11520.
88. O. Narayan and A. A. Middleton, “Avalanches and the renormalization group for pinned charge-density waves,” *Phys. Rev. B* **49** (1994) 244.
89. P. Chauve, T. Giamarchi, and P. Le Doussal, “Creep and depinning in disordered media,” *Phys. Rev. B* **62** no. 10, (Sep, 2000) 6241–6267.
90. P. Chauve, P. L. Doussal, and K. J. Wiese, “Renormalization of pinned elastic systems: how does it work beyond one loop,” *Phys. Rev. Lett.* **86** (2001) 1785–1788.
91. P. L. Doussal, K. Wiese, and P. Chauve *Phys. Rev. B* **66** (2002) 174201.
92. G. Durin and S. Zapperi, “The Barkhausen effect,” in *The Science of Hysteresis, Vol.*

- II*, pp. 181–267. Academic Press, 2006.
93. M. A. Rubio, C. A. Edwards, A. Dougherty, and J. P. Gollub, “Self-affine fractal interfaces from immiscible displacement in porous media,” *Phys. Rev. Lett.* **63** (Oct, 1989) 1685–1688. <http://link.aps.org/doi/10.1103/PhysRevLett.63.1685>.
 94. V. K. Horvath, F. Family, and T. Vicsek, “Dynamic scaling of the interface in two-phase viscous flows in porous media,” *Journal of Physics A: Mathematical and General* **24** no. 1, (1991) L25. <http://stacks.iop.org/0305-4470/24/i=1/a=006>.
 95. S. He, G. L. Kahanda, and P.-z. Wong, “Roughness of wetting fluid invasion fronts in porous media,” *Phys. Rev. Lett.* **69** no. 26, (1992) 3731–3734.
 96. F. Family, K. C. B. Chan, and J. G. Amar, “Dynamics of interface roughening in imbibition,” in *Surface Disorder: Growth, Roughening and Phase Transitions*, P. M. R. Jullien, J. Kertsz and D. E. Wolf, eds., pp. 205–212. Nova Science, New York, 1992.
 97. T. Vicsek, M. Cserzo, and V. K. Horvath, “Self-affine growth of bacterial colonies,” *Physica A: Statistical Mechanics and its Applications* **167** no. 2, (1990) 315–321.
 98. J. Zhang, Y.-C. Zhang, P. Alstrom, and M. T. Levinsen, “Modeling forest fire by a paper-burning experiment, a realization of the interface growth mechanism,” *Physica A: Statistical Mechanics and its Applications* **189** no. 3, (1992) 383–389.
 99. J. P. Sethna, “Statistical mechanics - Crackling crossover,” *Nature Physics (News and Views)* **3** (2007) 518–519.
 100. M. Jost and K. Usadel, “On the automaton representation of the edwardswilkinson model with quenched disorder,” *Physica A: Statistical Mechanics and its Applications* **255** no. 12, (1998) 15 – 25. <http://www.sciencedirect.com/science/article/pii/S0378437198001125>.
 101. A. Rosso, P. Le Doussal, and K. J. Wiese, “Numerical calculation of the functional renormalization group fixed-point functions at the depinning transition,” *Phys. Rev. B* **75** (Jun, 2007) 220201. <http://link.aps.org/doi/10.1103/PhysRevB.75.220201>.
 102. H. Leschhorn and L.-H. Tang, “Comment on “elastic string in a random potential”,” *Phys. Rev. Lett.* **70** (May, 1993) 2973–2973. <http://link.aps.org/doi/10.1103/PhysRevLett.70.2973>.
 103. T. Hwa and D. Fisher, “Anomalous fluctuations of directed polymers in random media,” *Physical Review B* **49** no. 5, (1994) 3136.
 104. W. Press, S. A. Teukolsky, W. T. Vetterling, and B. P. Flannery, *Numerical Recipes in C++*. Cambridge University Press, Cambridge, 2nd ed., 2002.
 105. A. A. Middleton and D. S. Fisher, “Critical behavior of charge-density waves below threshold: Numerical and scaling analysis,” *Phys. Rev. B* **47** (Feb, 1993) 3530–3552. <http://link.aps.org/doi/10.1103/PhysRevB.47.3530>.
 106. L. Laurson, X. Illa, and M. J. Alava, “The effect of thresholding on temporal

- avalanche statistics,” *J. Stat. Mech.* (2009) P01019.
107. D. S. Fisher, “Sliding charge-density waves as a dynamic critical phenomenon,” *Phys. Rev. B* **31** (1985) 1396–1427.
 108. G. Durin, “Private communication.”
 109. M. K. Transtrum, B. B. Machta, and J. P. Sethna, “Geometry of nonlinear least squares with applications to sloppy models and optimization,” *Phys. Rev. E* **83** (2011) 036701.
 110. R. Gutenkunst, *Sloppiness, Modeling, and Evolution in Biochemical Networks*. PhD thesis, Cornell University, 2007.
<http://ecommons.library.cornell.edu/handle/1813/8206>.
 111. L. M. Bettencourt, J. Lobo, D. Helbing, C. Kühnert, and G. B. West, “Growth, innovation, scaling, and the pace of life in cities,” *Proceedings of the National Academy of Sciences* **104** no. 17, (2007) 7301–7306.